Self-Navigated Prospective Motion Correction of repeated 3D-EPI acquisitions for functional MRI applications

Samuel Getaneh Bayih

Department of Human Biology

University of Cape Town

Thesis presented for the degree of

Doctor of Philosophy

January 2024

"I affirm that this thesis has been written solely by me and has not been previously submitted, either in whole or in part, for any academic degree. Unless specifically stated otherwise with reference or acknowledgement, all of the presented work is entirely my own."

Samuel Getaneh Bayih

Declaration on the Inclusion of Publications in a PhD Thesis

I confirm that I have been granted permission by the University of Cape Town's Doctoral Degrees Board to include the following publication(s) in my PhD thesis, and where co-authorships are involved, my co-authors have agreed that I may include the publication(s):

Bayih S.G., Jankiewicz M, Alhamud A, van der Kouwe AJW, Meintjes EM. "Self-navigated prospective motion correction for 3D-EPI acquisition." Magn. Reason. Med.2022;88(1):211-223. doi: 10.1002/mrm.29202.

Signed by candidate

Signature: _____ Date: 01/15/2024

Student Name: Samuel Getaneh Bayih Student Number: BYHSAM001

Abstract

Functional magnetic resonance imaging (fMRI) typically employs one of the fastest pulse sequences – known as echo-planar imaging (EPI) – to repeatedly image the whole brain as stacks of two-dimensional slices. Two-dimensional EPI (2D-EPI) is preferred over three-dimensional (3D)-EPI as it is more motion robust. However, 3D-EPI offers various advantages over 2D-EPI for functional MRI (fMRI), including the absence of spin-history artifacts, potential for faster acceleration, and better signal quality at higher spatial resolution. As such, 3D-EPI would be beneficial for fMRI if it could be made more motion robust.

Various prospective and retrospective motion correction techniques have been developed to minimize subject motion or its effects during MR imaging. The predominant retrospective motion correction techniques, which aim to re-align imaging volumes after acquisition, are incorporated as pre-processing steps in functional MRI analysis packages. However, these typically do not perform intra-volume motion correction. There are also advanced methods that aim to generate artifact-free volumes by using inverse modelling and motion estimates. An alternative approach, termed prospective motion correction (PMC), aims instead to track and correct motion in real time during scanning. PMC techniques typically require either additional external hardware or additional gradient and radio-frequency (RF) pulses inserted into the scanning sequence to track subject motion, thereby increasing scan costs or time. This work demonstrates the application of a novel self-navigated PMC ($snPMC$) approach in repeated 3D-EPI acquisitions to track subject motion and readjust the imaging FOV in real time while a volume is still being acquired without the need for any external hardware or additional gradient and RF pulses.

The technique utilizes the fact that a subset of the partitions acquired to construct an entire 3D volume can be used to re-construct a low-resolution volume image, termed a volumetric self-navigator ($vSNav$), that will contain the same general features as the entire volume and can be used to detect motion while remaining partitions are still being acquired. In our first implementation, we tracked subject motion once per volume by registering each volumetric self-navigator ($vSNav$), constructed from 24 of 52 partitions, to a reference ($vSNav_{Ref}$) acquired and constructed during the first volume acquisition. The estimated motion parameters are sent to the sequence and the sequence updates its imaging field of view (FOV) once per volume. The $snPMC$ 3D-EPI sequence was validated without and with intentional motion in phantoms and in vivo on a 3T Skyra (Siemens, Erlangen, Germany) MRI. For the in vivo scans, motion estimates from the $vSNav$'s were compared to retrospective motion estimates obtained

using FLIRT (FMRIB's Linear Image Registration Tool). Both phantom and in vivo data demonstrated accurate and stable motion estimates in the absence of motion. For phantom acquisitions with intentional motion, estimated residual motion after motion correction were within acceptable thresholds (i.e., < 10% of the slice thickness and < 0.2º rotation). For in vivo acquisitions, motion estimates using $vSNav$ and FLIRT agreed to within 0.23 mm (< 10% of the slice thickness) and 0.14º in all directions.

The performance of our $vSNav$ 3D-EPI sequence for fMRI data acquisition was compared to the widely used 2D-EPI sequence with prospective acquisition correction (PACE). Four healthy volunteers were scanned with both the 3D- and 2D-EPI sequences while performing a block design finger tapping task. Except for flip angles, which were 16º for 3D-EPI and 90º for 2D-EPI, respectively, imaging parameters (i.e., spatial resolution 3.3x3.3x3.1 mm^3) of the two sequences were almost identical. Intentional and unintentional head motions were induced during the experiments while real-time motion detection and correction – $snPMC$ for 3D-EPI and standard PACE for 2D-EPI – were active. After applying identical pre-processing steps and statistical analysis pipelines on the 3D-EPI and 2D-EPI data, it was found that the 3D-EPI data had a greater number of voxels with higher inherent temporal SNR than the 2D-EPI data. While the temporal SNR of the BOLD signal is expected to be higher with 3D-EPI than 2D-EPI at high spatial resolutions, this result was unexpected at this spatial resolution. However, the application of 3.3 mm, 6.6 mm, 8 mm, 9.9 mm and 12 mm FWHM Gaussian spatial filters enhanced the 2D data more than the 3D data, resulting in similar findings following statistical analyses, except that fewer spurious activations were evident in the 3D-EPI data. To fully exploit the superior quality of the 3D-EPI BOLD signal, it will be critical to develop an optimized pre-processing pipeline for 3D-EPI data.

Finally, we aimed to increase the temporal resolution of $snPMC$ by acquiring and registering two (double) volumetric self-navigators ($dvsNav1$ and $dvsNav2$) constructed from two different subsets of the partitions during each volume acquisition. Each $dvsNav$ is registered to its respective reference acquired during the first volume acquisition ($dvsNav1_{Ref}$ or $dvsNav2_{Ref}$). After the motion parameters estimated by either $dvsNav1$ or $dvsNav2$ are sent back to the 3D-EPI sequence, the sequence immediately adjusts its imaging FOV and acquires the subsequent partitions (including those used to construct the next self-navigator) using the updated FOV. The performance of our double volumetric self-navigated ($dvsNav$) 3D-EPI sequence was validated both in a phantom and in vivo, and the in vivo motion estimates were compared to retrospective estimates from FLIRT. The phantom data demonstrated

successful motion estimation and correction; induced motions were accurately detected and completely corrected before accumulation of the partitions for the next $dvsNav$. However, the in vivo data demonstrated above threshold (i.e., > 10% of slice thickness or > 0.2º) differences between motion estimates from the $dvsNav$ sequence and FLIRT. It appears that effects of continuously pulsating motions, which are likely due to physiological noise, limit the accuracy of motion estimation. The detection of continuously pulsating motions was unexpected. These data could potentially be included in motion models to better account for physiological processes.

In conclusion, our results demonstrate that self-navigated 3D-EPI is feasible for functional MRI applications. Further work is needed to accelerate the temporal resolution of motion tracking, to increase both the temporal and spatial resolution of our self-navigated 3D-EPI sequence, and to optimize pre-processing pipelines for 3D-EPI data.

Contents

List of Figures

List of Tables

Preface

This thesis presents a new prospective motion correction (PMC) technique that tracks subject motion in real time without additional hardware or gradient and RF pulses. The thesis evaluates motion correction performance of the proposed method in both phantom and in vivo experiments, as well as its performance for functional magnetic resonance imaging (fMRI) data acquisition.

The thesis contains three independent articles that are presented in chapters two, three and four, respectively. Each chapter assesses different aspects and/or developmental stages of the proposed method, as well as results from validation studies. To date, only the first of these chapters has been published. The introduction provides the necessary background and context for the work. Given that the thesis is a compilation of three independent papers, there is necessarily some repetition. For the purposes of thesis examination, the contributions of the co-authors are provided below.

Chapter One discusses the principles of nuclear Magnetic Resonance Imaging (MRI), fMRI and echo-planar imaging (EPI) sequences. It details various artifacts that confound fMRI data, especially those that arise from subject movement during scanning, and widely used techniques to address motion artifacts.

In Chapter Two, a novel self-navigated method for prospective motion correction (PMC) during repetitive 3D-EPI acquisition is introduced. The technique involves constructing a volumetric self-navigator ($vSNav$) to detect subject motion and sending motion parameters to the sequence to update the imaging field-of-view (FOV) once per volume. The chapter has been published as an article titled "Self-navigated prospective motion correction for 3D-EPI acquisition", which appeared in the esteemed journal Magnetic Resonance in Medicine in July 2022, Volume 88, Issue 1, Pages 211-223.

I authored the article with the help of four co-authors. Ernesta Meintjes provided technical expertise in acquiring and analysing the data, understood the potential of the 3D-EPI sequence in fMRI, and supervised the overall project. Andre van der Kouwe and Ali Alhamud introduced me to the Siemens IDEA framework. I designed the centre-out acquisition algorithm, which was critical for self-navigator development, and implemented the $vSNav$. I acquired the data, developed the algorithms, and methods for validation, and performed the data processing. Ernesta Meintjes and Andre van der Kouwe provided technical support and expertise. I drafted

the article and received editorial and scientific input from my co-authors, Ernesta Meintjes, Andre van der Kouwe, Marcin Jankiewicz, and Ali Alhamud.

Chapter Three compares the performance of the $vSNav$ 3D-EPI sequence to the widely used 2D-EPI sequence with PACE (Prospective Acquisition Correction; Thesen et al., 2000) for fMRI data acquisition. Temporal signal-to-noise ratios (SNR) and brain activations seen with 2D- and 3D-EPI are compared on a finger tapping experiment both in the absence and presence of intentional head motions. I designed the experiments, and acquired and analysed the data. My supervisors provided technical support and editorial feedback on the manuscript.

Chapter Four of this dissertation covers the implementation and validation of the double volumetric self-navigated ($dvsNav$) 3D-EPI sequence, which doubles the temporal resolution of self-navigated PMC (snPMC). The chapter provides the theoretical background and a detailed discussion of the design and implementation of the dvsNav 3D-EPI sequence. After comparing six different potential configurations for the double volumetric self-navigators ($dvsNavs$), the most suitable configuration is implemented. The chapter presents the results from phantom and in vivo experiments, both in the absence and presence of intentional motion. I designed and implemented the $dvsNav$ 3D-EPI; validation experiments were designed with the help of my supervisors, Ernesta Meintjes and Andre van der Kouwe. I acquired and analyzed the data and drafted the chapter. My supervisors provided scientific and editorial input.

Chapter Five provides a comprehensive summary and discussion of the main findings of the thesis, discusses the limitations and strengths of the methods and results presented, and suggests possible future work.

Acknowledgements

Ernesta Meintjes was the supervisor for this project. She, along with Andre van der Kouwe, provided the necessary context, expert ideas, advice, support, and resources required for the implementation of this work. I would like to express my gratitude for their significant contributions, without which this project would not have been possible. I would also like to extend my thanks to Ali Alhamud and Marcin Jankiewicz for their valuable inputs.

I am immensely grateful to my sister, Engidawork Ayele, and brother-in-law, Mebrat Ayele, for their unwavering support since forever.

I would like to thank Rene Lenssen, who managed my NUFFIC scholarship, for his understanding especially during the COVID lockdown.

The resources used in this work were provided by the University of Cape Town, Cape Universities Body Imaging Centre (CUBIC), and Athinoula A. Martinos Center for Biomedical Imaging.

This study received support from the South African National Research Foundation grant 48337 and National Institute of Health (NIH) grants: R01HD085813, R01HD099846, and R01HD093578.

Chapter One

1. Introduction

This thesis introduces and validates a novel technique to track and correct head motion in real time in applications that require repeated magnetic resonance imaging (MRI) acquisitions (such as functional MRI) without additional hardware or dedicated pulse sequences. This chapter discusses the background and motivation for this work, basic principles of functional MRI (fMRI), fMRI acquisition pulse sequences including echo-planar imaging (EPI), motion during acquisition and subsequent artifacts, and current techniques to eliminate or minimize motion artifacts in fMRI. Chapter 2, which is a published paper (Bayih et al., 2022), discusses the implementation in repeated three-dimensional EPI (3D-EPI) acquisitions of a volumetric self-navigator ($vSNav$) for prospective motion correction, and chapter 3 compares the performance of the proposed approach to standard 2D-EPI for a finger tapping fMRI experiment. In chapter 4, the double volumetric self-navigator ($dvsNav$) is introduced to increase the temporal resolution of motion correction. Chapter 5 is a comprehensive discussion based on the main findings of chapters 2, 3 and 4. The final chapter presents the conclusions.

1.1. Background and motivation

Functional magnetic resonance imaging (fMRI) is a non-invasive brain imaging technique used to link different regions of the brain with corresponding functions based on task-correlated changes in local cerebral blood oxygenation levels. Moreover, fMRI links different regions of a brain based on synchronously correlated blood oxygenation level changes in the regions – showing intrinsic brain networks within the brain. However, the variations in MR signal due to the coupling of action or inaction in the brain with changes in local cerebral blood oxygenation are comparable in magnitude to variations arising from other signal sources, also known as noise. Even though technological advancements have minimized and eliminated some of the sources of noise and their effects on the MR signal, subject motion during scanning remains the most prevalent source of confounding artifacts in fMRI. Different motion correction techniques – broadly grouped as retrospective and prospective – have been developed to address problems of motion artifacts in MRI. In fMRI, head motion artifacts can be minimized or avoided prospectively (i.e., motion detection and correction in real time), and any remaining artifacts are removed from the data retrospectively, depending on the severity of motion. Prospective motion correction techniques, which attempt to avoid or minimize the

confounding effects of subject motion by adjusting the acquisition field of view in real time when motion occurs, have been indispensable tools in enhancing the statistical power of fMRI data. However, prospective motion correction techniques either require dedicated pulses or external hardware which commonly needs its own configuration and calibration.

The aim of this project was to develop an alternative approach to prospective motion correction that detects and corrects motion in real time without additional external hardware or radio frequency (RF) and gradient pulses, thus eliminating the additional "dead-time" introduced by navigators. The development was done on the Siemens 3 T Skyra scanners (Erlangen, Germany) at the Cape Universities Body Imaging Center (CUBIC) located at the Faculty of Health Sciences (FHS) of the University of Cape Town (UCT) (Cape Town, South Africa) and at the Martinos Center for Biomedical Imaging (Charlestown, MA, USA). Protocols had been approved by the Human Research Ethics Committee of the UCT FHS.

1.2. Functional Magnetic resonance imaging (fMRI)

1.2.1. Principles of nuclear magnetic resonance

The hydrogen nucleus, which is the element typically imaged during magnetic resonance imaging, comprises a single proton. A proton is a positively charged subatomic particle that has an intrinsic property called spin, giving rise to a magnetic dipole moment (μ). The adult brain is comprised of approximately 6.9×10^{25} hydrogen nuclei (i.e. dipole moments) (Mitchell et al., 1945) that are usually randomly oriented, resulting in no net magnetization.

When placed in a static magnetic field, $\mathbf{B_0}$, the dipole moment associated with each proton experiences a torque ($\boldsymbol{\tau} = \boldsymbol{\mu} \times \mathbf{B_0}$) that causes it to precess around the magnetic field. The dipole moments precess at a characteristic frequency called the Larmor precession frequency, f_L, which is given by

$$f_L = \gamma B_0, \tag{1.1}$$

where γ is the gyromagnetic ratio specific to the nucleus. Since the gyromagnetic ratio (γ) of ^{1}H is 42.58 MHz/T, the dipole moments associated with hydrogen nuclei will precess at a frequency of 127.74 MHz around a 3 T field. Given that the millions of hydrogen dipole moments were randomly oriented prior to commencing their precessional motion, their randomly oriented transverse components will cancel while they are precessing, resulting in a net magnetization ($\mathbf{M_0}$) parallel to the static magnetic field.

Application of a small alternating magnetic field, $\mathbf{B_1(t)}$, at the Larmor frequency and perpendicular to the static $\mathbf{B_0}$ field, causes the magnetization to precess around $\mathbf{B_1}$ at a

frequency $f_1 = \gamma B_1$. This alternating transverse field is referred to as the radiofrequency (RF) pulse, and the requirement that the frequency be matched to the Larmor precession frequency is called the resonance condition; excitation (i.e. rotation of the magnetization away from being aligned parallel to $\mathbf{B}_0$) only occurs if the resonance condition is met. The duration of the RF pulse determines the angle through which the magnetization will rotate around the $\mathbf{B}_1$ axis. This angle (α), known as the flip angle, is given by $\alpha = 360° \cdot \gamma B_1 t$, where t is the time for which the RF pulse is applied. Following excitation, the magnetization therefore has components parallel (by convention termed M_z) and perpendicular (M_{xy}) to the static magnetic field. These are referred to as the longitudinal and transverse components, respectively. When the RF pulse is terminated, the millions of dipole moments that constitute the net magnetization again start precessing around the axis of the static magnetic field, $\mathbf{B_0}$, at the Larmor frequency, resulting in a net magnetization, **M(t)**, precessing around $\mathbf{B}_0$. While precessing, the magnetization returns to its equilibrium position aligned parallel to $\mathbf{B_0}$ through a process known as relaxation.

Relaxation comprises two independent and distinct mechanisms: (i) longitudinal or spin-lattice relaxation which is caused by the spins' loss of energy to the surrounding environment, and (ii) transverse or spin-spin relaxation that occurs due to individual spins becoming out of phase. The longitudinal relaxation process, known as T_1 recovery, is characterized by a time constant T_1 given by

$$M_z(t) = M_0(1 - e^{\frac{-t}{T_1}}), \tag{1.2}$$

where $M_z(t)$ is the longitudinal magnetization at any time t, and M_0 is the net magnetization before excitation. T_1 is therefore the time when the longitudinal magnetization has regrown to 63% of its maximum value.

Transverse or spin-spin dephasing occurs due to each spin being in a slightly different local environment and experiencing a slightly different net magnetic field. This results in each spin precessing at a slightly different frequency around $\mathbf{B_0}$, which causes spins to lose their phase coherence with time and loss of the transverse magnetization, M_{xy}. The rate at which the transverse signal decays from its maximum value immediately after excitation, $M_{xy}(0)$, is characterized by a time constant T_2, given by

$$M_{xy}(t) = M_{xy}(0)(e^{\frac{-t}{T_2}}). \tag{1.3}$$

T_2 is therefore defined as the time when the signal has decayed by 63%. In addition to true spin-spin dephasing, any local magnetic field inhomogeneities also contribute to signal loss. The combined effect of spin-spin interactions and magnetic field inhomogeneities is called T_2^*

decay and is characterized by the time constant T_2^*. Therefore, the net transverse magnetization at any time t after excitation, $M_{xy}(t)$, is computed with equation (1.3) but replacing T_2 by T_2^*.

The Bloch equation (Bloch, 1946) describes the motion of the magnetization vector **M(t)** in the presence of a time-varying magnetic field **B(t)**, and both longitudinal and transverse relaxation, namely

$$\frac{d\mathbf{M}(t)}{dt} = \left(\gamma \mathbf{M}(t) \times \mathbf{B}(t)\right) + \frac{1}{T_1}(M_0 - M_z)\hat{\boldsymbol{k}} - \frac{1}{T_2}\left(M_x\hat{\boldsymbol{\imath}} + M_y\hat{\boldsymbol{\jmath}}\right). \quad (1.4)$$

The equation states that the net magnetization vector precesses around the net magnetic field, with its magnitude in the longitudinal and transverse directions governed by the time constants T_1 and T_2, respectively. Only the net transverse magnetization contributes to the measured MRI signal.

1.2.2. Principles of magnetic resonance image formation

A magnetic resonance (MR) image is a map that shows the spatial distribution of atomic nuclear properties such as nuclear density, T_1, T_2 or nuclear motion, within an object. An MR image is constructed from MR signals that are spatially encoded with spatially varying magnetic fields (Lauterbur, 1973). Superimposing predetermined spatially varying magnetic fields (i.e., spatial gradient fields) on the static magnetic field causes atomic nuclei at different locations to precess at different rates $f(l)$, as computed with the following equation,

$$f(l) = \gamma B(l), \quad (1.5)$$

where l is the spatial coordinate along the spatial gradient field, $B(l)$ is the total magnetic field at a spatial coordinate l along the spatial gradient field, and γ is the gyromagnetic ratio.

Spatial information in MRI is resolved by using spatial gradient fields. The direction of the static magnetic field ($\mathbf{B_0}$) is parallel to the scanner bore and is called the longitudinal (or z) direction; x and y refer to the two transverse directions. Applying a magnetic field gradient along the x, y or z direction will spatially vary the strength of the magnetic field in the direction of the applied gradient. By applying x, y or z gradients simultaneously, the magnetic field can be varied along any direction, and correspondingly the frequency of the MR signal along that direction. In practice, 3 mutually orthogonal field gradients are applied at different times during image acquisition to encode spatial information into the frequency and phase of the MR signal, which can be extracted using mathematical constructs like Fourier transforms. These temporal patterns of gradient field and RF pulse variations are coded in MR pulse sequences.

Conventional two-dimensional (2D) pulse sequences first select a slice of the object to be imaged (i.e., slice selection), and then resolve the in-plane spatial dimensions within the slice (i.e., frequency and phase encodings). The purpose of slice selection is to localize the MR slice. This is achieved by applying a gradient perpendicular to the slice direction (i.e., slice-select gradient (G_{ss})) at the same time as the RF pulse. By setting the frequency of the RF pulse to match the Larmor precession frequency of spins in the slice (or slab) of interest, only those spins are excited. The thickness of the slice/slab will depend both on the RF bandwidth and the strength of the G_{ss}. Following slice selection, frequency encoding and phase encoding steps are used to extract the spatial distribution of spins within the slice. One-dimensional spatial information can be obtained using a single frequency-encoding (or readout) gradient (i.e., G_{FE}) applied during signal readout. This causes nuclei in different positions along the frequency encoding direction to precess with different frequencies. However, when two-dimensional spatial information is required, an additional gradient, called the phase-encoding gradient (i.e., G_{PE}), is required. The phase-encoding gradient, which is applied between excitation and readout, causes spins along its direction to become out of phase, with the amount of phase incoherence determined by the strength of the phase encoding gradient. A 2D inverse Fourier transform is applied to the spatially encoded MR signals to resolve the spatial information and reconstruct the MR image. Depending on the type and purpose of the MRI acquisition, the timing and duration of RF and gradient pulses can vary. Excitation, encoding and signal readout schemes are depicted in diagrams called pulse sequence diagrams.

1.2.3. Blood-oxygenation-level dependent (BOLD) signals

Neural activity associated with sensory, motor, or cognitive processes increases local cerebral blood flow (CBF). Since the localized changes in CBF are greater than activity-induced changes in the cerebral metabolic rate for oxygen (Mintun et al., 2001), the relative concentration of oxy- to deoxyhemoglobin increases in active brain regions. Oxyhemoglobin is diamagnetic and has little effect on magnetic field lines, whereas deoxyhemoglobin is paramagnetic and concentrates magnetic field lines (Pauling & Coryell, 1936), thereby accelerating T_2* decay. A relative increase in oxyhemoglobin therefore reduces T_2^* decay, resulting in a localized increase in the MRI signal on T_2^*-weighted images. The change in signal that results from changes in blood oxygenation is called the blood-oxygenation-level dependent (BOLD) contrast (Ogawa et al., 1990).

Although the exact physiology of the BOLD response following a brief stimulus is complex and controversial, the main stages are described by the Hemodynamic Response

Function (HRF) (see Figure 1-1). Immediately after the stimulus, the localized cerebral metabolic rate of oxygen (CMRO2) increases, resulting in a decrease in the local oxyhemoglobin concentration and a corresponding increase in the ratio of deoxy- to oxyhemoglobin. This relative increase in the local deoxyhemoglobin concentration results in signal loss, referred to as the initial dip. Approximately 1 to 2 seconds after the stimulus, the brain reacts by increasing cerebral blood flow (CBF) to the affected regions, flooding the activated regions with oxygenated hemoglobin at a rate higher than the CMRO2 and increasing the cerebral blood volume (CBV) (Fox & Raichle, 1986). The local concentration of oxygenated hemoglobin continues to increase until it reaches a peak around 4 to 6 seconds after the stimulus, with a corresponding increase in the BOLD signal. After reaching a peak, CMRO2 and CBF decreases to their normal levels faster than CBV. The lag in the CBV decrease results in a brief period when the relative concentration of deoxy- to oxyhemoglobin is higher than its pre-stimulus level, causing the BOLD signal to dip below baseline. This is referred to as the post stimulus undershoot. The BOLD signal intensity returns to its original level once the CBV, CMRO2 and CBF have all returned to their original (pre-stimulus) levels.

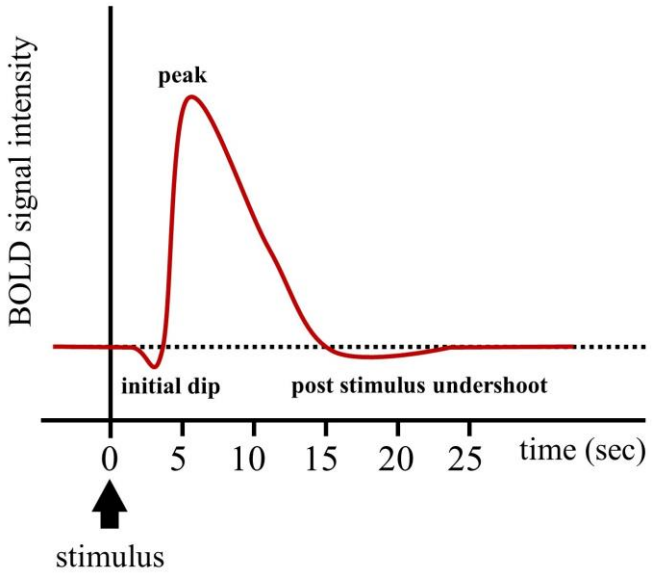

Figure 1-1 BOLD Hemodynamic Response Function (HRF) following a brief stimulus.

The HRF shown in Figure 1-1 depicts the BOLD response following a single brief stimulus. For multiple stimuli that are separated by at least 5 seconds, the HRF can be approximated by superposition of the HRFs of all the stimuli (Boynton et al., 1996; Dale & Buckner, 1997). However, presentation of multiple stimuli separated by 1 second was observed to evoke a reduced BOLD response (Huettel & McCarthy, 2000). The time period after

presentation of a stimulus where presentation of another stimulus results in a reduced BOLD response is known as the refractory period. The refractory period depends on the region of the brain, the duration of the stimuli and the type of stimuli (Birn et al., 2001; Huettel et al., 2004).

1.2.4. BOLD fMRI

Functional magnetic resonance imaging (fMRI) is a non-invasive neuroimaging technique that uses the BOLD effect to measure and localize brain activity while performing a task. During fMRI, the temporal evolution of the BOLD signal is measured through repeated acquisition of T_2^* weighted brain images. Each of the repeatedly acquired three-dimensional T_2^* weighted brain volumes are tagged with their acquisition time, yielding a four-dimensional dataset. The temporal signal variations of individual voxels in the T_2^* weighted brain volumes are then analyzed to identify voxels in which the signal variations are temporally correlated with the stimulus pattern or, in the case of resting state fMRI, with each other. Depending on the voxel size and magnetic field strength, the BOLD signal change can be 1% or less of the MR signal intensity (Bandettini et al., 1993), making it highly susceptible to various noise artifacts. Therefore, the power to detect BOLD signal changes depends to a large extent on the quality of the signal.

Once the dataset is acquired, it is preprocessed to obtain viable BOLD signals for statistical analysis. Pre-processing typically includes slice scan-time correction, which adjusts the time stamp of each slice based on the timing of its acquisition within the volume, co-registering each volume to the reference volume, temporal filtering to remove physiological artifacts and signal drifts (Birn et al., 2008; Shmueli et al., 2007), spatial smoothing to suppress noise signals uncorrelated to the region of interest, correcting distortions due to local magnetic field inhomogeneity using field maps (Jezzard & Balaban, 1995; Jezzard & Clare, 1999), and making each time point of the dataset independent of its predecessor, also known as pre-whitening (Huettel et al., 2014). Depending on the fMRI experiment type, design, acquisition protocol, and data quality, the preprocessing pipeline may skip some steps or include additional ones. Notably, co-registration to the reference volume aims to correct for inter-volume motion to ensure that the same voxel in successive volumes contains signal from the same anatomical region.

After preprocessing, statistical analyses are performed. For task-based fMRI, first-level statistical analysis typically involves solving a general linear model (GLM) in each voxel to determine the parameter estimates of each predictor. These parameter estimates describe the degree to which signal variation in the voxel may be attributed to the relevant predictor, i.e. to

the task being performed. For group analyses, first-level analyses are followed by second-level statistical analysis. Second-level analyses involve comparing parameter estimates for the different predictors between groups of subjects, or examining associations of parameter estimates with clinical or cognitive outcomes. For rs-fMRI, correlation analysis, independent component analysis (ICA) or Multi-Variate Pattern Analysis (MVPA) may be performed to identify voxels with correlated BOLD signal timecourses.

Correlation analysis computes the correlation coefficient (r) between two series X = $x_1+x_2+x_3+\ldots+x_N$ and Y = $y_1+y_2+y_3+\ldots+y_N$ using equation (*1.6*)

$$r = \frac{\sum_{i=1}^{N}(x_i-\bar{X})(y_i-\bar{Y})}{\sqrt{\sum_{i=1}^{N}(x_i-\bar{X})^2 \sum_{i=1}^{N}(y_i-\bar{Y})^2}}, \tag{1.6}$$

where $\bar{X}$ and $\bar{Y}$ are the mean values of series X and Y, respectively, r ∈ [-1, 1]. Readers are encouraged to refer to (Bandettini et al., 1993) for details on correlation and its application in fMRI.

Independent component analysis (ICA) extracts common features from fMRI signals without inputs of hypothesized waveforms. ICA allows detection of undetected linearly-mixed-independent signals. Readers are encouraged to refer to (Bell & Sejnowski, 1995; Mckeown et al., 1998; McKeown et al., 2003) for details on ICA and its application in fMRI.

Multi-variate pattern analysis (MVPA) captures spatial patterns of functional activity in relation to different experimental conditions using machine learning pattern recognition algorithms. Readers are encouraged to refer to (Davatzikos et al., 2005; Mahmoudi et al., 2012) for details of MVPA and its application in fMRI.

In this work, we used a General Linear Model (GLM) to identify voxels in which the signal timecourse was significantly correlated with the stimuli. GLM models the MRI signal of a given voxel over N time points ($y_1, y_{2,}, y_3, \ldots, y_N$) (i.e. N volumes) as the sum of experimental design variables ($x_{1,1}, \ldots, x_{N,p}$) weighted by scalar parameter estimates ($\beta_1, \beta_2, \beta_3, \ldots, \beta_p$), error terms (ε_1, ε_2, ε_3, ..., ε_N), and a constant term β_0, as shown in equation (1.7). The stimulus model, X, may include predictors of no interest and nuisance variables, such as motion parameters and low-frequency drifts. The GLM equation is given by

$$Y = \beta_0 + X\beta + \varepsilon \tag{1.7}$$

where Y is an $N \times 1$ vector that holds N intensity values of a voxel from N time points, X is an $N \times p$ matrix, referred to as the design matrix, which holds all the model time courses, β is a $p \times 1$ vector, referred to as the parameter estimates (PEs), and ε is an $N \times 1$ vector, also referred to as residuals, that holds the error values. The stimulus model is usually convolved

with a model of the hemodynamic response function (HRF) to more closely match the expected BOLD signal change and improve model fitting.

The parameter estimates (PEs) are compared with the uncertainty of their estimations by using the t-test shown in equation (1.8) where σ is the standard deviation of the PE and N is the total number of time points. If the t-value significantly differs from zero, then the PE values represent more reliable activations.

$$t = \frac{PE}{(\frac{\sigma}{\sqrt{N}})} \qquad (1.8)$$

Other statistical presentations such as P (probability) and Z statistics of how well the data (Y) fit to the models (X) are also calculated from the t values. Readers are encouraged to refer to (Jezzard et al., 2001; Monti, 2011) for further details.

1.2.5. Pulse sequences for fMRI

The temporal resolution of fMRI, which involves repeated whole-brain acquisitions to measure changes in the T2* weighted signal with time, depends on the speed of the imaging sequence. A widely used sequence is the gradient-echo (GE) echo-planar imaging (EPI) sequence, which is both fast and sensitive to local magnetic field variations. The details of the EPI sequence are described below using pulse sequence diagrams. The vertical and horizontal axes of the pulse sequence diagram show the amplitude and timing of the various pulses (i.e., RF and gradients) applied during the acquisition.

Echo-planar imaging (EPI) sequence

EPI, which is one of the fastest MRI pulse sequences (Stehling et al., 1991), can acquire sufficient data to reconstruct a complete (albeit low resolution) image slice following a single RF excitation pulse. Single-shot EPI acquires an entire image slice following a single excitation pulse, while multi-shot EPI applies multiple RF excitation pulses to achieve higher spatial resolution. After excitation, the EPI sequence uses a sequence of bipolar frequency-encoding gradients (G_{FE}) interleaved with small phase-encoding gradient blips (G_{PE}) to generate a train of spatially-encoded echoes for different amounts of phase dispersion. The digitized echoes therefore fill successive rows of k-space in a zig-zag fashion. The time duration between the center of the RF excitation pulse and the mid-point of the data acquisition (or readout) period is called the echo time (TE). The time duration between the centers of successive RF excitation pulses is called the repetition time (TR). The EPI sequence can be used for two-dimensional or three-dimensional acquisitions. These are referred to as 2D-EPI or 3D-EPI sequences, respectively (see Figure 1-2).

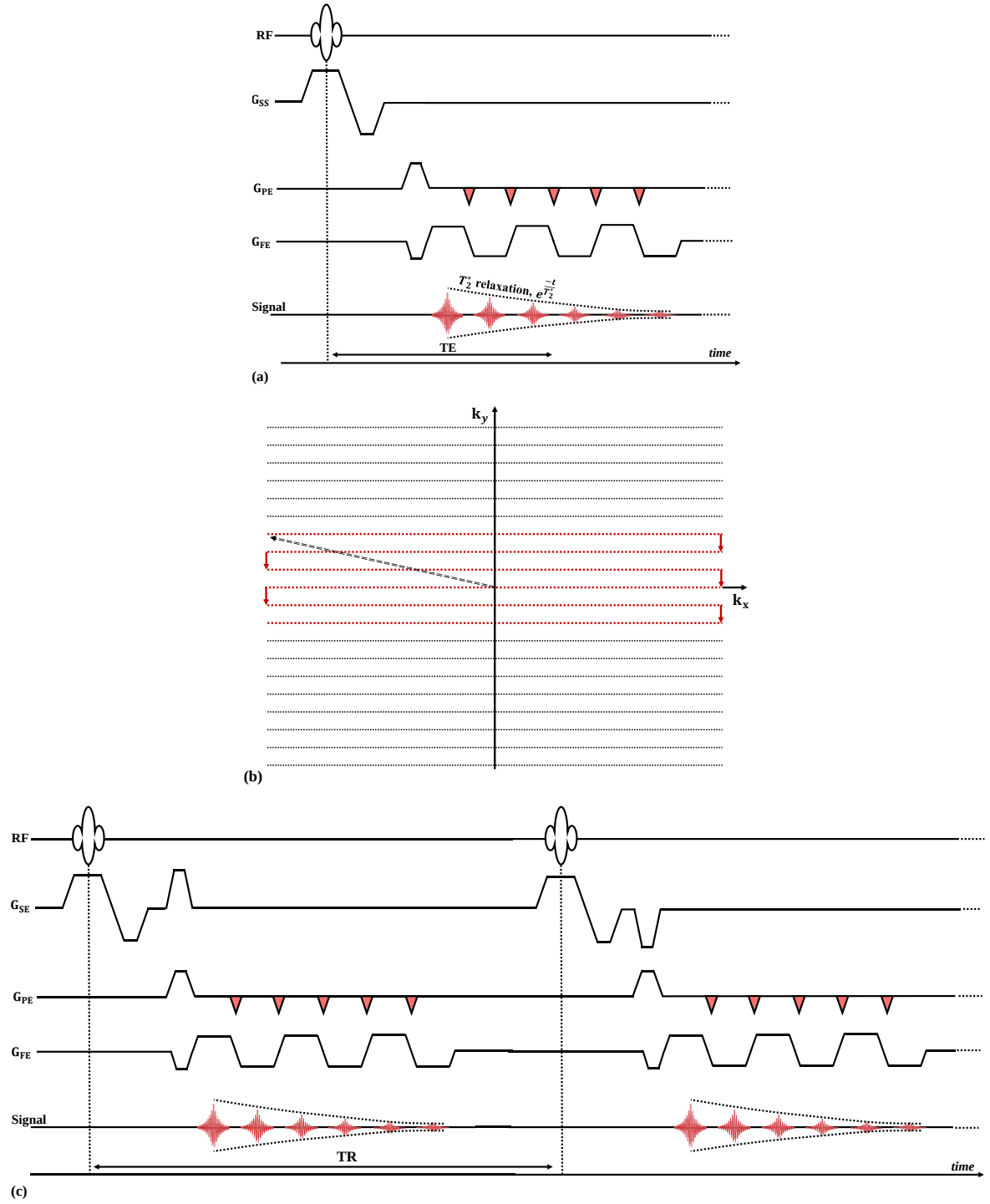

Figure 1-2 EPI pulse sequence diagrams and k-space trajectory. (a) Diagram of the EPI pulse sequence for two-dimensional acquisition (2D-EPI) and (b) its corresponding k-space filling with a cartesian trajectory. (c) Diagram of the EPI sequence for three-dimensional acquisition (3D-EPI).

The 2D-EPI sequence first excites a slice of interest by setting the center frequency of the RF excitation pulse to the Larmor frequency of that slice; the slice frequency depends on the static field strength, B_0, and the slice select gradient, G_{ss}. The slice thickness is determined by the RF bandwidth and the strength of the slice select gradient. Immediately after slice

excitation, G_{SS} generates a pulse with approximately half the duration and opposite polarity to the preceding slice select gradient pulse. This gradient pulse, which is referred to as the rephasing lobe, is applied to compensate for phase dispersions that occur during the finite duration of the RF excitation pulse. Before commencing signal recording (analog to digital conversion), preparatory lobes of G_{PE} and G_{FE} are applied to set to the first sample point of the first k-space line (see Figure 1-2 (a) and (b)). MR signal recording (k-space filling) is characterized by oscillating bipolar G_{FE} pulses that generate a train of echoes. The oscillating G_{FE} pulses oscillate the recording direction of the k-space lines (k_x) between positive and negative directions, while the application of G_{PE} 'blips' between echoes shifts the k-space line that the echo corresponds to (see Figure 1-2 (b)). In 2D-EPI, the next slice is selected during the next RF excitation pulse with a new center frequency and with the same G_{SS}, whereafter the phase-encoding and readout processes are repeated.

In contrast to 2D-EPI, the 3D-EPI sequence simultaneously excites an entire set of contiguous slices, also known as a slab. The "slices", also called partitions to distinguish them from slices in 2D imaging, are then encoded using an additional phase encoding gradient applied in a direction perpendicular to the "partitions. This is called the slice-encoding (G_{SE}) gradient. Exactly as in 2D-EPI, the remaining primary phase- and frequency-encoding (i.e., G_{PE}, and G_{FE}) gradients encode the in-plane spatial locations of the selected partition (Figure 1-2 (c)), filling 2D k-space in a zig-zag fashion. To acquire *n* partitions in a slab, this process needs to be repeated for *n* different G_{SE}. Equation (1.9) gives the relationship between gradient pulses and coordinates in k-space.

$$\begin{aligned} k_x(t') &= \int_0^{t'} \gamma G_{RO}(t)\, dt \\ k_y(t') &= \int_0^{t'} \gamma G_{PE}(t)\, dt \\ k_z(t') &= \int_0^{t'} \gamma G_{SE}(t)\, dt \end{aligned} \tag{1.9}$$

Factors like the strength of the static magnetic field, experimental design and fMRI acquisition parameters determine the number, amplitude and period of sequence pulses (see Figure 1-2) and the quality of the fMRI data.

1.2.6. Imaging parameters in fMRI

One of the challenges in 2D and 3D acquisitions using single-shot EPI sequences is global signal dropout across the entire image due to T_2^* relaxation effects. The T_2^* relaxation rate determines the amount of MR signal loss at the center of k-space (i.e., at $k_x = k_y = 0$) or in other words, at TE. Depending on the length of the acquisition window, MR signals sampled at the beginning and end of the readout period will have different amplitudes, which affect the degree of blurring and global signal dropout in the images. The problem of blurring and signal attenuation due to long acquisition duration can be rectified: i) by increasing the receiver bandwidth, which increases the MR signal sampling rate but results in poorer signal quality (usually measured in signal-to-noise ratio (SNR)), or ii) by decreasing image resolution for the same coverage (field of view). Given that image resolution is inversely proportional to the maximum value sampled along that direction in k-space (i.e. $\Delta y = 1/k_y^{max}$), lower resolution corresponds to a smaller k-space matrix, which will shorten the acquisition time. Although increasing voxel size usually increases SNR, very large voxels also increase intravoxel inhomogeneities, which may result in significant partial volume averaging and decreased SNR.

The statistical power of an fMRI analysis depends on how strongly local fluctuations in the T_2^* signal are correlated with the neural activity being measured. However, the resulting signal change (i.e., BOLD contrast) can be 1% (or less) of the average MR signal. To maximize the statistical power of fMRI data, it is necessary to maximize T_2^* fluctuations arising from neural activity. Assuming that noise fluctuations are not correlated to neural activities, the maximum BOLD contrast will be obtained at TE ≈ T_2^* (van der Zwaag et al., 2009).

To further maximize the BOLD contrast of T_2^* images in fMRI acquisitions at a specific static magnetic field strength, the net magnetization available for repeated RF excitation has to be maximized. The net magnetization available for repeated RF excitation depends on the time duration between consecutive RF pulses (TR), the flip angle (α) and longitudinal relaxation time (T_1). TR also determines the number of T_2^* weighted images that can be acquired and the total acquisition time. Therefore, after selecting TR, the optimum flip angle, which maximizes the net magnetization available for RF excitation, also known as the Ernst angle α_{ernst} is determined using equation (1.10) (Ernst & Anderson, 1966; Winkler et al., 1988).

$$\alpha_{ernst} = \cos^{-1}(e^{\frac{-TR}{T_1}}) \qquad (1.10)$$

In equation (1.7), α_{ernst} is the Ernst angle (^{0}), TR is the repetition time (ms), and T_1 is the longitudinal relaxation time of grey matter (ms).

1.2.7. 2D- and 3D-EPI sequences in fMRI

2D-EPI is widely used in fMRI because of its sensitivity to BOLD contrast, its ability to cover the whole brain with spatial (~2–4 mm) and temporal (~2–3 s) resolutions suitable for most fMRI experiments, and robustness to motion artifacts (Chen & Glover, 2015; Norris, 2006). However, creating large signals in 2D-EPI requires large flip angles (~90º), which increases the amount of power deposited in tissues, known as the specific absorption rate (SAR) (Collins & Wang, 2011). Long acquisition times and low SNR limit the use of 2D-EPI for high spatial resolution fMRI acquisitions (Bernstein et al., 2004). Accelerated acquisition techniques such as partial Fourier (PF) sampling (Jesmanowicz et al., 1998) and partial parallel imaging (PPI) (Griswold et al., 2002; Pruessmann et al., 1999) have limited temporal gain in 2D-EPI because of the tradeoffs between TE and optimum BOLD contrast. Moreover, 2D-EPI sequences are inherently susceptible to spin-history artifacts which are very difficult, if not impossible, to remove once they are induced (Karl J. Friston et al., 1996).

Although 3D-EPI alleviates some of the limitations of 2D-EPI, it is less widely used in fMRI mostly because of its high susceptibility to motion artifacts. For instance, 3D-EPI uses smaller flip angles (i.e. <20º) that result in significantly lower SAR, 3D-EPI has better BOLD signal sensitivity in high spatial resolution fMRI than 2D-EPI (Bernstein et al., 2004), accelerated acquisition techniques can be implemented in the secondary phase-encoding (i.e. slice-encoding) direction resulting in significant temporal gain, and there are no spin-history artifacts.

1.2.8. Noise signals in fMRI

Some of the challenges in fMRI stem from low BOLD contrast, which is comparable to or sometimes less than the contrasts created by noise. Noise signals can be grouped broadly into thermal noise, system noise, physiological noise, noise due to unexpected neuronal activities, noise due to variability in task performance and noise due to head motion.

Thermal Noise

Thermal noise is intrinsic to MRI due to the non-zero thermal energy within subjects and scanner electronics. These noise signals are linearly proportional to magnetic field strength and fluctuate randomly with no spatial or temporal correlation. However, the effects of thermal noise on each voxel can be modelled reasonably well. For instance, thermal noise signals have additive contributions in background voxels where there is assumed to be no MR signal. Therefore, effects of thermal noise on the background voxels can be approximated by zero bounded positively skewed distributions such as a Rayleigh distribution. On the other hand, the fluctuations have both additive and subtractive contributions to MR signals with significant

intensities in the region of interest. Hence the effects of thermal noise on brain voxels are approximated by a Gaussian distribution (Edelstein et al., 1986; Kellman & McVeigh, 2005; Krüger & Glover, 2001; Wald & Polimeni, 2017).

Physiological Noise

In fMRI, physiological noise signals are those generated by physiological activities (other than BOLD). These constitute approximately 40% and 52% of the total noise at 1.5 T and 3.0 T, respectively, and increase with the strength of the magnetic field (Krüger et al., 2001). Although physiological noise increases faster than thermal noise with increasing magnetic field strength, its rate of increase slows as spatial resolution increases (Triantafyllou et al., 2005). Physiological noise signals are generated predominantly by cardiac and respiratory activities. Cardiac pulsations create localized noise near edges of the brain or blood vessels; resulting artifacts are most pronounced in areas near large arteries. Usually, fMRI acquisition configurations are too slow to sufficiently sample cardiac noise which may result in aliasing and manifest as subtle functional activations. Further, thoracic movements due to breathing may, in addition to localized artifacts in brainstem areas, disturb the homogeneity of the static magnetic field and induce artifacts across the entire brain (Krüger & Glover, 2001; Liu, 2017; Raj et al., 2001).

Various methods have been developed to minimize the effects of physiological noise in fMRI data retrospectively. Some of the methods monitor cardiac and respiratory activities using devices then sort the image data relative to the phases of the noise cycles (Glover et al., 2000) or estimate and remove physiological noise (X. Hu et al., 1995). Other methods model the physiological noise in regions-of-interest (ROI) where no BOLD response is expected, such as white matter, large vessels and cerebrospinal fluid (CSF), and include the models as nuisance parameters within the general linear model when analyzing the BOLD time series data (Behzadi et al., 2007).

System Noise

System noise is caused by inconsistencies in the MRI hardware or environment. One of the most common sources of system noise in fMRI is a slow shift in the frequency distribution of the MRI signals, also known as scanner drift, due to either inherent slow changes in the strength of the static magnetic field over time or aliasing because of hardware limitations that result in under-sampling of physiological pulsations. Scanner drift is corrected during preprocessing (i.e., detrending) using temporal high-pass filtering (Chen & Glover, 2015; Tanabe et al., 2002). Any instability in the gradient coils will also alter the spatial encoding,

thereby changing the shapes and locations of the recorded MR signals (Bernstein et al., 2004; Hidalgo-Tobon, 2010).

Further, improper configuration or use of RF coils can reduce the excitation efficiency and coil sensitivity which ultimately induce artifacts like shading – MR signal cancellations or reductions. The sensitivity of the RF receiver coil is affected, for example, by its proximity to the signal with closer tissues generating the largest signals, failure of coil elements that alters the coil homogeneity, and signal contributions from outside the FOV. Other factors such as leakage in the RF shielding of the MRI room, electromagnetic interference from high-amperage power lines or transformers, and moving metal objects like elevators or rolling carts, may all contribute to system noise (Silva & Merkle, 2003).

Even though technological and computational advances have minimized the occurrence and effects of these sources of system noise, MR centers have a responsibility to ensure and maintain the integrity of their MR scanners and environment. Moreover, MRI scanner operators and researchers should familiarize themselves with the ever-improving quality assurance procedures to limit the effects of system noise and provide feedback to the MR center whenever necessary.

Noise due to unrelated neural activities or variation in task performances

In task-based fMRI, the performance of a subject in executing the same task repeatedly usually varies especially when experiments constitute complex tasks. The response time for instructions varies between subjects (inter-subject) and between tasks performed by an individual (intra-subject). Moreover, during fMRI acquisition, the subject may focus on the scanner's sound, think about other unrelated issues, recalling bad or good memories and so on. Such unrelated stimuli activate neural processes that require a metabolic response, thereby creating BOLD contrasts unrelated to the task. Schemes to reduce the effects of mis-timings and inconsistencies in task responses and engagement include careful design of fMRI experiments (Amaro & Barker, 2006), calibrating individual- and region-specific BOLD responses (Thomason et al., 2007), and training subjects on the task before starting the scan (De Bie et al., 2010).

Noise due to head motion

In fMRI, head motion is the most common source of confounding artifacts. These include ghosting, blurring, signal dropout, spikes and image deformation, which all arise from inconsistent k-space filling (Zaitsev et al., 2015). Moreover, depending on the severity and pattern of motion, it can result in loss of slices in 2D acquisitions when large through-plane

motion occurs, false activations when the motion is temporally correlated with the functional task (for example when the task induces motion), complex artifacts when compounded with other noise, or complete data corruption. Various techniques have been developed to eliminate or minimize head motion through restraining devices, or to limit its effects by detecting and correcting for subject motion. However, because of the unpredictability and limitless variability in subject motion during scanning, there is not a single motion correction technique that is suitable for all fMRI acquisitions.

Since this work focuses on developing an alternative motion detection and correction technique for fMRI acquisitions, the following sections will focus on subject motion and motion correction techniques that have been implemented in fMRI.

1.3. Subject Motion in fMRI

fMRI measures the temporal evolution of the MR signal in every voxel of the brain image, which is acquired by scanning a subject repeatedly while performing a task. If the subject lies motionless in the scanner, each voxel will correspond to the same anatomical location on every repeated image (Chen & Glover, 2015; Goebel et al., 2006). For instance, a voxel $v(x, y, z)$ in an fMRI image may correspond to an anatomical location centered at $a(m, n, o)$. However, if a subject changes pose during scanning, $v(x, y, z)$ in the fMRI image may thereafter correspond to a new anatomical location centered at $a(m \pm \Delta m, n \pm \Delta n, o \pm \Delta o)$, where $\Delta m, \Delta n \text{ or } \Delta o \neq 0$, until the subject returns exactly to his/her original position. Therefore, the intensity of $v(x, y, z)$ corresponds to the MR signal from physical locations centered at $a(m, n, o)$ and $a(m \pm \Delta m, n \pm \Delta n, o \pm \Delta o)$ before and after the pose change, respectively. This violates the basic assumption of fMRI imaging which is that each voxel consistently contains MR signal from the same anatomical location.

Ideally, fMRI scanning requires subjects to be motionless (i.e., $\Delta m, \Delta n$ and $\Delta o = 0$) during scanning. Given the relatively long scan times, even healthy, motivated, and coached volunteers to remain motionless–usually they induce up to 2 mm of translational or 1º of rotational motions–during scanning (Zaitsev et al., 2017). The problem of subject motion during scanning is prevalent in clinical fMRI of children, elderlies, and patients. Moreover, the type and severity of subject motion depend on factors like the experiment, age, sex and condition or state of the subject during scanning (Hausman et al., 2022; Mayer et al., 2007; Poldrack et al., 2002; Seto et al., 2001; Yuan et al., 2009). Given the unbounded and limitless nature of these factors, subject motion remains a persistent source of artifacts in fMRI.

1.3.1. Subject motion induced artifacts in fMRI

An MR image $I(x, y, z)$ is generated by applying an inverse Fourier transform (see equation (1.11)) to k-space data $K(k_x, k_y, k_z)$; k-space is the Fourier transform of the spatially encoded MR signals of image $I(x, y, z)$.

$$I(x, y, z) = \iiint K(k_x, k_y, k_z) * e^{i2\pi(xk_x + yk_y + z\,k_z)} dk_x dk_y dk_z \qquad (1.11)$$

Fourier transformation of the MR signal from image space into k-space maps translations to a linear phase shift, and rotations to a rotation in k-space (Bernstein et al., 2004; Paschal & Morris, 2004). Therefore, considering only subject motion during scanning, translational motion induces linear phase variation into the k-space data in the direction of motion and rotational motion rotates the k-space data by the same degree. Motion induced phase changes and rotations create k-space data inconsistency during image construction (equation (1.11)), which assumes that the k-space data is the Fourier transform of motion-free MR signals. Usually, subject motion during scanning have both translational and rotational components which may manifest as artifacts in fMRI images. In 2D fMRI, spoiling after each slice acquisition prevents the spin-history artifacts that are caused by through-plane motion (Yancey et al., 2011). However, through-plane motion between slice excitation pulses may result in "double excitation" of the same brain region. This manifests as a slice-direction 'striping' artifact. In addition, motion alters the homogeneity of the static magnetic field, which was optimized before the start of the scan by the shimming coils. Shimming is most critical in regions with large magnetic susceptibility differences such as frontal sinuses (Jezzard, 2012; Jezzard & Clare, 1999; Ooi et al., 2013). Since subject motion during scanning moves these regions to new locations, field homogeneity will be compromised resulting in geometric distortions, spikes, and signal dropout.

The effect of subject motion on fMRI data depends on the type and severity of motion, the imaging parameters, the MR pulse sequence and k-space filling trajectory, and the structure of the target. To minimize motion artifacts in fMRI, the first logical step is therefore to minimize or if possible, avoid subject motion during scanning.

1.3.2. Avoiding subject motion in fMRI

A key strategy in fMRI data acquisition is to ensure that the subject is comfortable by using cushions, blankets, and/or sheets. To further minimize head motions, additional cushions and inflatable pads are inserted in spaces between the subject's head and the head-coil so that the head does not have room to move significantly. Additional procedures such as familiarizing

subjects with the MRI scanner, its noise, and the fMRI experimental task (if any) using mock scanner training all help to reduce anxiety related subject motions (De Bie et al., 2010).

In infants and young children (if no task is required), scanning is often performed during natural sleep to minimize motion. However, the loud banging scanner noises may wake the infant. Sedation, on the other hand, requires additional drugs, equipment, and anesthesiologist, which increases cost (Altman & Bernal, 2015; Bernal, 2012). Moreover, sedation is not always effective because subjects react to anesthetic drugs differently, anesthetic drugs have negative side effects, and using sedation for research procedures is ethically questionable (Andropoulos & Greene, 2017). Moreover, most fMRI experiments require subjects to be awake to engage with the task.

In older children and adults, devices like bite bars (Menon et al., 1997) and helmet head restraining systems (Hadj-Bouziane et al., 2014) have been used to avoid or minimize subject motion during scanning. However, biting a bar is itself a task which may confound activation by the experimental task, is uncomfortable, and bite bars require sterilization before and/or after use. Helmets, on the other hand, incur additional costs, may be head-size specific, and limit the use of additional equipment such as electroencephalography (EEG) electrodes.

1.4. Motion correction in fMRI

Despite employing these techniques and devices to minimize subject motion during scanning, motion artifacts are still prevalent in fMRI. Therefore, various motion correction techniques – broadly classified as retrospective or prospective – have been developed.

1.4.1. Retrospective motion correction (RMC)

Retrospective motion correction techniques attempt to correct for the effects of motion after acquisition of the complete dataset. Retrospective motion correction is available and has been optimized for rapid 2D imaging protocols in all the widely used fMRI analysis packages such as AFNI, FSL, SPM and BrainVoyager (Cox, 1996; Karl J. Friston et al., 1995; Goebel et al., 2006; Jenkinson et al., 2002). In these implementations the motion is considered to be slow relative to the sampling window, and RMC typically involves only inter-volume image-based registration. Although different packages use different algorithms, they ultimately result in similar activations (Oakes et al., 2005). The performance of these RMC implementations depend on the underlying interpolation algorithms and optimization of cost functions. Insufficiently corrected or uncorrected subject motion artifacts may manifest as signal changes in brain regions near high contrast borders, and, if they are correlated to the functional task,

may result in false activations (Field et al., 2000; Hajnal et al., 1994). In resting-state fMRI, where there is no functional task, head motion decreases the intrinsic functional connectivity (FC) in large-scale networks such as the default mode network, but increases FC in local networks such as between right and left motor regions (Power et al., 2012; Satterthwaite et al., 2012; van Dijk et al., 2012). In general, some components of motion-induced functional networks remain after retrospective motion correction (Yan et al., 2013).

For acquisitions with longer sampling windows, intra-volume motion, however, is non-negligible. Intra-volume motion may result in motion-related artifacts and/or spin-history signal deviations (Power et al., 2014; Satterthwaite et al., 2013). Slice-to-volume registration has been implemented in some 2D fMRI analysis packages to retrospectively correct for intra-volume motion. Self-navigation is another intra-volume RMC technique that involves sampling specific regions of k-space repeatedly so that motion during the acquisition of the volume can be estimated from discrepancies between these repeatedly-filled k-space regions. For instance, the PROPELLER (**P**eriodically **R**otated **O**verlapping **P**aral**EL** **L**ines with **E**nhanced **R**econstruction) acquisition scheme fills rotating parallel k-space lines also known as 'stripes' until a circular k-space region is completely filled (Krämer et al., 2012; Pipe, 1999). Oversampling of the centre of k-space allows motion to be estimated; minimal motion is assumed within stripes.

Intra-volume RMC becomes more critical for 3D acquisition schemes, where the sampling window is much longer. TURBINE (**T**rajectory **U**sing **R**adially **B**atched **I**nternal **N**avigator **E**choes) is a modification of the 2D PROPELLER approach that uses a 3D hybrid radial-Cartesian EPI readout scheme. It is a multi-shot technique where each shot uses an EPI readout to construct a 2D plane (called a 'blade') with phase encoding along k_z; subsequent planes are rotated about the k_z axis to fill a cylindrical k-space region (Graedel et al., 2017, 2022). However, because of the hybrid k-space sampling, magnetic field changes create phase inconsistencies between planes. The multi-shot acquisition also makes TURBINE more sensitive to physiological noise, motion, and magnetic field inhomogeneities. Moreover, TURBINE has lower BOLD sensitivity than matched 3D EPI acquisitions, and radial sampling has been shown to be less efficient than Cartesian sampling (Tsai & Nishimura, 2000).

The availability of vast numbers of annotated MR images, advances in graphic processing unit (GPU) technologies and mathematical models have accelerated the integration of machine learning (ML) algorithms into MRI data processing. ML algorithms implemented over interconnected computing units known as artificial neural network can be used to automatically

detect abnormalities in structural brain images by evaluating MR images of the same contrast and voxel geometry as the training data without localizing the artifacts or determining what the artifacts are (Esses et al., 2018; Sujit et al., 2019). Furthermore, various neural network architectures such as convolutional neural networks (CNNs) have been used to remove motion artifacts from contrast enhanced liver MR images, out-of-FOV motion artifacts from T1-weighted brain images and abdomen, and generative adversarial networks (GANs) were used to remove rigid and non-rigid motion artifacts. However, in addition to their demand for high computing resources, their performance depends on factors such as the size and quality of the training data, the quality and selection of input data, and optimization of parameters. In general, although preliminary applications of ML for retrospective motion correction have been promising, its clinical use has not been established (Armanious, Gatidis, et al., 2020; Küstner et al., 2018; Tamada et al., 2020; Wang et al., 2020).

1.4.2. Prospective motion correction

In contrast to RMC, prospective motion correction (PMC) aims to maintain the relative position of the target in the imaging field of view (FOV) by tracking the position of the target and readjusting the FOV in real time throughout the acquisition. PMC techniques sufficiently suppress spin-history effects (Yancey et al., 2011), intra-volume distortions (Speck et al., 2006) and contain all images of the target object within the acquisition FOV. Moreover, since retrospective motion correction is usually part of standard fMRI preprocessing pipelines, employing PMC during fMRI acquisition will further improve the integrity of the data (Aksoy et al., 2012; Boegle et al., 2010; MacLaren et al., 2011).

PMC techniques may detect subject motion in real time by using motion tracking schemes that involve attaching RF coils (Derbyshire et al., 1998; Ooi et al., 2009) or optical markers (Todd et al., 2015; Zaitsev et al., 2006) to a subject's head. However, both of these require additional hardware with their own setup, configuration and calibration requirements, thereby increasing both financial and time costs. Moreover, depending on marker fixation, subject motion may not accurately translate into tracker motion. An alternative approach is to use software-based motion trackers called navigators. These can be 1D, 2D or 3D low-resolution MR images acquired in an interleaved fashion throughout the acquisition to measure pose changes (Hess et al., 2011; Tisdall et al., 2012; Van Der Kouwe et al., 2006; White et al., 2010; Zhuo Wu Fu et al., 1995). However, navigators require additional RF and gradient pulses, which are difficult to implement in the already crowded EPI pulse sequence without increasing the acquisition time.

1.4.3. Self-navigated prospective motion correction ($snPMC$)

Here we propose implementing in repeated 3D-EPI a prospective intra-volume motion correction technique that does not require additional pulses or hardware to track subject motion in real time, referred to as self-navigated prospective motion correction ($snPMC$).

A 3D-EPI sequence was modified to acquire volumetric MRI data in a centre-out scheme, filling the 3D k-space from the centre partition and progressing outwards alternately filling one partition on either side of the centre partition. The sequence was also modified to readjust the acquisition FOV immediately after receiving motion parameters from the image reconstruction pipeline (IRP). The IRP was modified to accumulate subsets of partitions from the volumetric MRI data being acquired in dedicated storage(s) to construct a volumetric image(s), also referred to as a self-navigator(s), which could be used to estimate the current position of the target object relative to its position during the first acquisition. During each volume acquisition, except for the first, the IRP therefore estimates the position of the target and sends motion parameters back to the 3D-EPI sequence to update the FOV. The 3D-EPI readjusts its FOV immediately after receiving motion parameters from the IRP and acquires the remaining partitions of the current volume and the first partitions of the next volume, until new motion estimates are received, using the new FOV. The spatial resolution of the self-navigators was kept identical to the volumetric image being acquired using zero-filling of the remaining partitions. The $snPMC$ technique does not require additional time to detect and correct head motion. In this work, the single navigator used for $snPMC$ is referred to as a volumetric self-navigator ($vSNav$), and when two navigators per volume were used, these were referred to as double volumetric self-navigators ($dvsNav$).

Given that the 3D-EPI sequence samples 3D k-space and is therefore not affected by slice 'gaps' or 'double excitation' of slices as in 2D-EPI, motion correction could theoretically have been applied retrospectively by regridding k-space. In the presence of rapid head motion, regridding may, however, result in gaps in k-space, which cannot be corrected retrospectively. Moreover, RMC cannot correct 'slab' history effects (similar to slice history effects in 2D-EPI) that may occur when 3D-EPI is performed in thin slabs to increase resolution and minimize physiological artifacts.

Chapter Two

2. Self-navigated Prospective Motion Correction for 3D-EPI Acquisition[1]

Samuel G. Bayih[2,3], Marcin Jankiewicz[2,3,4], Ali Alhamud[2,4,5], André J. W. van der Kouwe[2,6,7] and Ernesta M. Meintjes[2,3,4]

Abstract

Purpose: Although three-dimensional EPI (3D-EPI) is more susceptible to motion artifacts than two-dimensional EPI, it presents some benefits for functional MRI (fMRI), including the absence of spin-history artifacts, greater potential for parallel imaging acceleration and better functional sensitivity in high-resolution imaging. Here we present a self-navigated 3D-EPI sequence suitable for prospective motion corrected fMRI without additional hardware or pulses. **Methods**: For each volume acquisition, the first 24 of the 52 partitions being acquired are accumulated to a new feedback block that was added to the image reconstruction pipeline. After zero filling the remaining partitions, the feedback block constructs a volumetric self-navigator ($vSNav$), co-registers it to the reference $vSNav$ acquired during the 1st volume acquisition and sends motion estimates to the sequence. The sequence then updates its FOV and acquires subsequent partitions with the adjusted FOV, until the next update is received. The sequence was validated without and with intentional motion in phantom and in vivo on a 3 T Skyra. **Results**: For phantom scans, the FOV was updated 0.704 s after acquisition of the $vSNav$ partitions, and for in vivo scans after 0.768 s. Both phantom and in vivo data demonstrated stable motion estimates in the absence of motion. For in vivo acquisitions, prospective head pose estimates using the $vSNav$'s and retrospective estimates with FLIRT agreed to within 0.23 mm (<10% of the slice thickness) and 0.14° in all directions. **Conclusion**: Depending on when motion occurs during a volume acquisition, the proposed method fully corrects the FOV and recovers image quality within one volume acquisition.

---

[1]Published in Magnetic Resonance in Medicine and reproduced with permission from John Wiley & Sons.

[2]Biomedical Engineering Research Center, Division of Biomedical Engineering, Department of Human Biology, University of Cape Town, Cape Town, South Africa
[3]Neuroscience Institute, Groote Schuur Hospital, University of Cape Town, Cape Town, South Africa
[4]Cape Universities Body Imaging Centre, University of Cape Town, Cape Town, South Africa.
[5]The Modern Pioneer Center and ArSMRM for MRI Training and Development, Tripoli, Libya
[6]A.A. Martinos Centre for Biomedical Imaging, Massachusetts General Hospital, Charlestown, USA.
[7]Department of Radiology, Harvard Medical School, Boston, USA.

2.1. Introduction

Functional MRI (fMRI) routinely uses echo planar imaging (EPI) (Stehling et al., 1991; Turner et al., 1991), which on a 3 T scanner can image the entire brain at roughly 3 x 3 x 3 mm^3 isotropic resolution in about 1 to 2 s. FMRI non-invasively measures brain activity by exploiting the coupling between neural activation and changes in blood oxygenation. The latter causes subtle contrast variations on T_2^* weighted images, known as blood-oxygenation-level-dependent (BOLD) contrast (Belliveau et al., 1991; Ogawa et al., 1992, 1993). The BOLD contrast, however, typically accounts for no more than 1% of the average MR signal intensity (Buxton, 2009; Huettel et al., 2014). This is comparable to and often less than contrasts created by other factors such as noise from cyclic cardiac and respiratory changes, instrumental drifts, external interferences and subject motion during scanning (Birn et al., 2006; Krüger & Glover, 2001; Shmueli et al., 2007).

Subject motion alters the evolution of the voxel-wise BOLD signal used to construct a functional map of the brain by causing signal from different anatomical regions to contribute to the time course of a single voxel. Moreover, head pose changes may change the macroscopic static (B0) and transmitted (B1) field at some voxels (Chen & Glover, 2015; Goebel et al., 2006). Avoiding or minimizing the effects of subject motion during fMRI data acquisition is therefore critical for a better BOLD signal extraction and a reliable functional analysis outcome. Remaining motionless throughout a 5- to 10-minute fMRI acquisition is, however, not trivial, and performing a task may cause involuntary motion. The difficulty becomes greater and subject motion more prominent in clinical sessions, or with young or elderly subjects. Besides, the pattern and intensity of head motion may vary depending on the type of experiment, as well as the age, sex and state of a subject during scanning (Mayer et al., 2007; Poldrack et al., 2002; Seto et al., 2001; Yuan et al., 2009), making head motion difficult to predict.

Head motion correction or minimization techniques typically combine one or more of the following schemes. The first aims to physically minimize head motion by using restraining objects like bite bars (Menon et al., 1997), helmets (Hadj-Bouziane et al., 2014), cushioning or sedation (Bernal, 2012). Even though these techniques reduce the amount of head motion they can introduce other problems. For instance, biting a bar is itself a task requiring effort during the scan and is uncomfortable. Helmets incur additional financial costs, may be head size specific and limit the use of additional equipment, such as EEG electrodes. Sedation is typically

not viable when a participant is required to perform a task, may affect fMRI signals, and presents ethical issues in research participants.

Retrospective motion correction, which estimates and corrects head motion after the data have been acquired, is implemented in most fMRI analysis packages (Liu, 2016). However, depending on the type of motion, motion correction after data acquisition may introduce subtle errors in the results. For instance, if the head motions are task correlated and are not sufficiently corrected, then the functional analysis may produce false activations. On the other hand, if head motion is not task correlated and not sufficiently corrected, then the resulting uncorrelated highly modulated signals may be processed as noise resulting in a decreased BOLD activation. Depending on the degree, head motion can create different levels of systemic effects by decreasing functional couplings between distributed regions of association cortex and by increasing local functional couplings (Hajnal et al., 1994; Power et al., 2012; Satterthwaite et al., 2012; van Dijk et al., 2012). Moreover, spin-history artifacts caused by through-plane motion may result in signal fluctuations that are comparable to BOLD signal contrast, making them difficult to remove retrospectively (Muresan et al., 2005; Yancey et al., 2011).

The final scheme, termed prospective motion correction (PMC), aims to keep the imaging field of view (FOV) fixed to the subject's head (rather than the scanner) by measuring head motion throughout the acquisition and realigning the imaging coordinates whenever head motion is detected. One approach involves attaching fixed markers, such as coils (Derbyshire et al., 1998; Ooi et al., 2009) or optical markers (Todd et al., 2015; Zaitsev et al., 2006), to a subject's head to track motion. These trackers, however, require additional hardware with their own setup and calibration requirements, increasing financial and time costs. An alternative approach uses software-based trackers termed navigators (Alhamud et al., 2012; Hess et al., 2011; Van Der Kouwe et al., 2006; Zhuo Wu Fu et al., 1995), which are acquired repeatedly throughout the acquisition and provide one-, two- or three-dimensional low-resolution snapshots of the location of an anatomical region. Previously, we implemented a low-resolution (8 x 8 x 8 mm^3) three-dimensional (3D) EPI volumetric navigator ($vNav$) for PMC during neuroanatomical acquisition (Tisdall et al., 2012), MR spectroscopy (Hess et al., 2011) and diffusion tensor imaging (Alhamud et al., 2016). Although these $vNav$'s require no external hardware, the parent sequence needs to be interrupted for 355-475 ms while the $vNav$ is acquired, reconstructed, registered and motion estimates are fed back to the parent sequence. While the inversion and recovery times in neuroanatomical and spectroscopy acquisitions are sufficient for insertion of the $vNav$ block, the repetition time (TR) for DTI had to be increased

slightly (Alhamud et al., 2016). In each application, motion is measured and feedback provided at the start of each measurement, which for MRS and neuroanatomical acquisitions occurs every 2-5 s (Hess et al., 2011; Tisdall et al., 2012) and for DTI every 10 s (Alhamud et al., 2012). In the present work, we wanted to explore the feasibility of implementing PMC for fMRI using a subset of the data being acquired by the parent sequence, without having to interrupt the measurement to play out the dedicated radiofrequency (RF) and gradient pulses required for the $vNav$ acquisition.

Prospective acquisition correction (PACE) (Thesen et al., 2000) for fMRI employs a similar strategy where each 3D volume (comprising a stack of slices) as soon as it becomes available is registered to a reference volume, whereafter motion estimates are fed back to the sequence and the scanner FOV is updated. However, since image reconstruction and registration are performed during acquisition of the next volume, the correction is only applied to the second next volume, resulting in a lag of up to two TRs (Tisdall et al., 2012; Zaitsev et al., 2017). Recently, (Hoinkiss et al., 2019) reduced the latency to around 300 ms by using multi-slice-to-volume image registration in combination with simultaneous multi-slice (SMS) imaging. However, this technique is necessarily limited to two-dimensional (2D) EPI where the volume is imaged slice by slice.

Although 2D-EPI is typically preferred for fMRI due to its greater motion robustness and relative speed, 3D-EPI may have some advantages. 3D-EPI excites the entire volume simultaneously and records signals for successive k_z partitions, filling the entire 3D k-space grid before image reconstruction. Specifically, the additional phase encoding gradient for partition encoding in 3D-EPI lends itself to parallel imaging acceleration (Afacan et al., 2012). In contrast, SMS acceleration in 2D-EPI increases the RF power requirements, which increases the average specific absorption rate (SAR) and homogeneity requirements of the transmit field (B1) (Le Ster et al., 2019; Moeller et al., 2010). Moreover, 3D-EPI is free from spin-history artefact problems and its functional sensitivity is better than (or comparable to) 2D-EPI (Goerke et al., 2005; Neggers et al., 2008; Poser et al., 2010; Stirnberg et al., 2017).

To date, the only PMC technique that has been applied to 3D-EPI fMRI data is optical tracking (Todd et al., 2015). PACE has not been implemented for 3D-EPI. Since PACE requires the complete image volume to be reconstructed prior to registration, PMC of 3D-EPI using PACE would, however, be delayed by at least one volume, irrespective of computational power. In this work, we propose a self-navigated PMC framework with reduced latency. The method eliminates the limitations of external hardware, as well as the need for additional

motion tracking pulses, by using a subset of the acquired kz partitions to construct a 3D volumetric self-navigator ($vSNav$) during each volume acquisition. The $vSNav$'s acquired in successive volume acquisitions are compared to a reference to estimate motion parameters, and corrections are applied to the imaging FOV before the start of the next volume acquisition.

2.2. Methods

2.2.1. Self-navigated 3D-EPI sequence Development

The multi-shot 3D-EPI sequence acquires a complete volume by repeatedly exciting the volume. After each excitation, a different partition encoding gradient is applied and one kz partition is filled along a Cartesian trajectory. A typical acquisition scheme, called the center-out scheme, starts from the central partition, filling partitions on either side of the central partition and moving outwards one partition at a time (Figure 2-1 (a)). In principle, it should be possible to construct a volumetric image from a subset of these partitions, thereby permitting motion detection before all partitions for the volume have been acquired. In this work, we added an additional block – termed the feedback block – to the image reconstruction pipeline (IRP) (Figure 2-2). This block accumulates the same data as the online block, albeit only for a subset of the partitions, and processes these partitions independently to compute motion estimates during the acquisition of the volume. The sequence was further modified to accept motion parameters fed back to it by the feedback block once during the acquisition of a particular volume, and to adjust the FOV based on this feedback.

2.2.2. Volumetric self-navigator design

To detect and measure motion, we construct a $vSNav$ once per volume acquisition from the subset of k-space data accumulated to the feedback block. The $vSNav$ of volume i ($vSNav_i$) is constructed by accumulating the first m partitions to the feedback block. To optimize the signal of our $vSNav$, we use the center partitions that contain more energy due to smaller encoding gradients. Combined with a center-out acquisition scheme, these partitions are acquired first, allowing sufficient time during acquisition of the remaining partitions for computations. The number of partitions, *m,* depends both on the minimum number of partitions required to construct a navigator volume with sufficient features for accurate motion detection, the time at which we would like to estimate motion during acquisition of a volume, and the time required to complete all computations and provide feedback before the start of the next volume acquisition. In the current implementation where we only construct one navigator during acquisition of a volume, m was chosen to provide feedback on motion that occurred

before or during the first half of each volume acquisition. The remaining $(n - m)$ partitions of $vSNav_i$ are zero filled, which is equivalent to applying a low pass filter along the partition direction (Figure 2-1(b)). In this manner the volumetric self-navigator has isotropic resolution that is low pass filtered in partition direction.

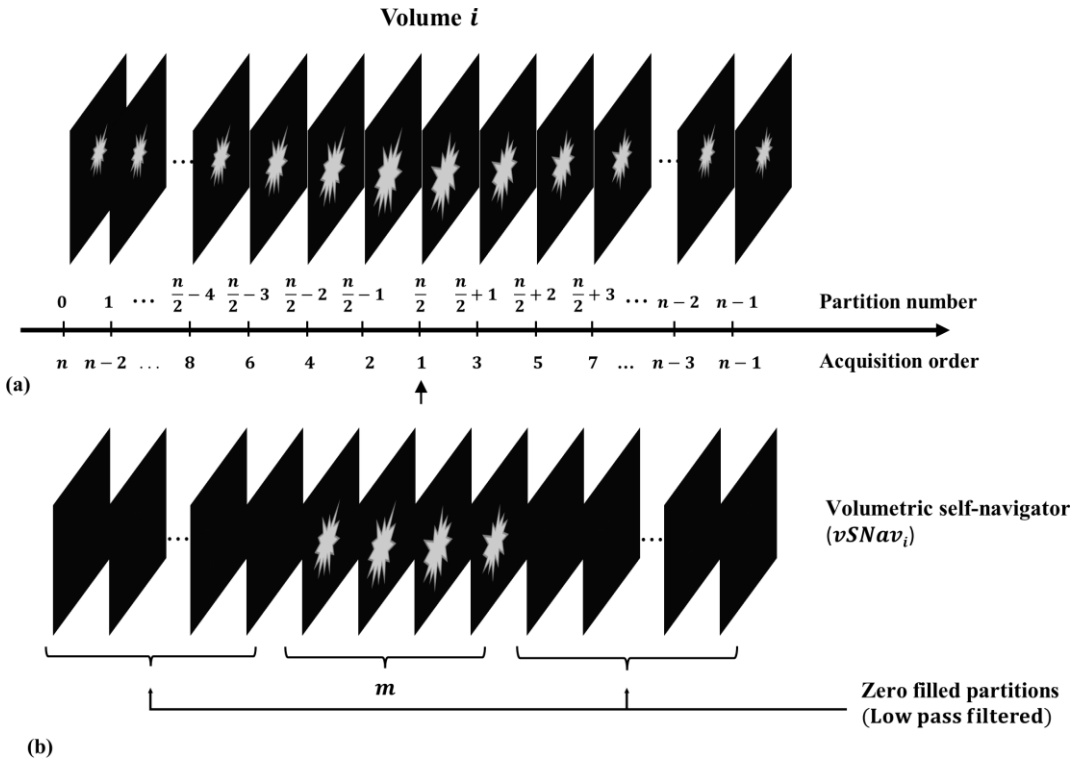

Figure 2-1 Position of partitions with respect to the isocenter and design of the volumetric self-navigator for volume i. (a) n partitions and their position relative to the isocenter (indicated by the arrow), as well as the order in which they are acquired with the centre-out scheme. (b) The volumetric self-navigator of the ith volume ($vSNav_i$) is constructed from the first m partitions, which are accumulated to both the online and feedback blocks. The remaining $(n - m)$ partitions in the feedback block are zero filled, which is equivalent to applying a low pass filter.

2.2.3. Real-time motion detection

The first $vSNav$ is set as a reference volume ($vSNav_{Ref}$) relative to which motion parameters of subsequent self-navigators are estimated. The m partitions for each self-navigator are accumulated in a time $\Delta t_1 = m*TR$, where TR is the partition repetition time. Immediately after accumulation of the partitions, the feedback block constructs the self-navigator volume, and for $i > 1$, estimates the position of $vSNav_i$ relative to $vSNav_{Ref}$ using the Siemens PACE algorithm (Thesen et al., 2000). PACE outputs six motion parameter values – three for translation and three for rotation. Assuming that the feedback block requires a time Δt_2 to zero fill remaining partitions, reconstruct $vSNav_i$, perform the computations to estimate

the motion parameters, and send these back to the sequence, the imaging FOV will be updated at time $\Delta t_1 + \Delta t_2$ after the start of the i^{th} volume acquisition (Figure 2-3). The remaining partitions of the current volume, and the first m partitions of the next volume, are then acquired with the adjusted FOV (i.e., corrected for motion).

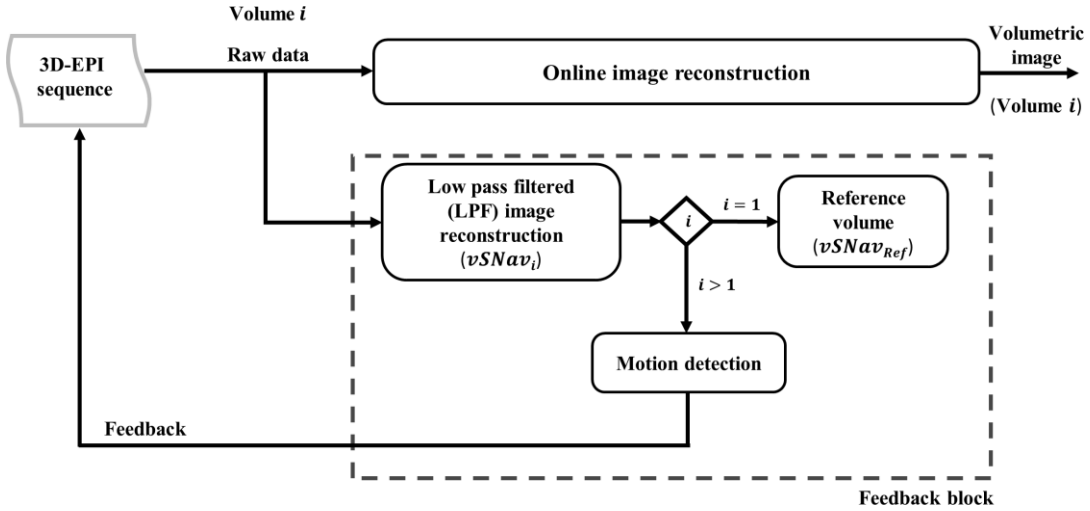

Figure 2-2 Block diagram illustrating the two blocks in the image reconstruction pipeline for the proposed self-navigated prospective motion correction scheme. The real-time feedback block (dashed rectangle) accumulates a sub-sample of the incoming data, fills remaining partitions with zero, reconstructs the self-navigator volume, estimates motion parameters by co-registering to the reference self-navigator volume, and sends the motion parameters back to the sequence. The sequence immediately readjusts the FOV according to the motion parameters received. The online image reconstruction block accumulates all acquired partitions (irrespective of FOV) and constructs a volumetric image at the end of every volume acquisition.

2.2.4. Real-time motion correction considerations

'Real-time' motion correction requires motion parameters to be fed back to the sequence before completion of a volume acquisition so that the remaining partitions of the current volume, or at the very least the partitions of the next volume, can be acquired with the updated FOV. For the method proposed here, the speed of motion detection is limited by the minimum number of partitions required to construct a $vSNav$ of sufficient quality for accurate co-registration to $vSNav_{Ref}$. Even with the in-plane resolution intact, using fewer partitions results in increased smoothing along the partition direction. Notably, the minimum number of partitions required will also be affected by which partitions are accumulated in the feedback block – using partitions with only high spatial frequencies may not contain sufficient features, thereby decreasing the sensitivity of through-plane motion detection if the number of partitions is not increased. As such, implementing real-time motion correction using the proposed $vSNav$ approach requires a trade-off between when and how fast motion can be estimated during a

volume acquisition. To provide time for the feedback block to compute and send the motion parameters back to the sequence, remaining partitions are only accumulated to the online block.

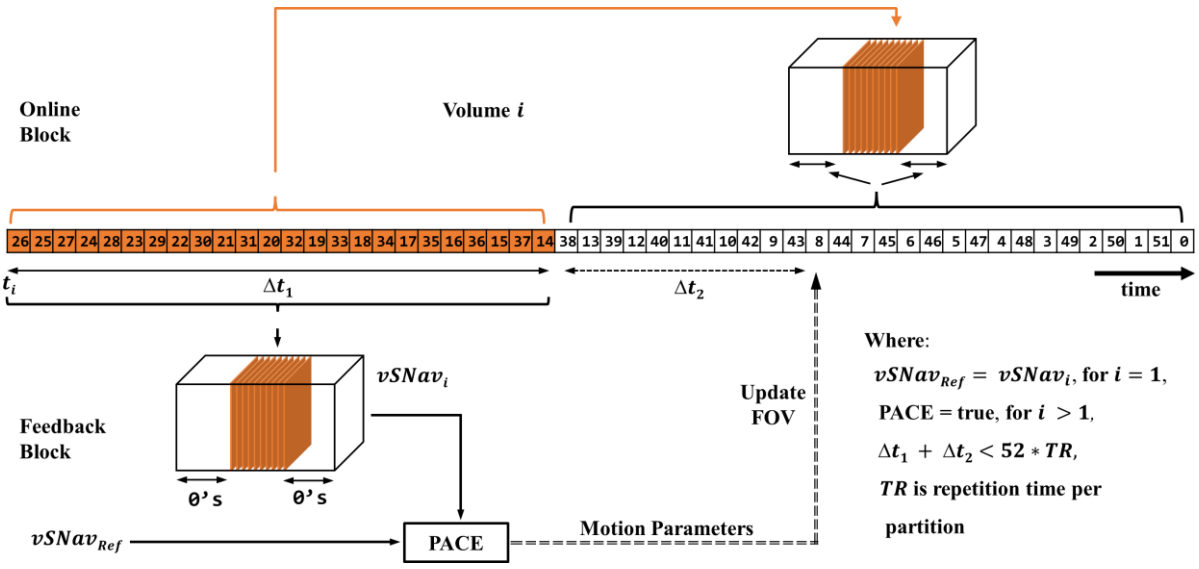

Figure 2-3 Illustration of the self-navigated prospective motion correction scheme for a single volume comprising 52 partitions. The feedback block takes time Δt_1 to accumulate the partitions for the volumetric self-navigator ($vSNav$), and time Δt_2 to zero fill remaining partitions, construct the i^{th} self-navigator, estimate its position relative to the reference self-navigator, and send motion estimates back to the sequence. All 52 partitions are accumulated to the online block in a time $52*TR$, where TR is the partition repetition time. In the current implementation, the first 24 partitions are used to construct the $vSNav$ and the remaining 28 partitions are accumulated to the online block only. Image reconstruction of the i^{th} volume occurs after accumulation of all 52 partitions.

To determine the optimal number of partitions required for accurate motion detection, we scanned a High Precision Devices (HPD) system phantom (Figure 2-4) on a 3 T Skyra (Siemens Healthcare, Erlangen, Germany) using our 3D-EPI sequence without motion correction, while manually moving the pad supporting the phantom to the right at the start of volume 6 and then to the left at the start of volume 16. The phantom was scanned in a 20-channel Head/Neck coil. Sequence parameters were: TR 64 ms, $TRvol$ 3.33 s, TE 30 ms, voxel size 3.1 x 3.1 x 3.1 mm^3, acquisition matrix 64 x 64 x 52, FOV 200 x 200 mm^3, bandwidth 2298 Hz/px, flip angle 18^o, 24 volumes with fat saturation ON. Offline we constructed $vSNav$'s using either the first 8, 12, 16, 20, 24, 28, 32, 36, 40, 48 or all 52 partitions and estimated motion parameters for each $vSNav$ configuration. Since the $vSNav$ constructed using all 52 partitions ($vSNav52$) provides the highest accuracy achievable with PACE, the performance of all the other $vSNav$ configurations was compared to $vSNav52$.

Figure 2-4 High Precision Devices (HPD) system phantom model 130, which contains 5 plates, 57 fiducial spheres and 2 wedges, and its placement in the 20-channel head/neck coil.

Based on our results (Figure 2-5), showing that translations converge to within 0.2 mm of the ground truth for 20 or more partitions, and rotations to within 0.1 degree for 12 or more partitions, we used 24 of 52 partitions to construct our $vSNav$ in the current implementation (Figure 2-3). As such, $\Delta t_1 \cong (24) * TR$, where TR is the repetition time (TR) for each partition. For all measurements after the first, the feedback block estimates subject motion relative to the first measurement and feeds the motion parameters back to the sequence at time $(\Delta t_1 + \Delta t_2) < 52 * TR$ after the start of that measurement. To avoid oscillations arising from small registration errors, the feedback block was programmed to only send feedback to the sequence for translations exceeding 10% of the slice thickness or rotations exceeding 0.2°.

The online block of the IRP (Figure 2-3) first accumulates all partitions of the i^{th} volume acquisition before constructing the volumetric image. The quality of partitions that are accumulated and processed in this block is partly dependent on the performance of the feedback block. The performance of the feedback block depends on the number and position of partitions used to construct the self-navigators and the severity of subject motion, which also affects the quality of raw data that are accumulated to the online block. Only in two cases will the sequence not receive feedback from the feedback block: (i) if the subject motion is too severe (i.e. when estimated translation or rotation values are greater than $20\ mm$ or 8°, respectively), or (ii) if the self-navigators do not have enough features for PACE to estimate motion.

The online block of the IRP reconstructs and displays the slices of each volume in mosaic format. In addition to the online reconstruction and display, it also displays slices of the $vSNav$'s constructed by the feedback block in mosaic format and overlays the estimated motion parameters on the images to provide a summary of the self-navigator performance throughout the scan.

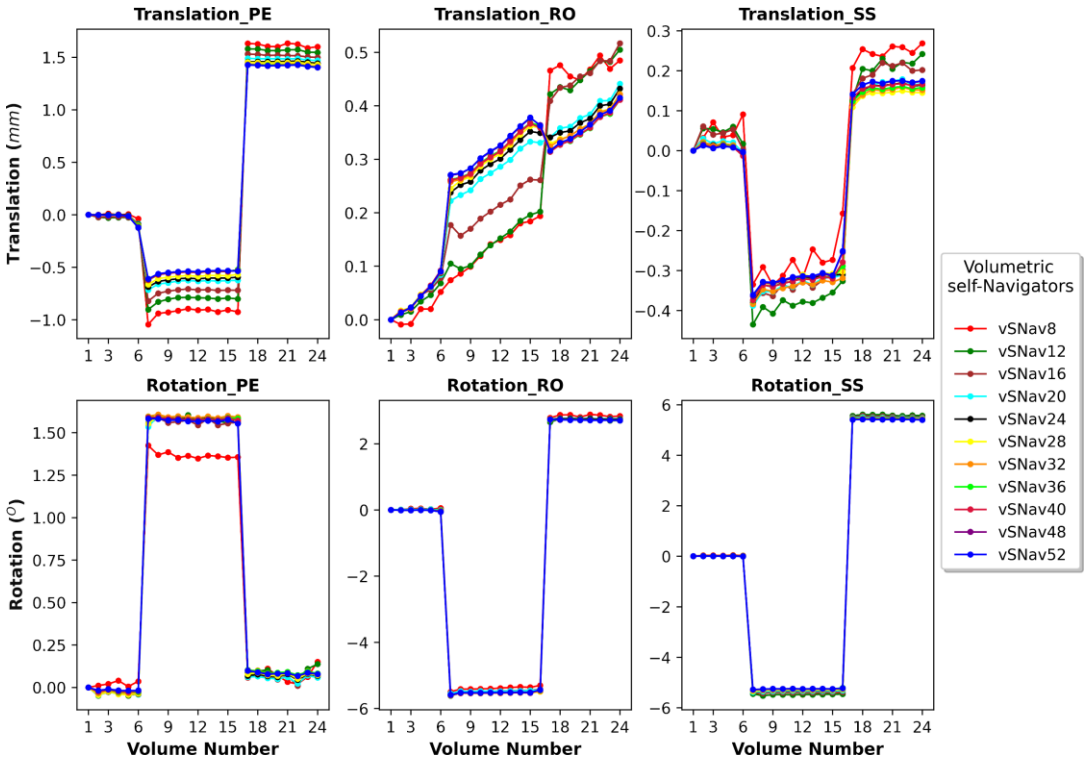

Figure 2-5 Plots comparing motion estimates for volumetric self-navigators (vSNav's) constructed from the first 8, 12, 16, 20, 24, 28, 32, 36, 40, 48 or all 52 partitions of each volume acquisition. Since the vSNav's constructed using all 52 partitions (vSNav52) provide the highest accuracy achievable with PACE, that is the ground truth that motion estimates of vSNav's constructed from a sub-sample of the partitions were compared to. For translations, accuracy converges to within 0.2 mm of the vSNav52 estimates for 20 or more partitions, and for rotations to within 0.1 degree for 12 or more partitions.

2.2.5. Sequence validation

The self-navigated 3D-EPI sequence was validated both in a phantom and in vivo in three healthy volunteers. All scans were performed on a 3 T Skyra (Siemens Healthcare, Erlangen, Germany) located at the Cape Universities Body Imaging Centre (CUBIC) in Cape Town, South Africa, according to protocols that had been approved by the Faculty of Health Sciences Human Research Ethics Committee of the University of Cape Town. The volunteers (age 30, 31 and 36 years, male) provided written informed consent.

For the phantom scans, sequence parameters were the same as above, except that 36 volumes were acquired. In vivo acquisitions were performed using a 32-channel head coil with the same sequence parameters, except for 80 volumes. Sequence parameters were selected to be similar to those typically used during an fMRI BOLD acquisition. The phantom images were acquired in the coronal orientation with slice select anterior-posterior and phase encoding

left-right. The in vivo images were acquired in the sagittal orientation with slice select left-right and phase encoding anterior-posterior.

The phantom was scanned first without motion and next with motion, in both instances with active motion correction. During the scan with motion, three discrete motions were induced manually by moving the pad supporting the phantom first to the right around the start of volume 4, then to the right around the start of volume 13 and finally to the left around the start of volume 25.

In vivo scans were performed first without motion while real-time motion detection and correction were active, second with intentional motion and real-time motion detection active, but no feedback applied, and finally, with intentional motion and both real-time motion detection and correction active. During the scans with intentional motion, participants were asked to move their heads at particular times during the acquisition, remaining still at each new position for about 20 volume acquisitions, as well as for the first and last 10 volume acquisitions. Specifically, the participants were asked to rotate their head to the right around volume 10, rotate back to the center around volume 30, rotate to the left around volume 50, and finally rotate back to the center around volume 70, remaining still until the end of the acquisition. In a separate acquisition, the 1st subject was asked to move directly from right to left around volume 30 instead of moving back to the center. The amount of motion was controlled by marking three dots on the inside surface of the scanner bore – one dot directly in line with the subject's line-of-sight (center mark), one dot approximately 8 cm to the left of the center mark, and another approximately 8 cm to the right of the center mark. When instructed to move, all participants turned their head to face the relevant mark (center, left or right). In vivo data were further processed using FLIRT in FSL (Jenkinson et al., 2002) to assess the accuracy of the motion parameters estimated by PACE.

2.3. Results

2.3.1. Phantom data

Figure 2-6 (a) shows that motion estimates for the phantom in the absence of motion are stable. Figure 2-6 (b) shows motion estimates when the phantom was moved during the beginning of the 4th (after the 3th) and 13th (after the 12th) volume acquisitions, and a small motion during the 24th and big motion during 25th volume acquisitions. Except for volume 24, motion was successfully detected during the volume acquisition in which it occurred, and the FOV updated before the start of the next volume acquisition. From the log viewer it was

confirmed that the last 17 partitions of the volume during which motion occurred were acquired with the updated FOV for the first and second motion instances, as well as partitions of the next volumes acquired before a new update was received. Even though there was continuous motion during the 24th and 25th volume acquisitions, the FOV was completely corrected by the 26th volume acquisition. Figure 2-6 (c) shows the central slice of the 1st volume, and Figure 2-6 (d-f) difference images between the central slices of volumes before and after motion occurred. Figure 2-6 (d) is the difference between the 3rd and 5th volumes, Figure 2-6 (e) between the 12th and 14th, and Figure 2-6 (f) between the 23rd and 26th volumes.

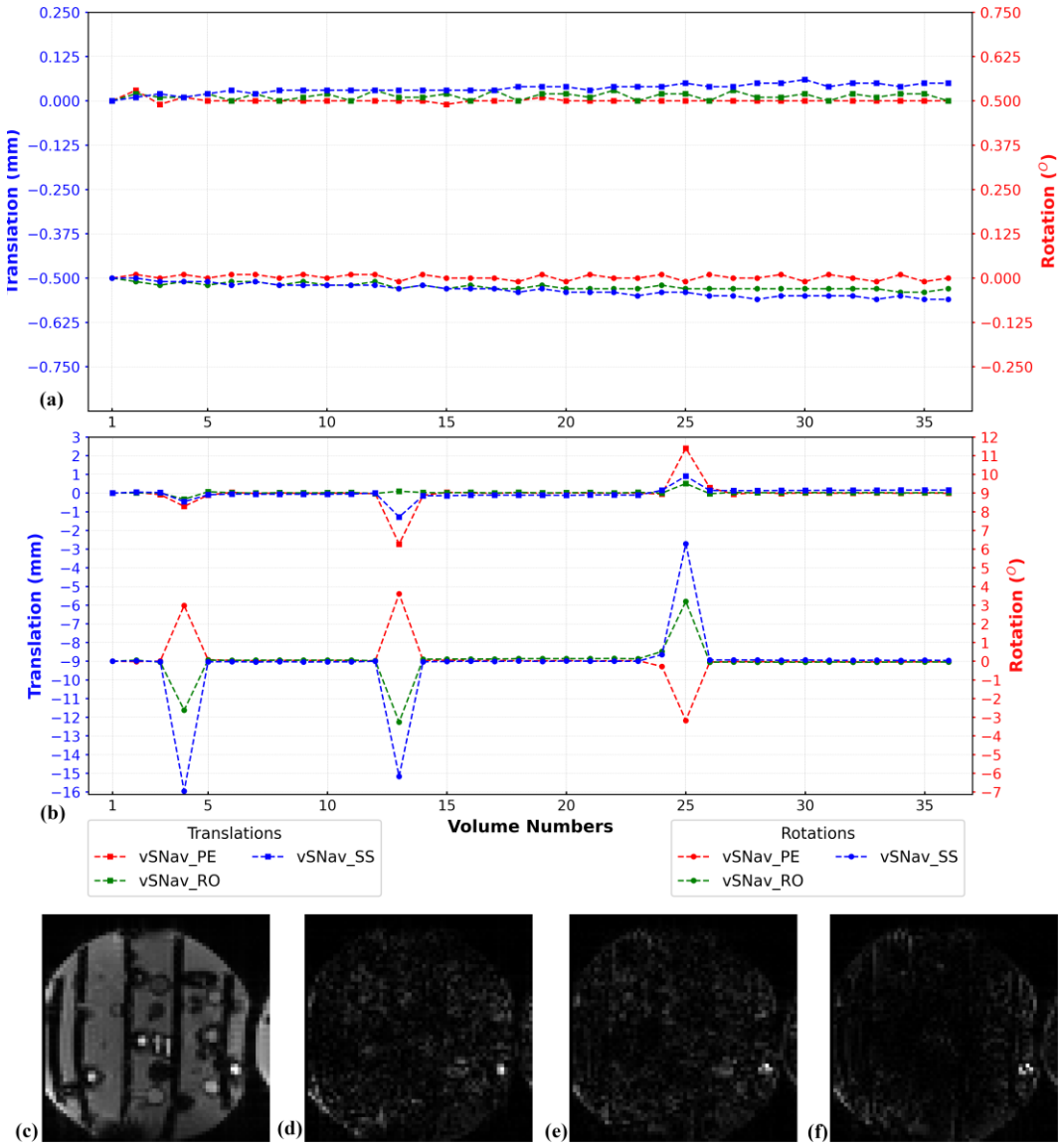

Figure 2-6 Plots showing for each volume the position of the phantom in the imaging FOV relative to its position during the first volume as measured by the volumetric self-navigator for acquisitions with (a) no motion and (b) motion induced during measurements 4, 13 and 25. Images were acquired in the coronal orientation with phase encoding in the left-right direction and readout in the inferior-superior direction. The images in the bottom row show (c) the central slice of the first volume, and difference images between the central slices acquired in (d) volumes 3 and 5, (e) volumes 12 and 14, and (f) volumes 23 and 26.

2.3.2. In vivo data

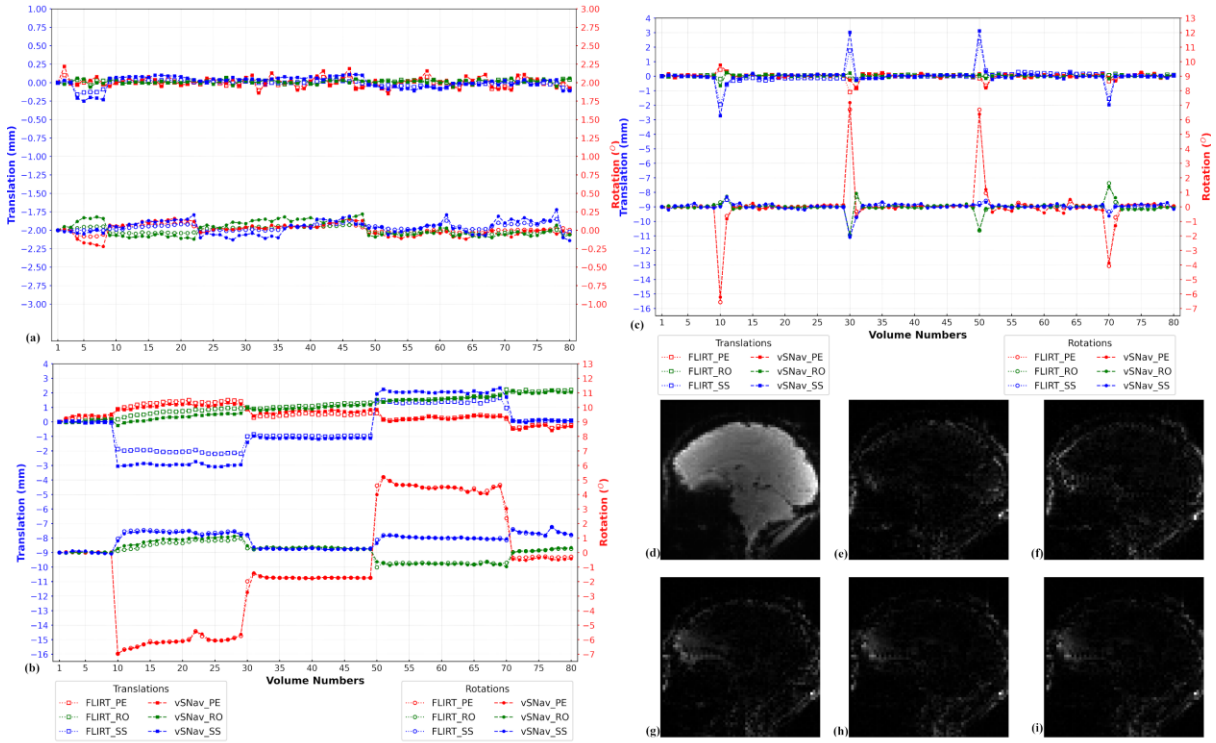

Figure 2-7 Plots showing for one volunteer prospective vSNav and retrospective FLIRT estimates of their head position in the imaging FOV during each volume relative to its position during the 1st volume for acquisitions (a) without intentional motion, (b) with intentional motion around volumes 10, 30, 50 and 70 but without feedback to the sequence, and (c) with intentional motion and both real-time detection and correction enabled. Since images were acquired in the sagittal orientation, the slice select direction is from left to right, phase encoding from anterior to posterior and readout from inferior to superior. For the acquisition with motion correction enabled, we show (d) a central slice of the 1st volume ($vSNav_{Ref}$) and (e-h) difference images of the same central slice between volumes acquired before motion occurred and after the head position within the imaging FOV is fully restored. In (e) we show the difference image between volumes 9 and 14, in (f) between volumes 29 and 33, in (g) between volumes 49 and 53, and in (h) between volumes 69 and 72. Notably, the motion around volume 30 involved substantial nodding compared to the other motion events. In (i) we show the difference image of the central slice before and after a period of continuous motion (i.e., between the 61st and 65th volumes).

Figure 2-7 shows for one volunteer how their head position in the imaging FOV changes relative to its position in the 1st volume for acquisitions (a) without intentional motion (NoMo), (b) with intentional motion but without feedback to the sequence enabled (NoCo), and (c) with motion and both feedback and real-time FOV updates enabled (MoCo). These estimates were determined prospectively by the $vSNav$ and retrospectively by FLIRT; all motion estimates were converted to the scanner coordinate system to facilitate comparison. Small oscillations in Figure 2-7 (a) demonstrate difficulties remaining motionless and potential effects of physiological noise during lengthy scans, especially when compared to the phantom scans shown in Figure 2-6 (a). As seen in Figure 2-7 (c), the head position largely returns to its

original position within the imaging FOV in the volume immediately following that during which motion is detected and the FOV update is applied. Figure 2-7 (d) shows a central slice of the 1st volume of the MoCo acquisition, and Figure 2-7 (e-h) the difference images of the same central slice between volumes acquired before and after motion occurred. In addition, we show in Figure 2-7 (i) the difference image between volumes acquired before and after the continuous motion detected between volumes 60 to 65 (Figure 2-7 (c)).

Table 2-1 shows the maximum, mean and standard deviation of the differences between position estimates obtained using the $vSNav$ and FLIRT for each acquisition of each subject. Notably, larger maximum and mean discrepancies are evident in most directions for acquisitions without motion correction. For NoMo and MoCo acquisitions, mean translation and rotation differences are below 0.23 mm and 0.14 degrees, respectively, and maximum differences below 1.5 mm translation and 1 degree rotation. The largest differences were seen for subject 2, who moved continuously between the 3rd and 4th motion event, and moved slower causing motion events to extend across more than one volume. Moreover, it can be seen in Figure 2-7 (b) and (c) that the largest discrepancies between the $vSNav$ and FLIRT occur in the volumes where motion is detected and that these tend to be largest along the slice select direction. This may in part be due to substantial smoothing along this direction, arising from more than half the partitions being filled with zeroes.

Table 2-1 Differences (maximum and mean) between PACE and FLIRT motion estimates for the 3 acquisitions of all 3 subjects.

Motion estimation difference	Motion parameter component	Logical coordinate system	Subject #1			Subject #2			Subject #3		
			NoMo	NoCo	MoCo	NoMo	NoCo	MoCo	NoMo	NoCo	MoCo
Maximum	Translation (mm)	PE	0.12	0.27	0.84	0.28	0.50	0.31	0.23	0.46	0.35
		RO	0.05	0.43	0.45	0.18	1.68	0.99	0.15	0.34	0.29
		SS	0.14	1.16	1.26	0.15	1.01	1.53	0.20	0.82	0.42
	Rotation (°)	PE	0.16	0.76	0.58	0.25	1.00	1.02	0.14	0.42	0.51
		RO	0.15	0.39	0.30	0.13	1.65	0.68	0.17	0.78	0.28
		SS	0.13	0.24	0.3	0.25	0.37	0.25	0.24	0.44	0.39
Mean (Standard deviation)	Translation (mm)	PE	0.03 (0.03)	0.14 (0.08)	0.06 (0.11)	0.09 (0.05)	0.24 (0.11)	0.13 (0.07)	0.05 (0.04)	0.34 (0.08)	0.06 (0.06)
		RO	0.02 (0.01)	0.16 (0.14)	0.06 (0.07)	0.07 (0.04)	0.55 (0.54)	0.17 (0.15)	0.06 (0.04)	0.09 (0.08)	0.06 (0.06)
		SS	0.04 (0.03)	0.45 (0.37)	0.15 (0.19)	0.04 (0.03)	0.12 (0.13)	0.23 (0.26)	0.06 (0.04)	0.29 (0.20)	0.07 (0.09)
	Rotation (°)	PE	0.04 (0.03)	0.07 (0.13)	0.11 (0.12)	0.08 (0.06)	0.28 (0.25)	0.14 (0.15)	0.05 (0.04)	0.19 (0.10)	0.09 (0.10)
		RO	0.05 (0.04)	0.10 (0.09)	0.06 (0.06)	0.05 (0.03)	0.37 (0.26)	0.13 (0.12)	0.06 (0.04)	0.30 (0.16)	0.07 (0.06)
		SS	0.05 (0.03)	0.05 (0.04)	0.07 (0.06)	0.06 (0.05)	0.13 (0.08)	0.07 (0.06)	0.09 (0.04)	0.24 (0.09)	0.07 (0.07)

Where: PE: **P**hase**E**ncode; **RO**: **R**ead**O**ut; **SS**: **S**lice**S**elect; **NoMo**: **No Mo**tion with motion correction; **NoCo**: motion with **No** motion **Co**rrection; **MoCo**: **Mo**tion with motion **Co**rrection

In a final in vivo experiment where the 1st subject moved his head from the left marker directly to the right during the 30th measurement, the estimated motion parameters exceeded the PACE limits (>20 mm translation or 8 degrees rotation). This caused the feedback block to stop so that no real-time motion detection nor correction occurred. However, the online block continued to accumulate and construct the remaining measurements.

2.4. Discussion

This work demonstrates that a new feedback block introduced in the IRP of the 3D-EPI sequence can compute motion parameters to within sub-millimeter accuracy from a volumetric image generated using a sub-sample of the partitions. These motion parameters are sent back to the sequence, allowing the FOV to be adjusted once per volume acquisition thereby enabling real-time motion correction.

It is worth highlighting that the proposed $vSNav$ differs fundamentally from the $vNav$ previously implemented by the authors. $vNav$ is an additional independent 3D-EPI volume acquired at repeated intervals during a measurement (which can be 2D or 3D), requiring the main measurement/parent sequence to be paused briefly (355-475 ms). The low resolution (8 x 8 x 8 mm^3) $vNav$ volume is constructed using its own dedicated RF and gradient pulses, and are unaffected by any contrasts (such as diffusion weighting) applied during the main measurement. To minimize any impact on the signal of the parent sequence, a small flip angle of 2 degrees is used. In contrast, the current self-navigators are constructed from a subset of the data being acquired as part of the main measurement. As such, the measurement never needs to be interrupted and no additional RF pulses or gradients need to be inserted during the acquisition. The current method is only suitable for 3D acquisition, as a subset of the kz partitions are used, and the remaining partitions are zero-filled to fill the complete 3D k-space matrix. The resolution of the $vSNav$ is therefore kept isotropic and smoothed only in the partition direction. Moreover, the flip angle is that of the main measurement. Here we use the Ernst angle (18 degrees) to optimize the BOLD contrast at 3 T.

In the current approach, partitions that are not accumulated to the feedback block, are zero filled, which occurs almost instantaneously. In addition to the time required to acquire the partitions accumulated to the feedback block (acquisition time), the feedback block requires a finite amount of time (computation time) for image reconstruction, registration, feedback and to apply FOV updates to the sequence. Since the $vSNav$ always comprises 52 partitions, the computation time is not affected by the number of partitions acquired. The computation time

of the feedback block does, however, appear to depend, in part, on both the number of receiver channels and the partition repetition time (TR). During phantom scanning where the 20-channel Head/Neck coil was used with TR 64 ms, the sequence FOV was updated after acquiring a further 11 partitions (0.704 s after acquisition of the self-navigator partitions). In contrast, sequence updates were only performed after acquisition of a further 12 partitions (0.768 s after acquisition of the self-navigator partitions) during in vivo scanning where the 32-channel head coil was used with the same TR. As a result, the last 17 partitions of the current volume (and the first 35 partitions of the next volume) were acquired with the adjusted FOV during phantom scans, but only the last 16 partitions of the current volume (and the first 36 partitions of the next volume) during in vivo scans. These times suggest that, for 52 partitions per measurement volume, our feedback block will be able to provide updates to the sequence before the start of the next volume acquisition for $vSNav$'s constructed using 40 or fewer kz partitions.

As shown in Figure 2-5, the accuracies of translation estimates approach those of PACE, which uses all 52 partitions, for $vSNav$'s constructed using 20 or more partitions, and rotation estimates for 12 or more partitions. Based on these results, we used 24 partitions for the current implementation.

The motion parameter plots and absence of features in the difference images between a central slice acquired immediately preceding and following a motion event (Figure 2-6 and Figure 2-7) confirm that the position of the object being scanned (phantom or head) approaches its original position within the imaging FOV in the volume following the one during which motion occurred. The phantom data in Figure 2-6 (a), which were acquired without motion but with real-time motion correction enabled, are stable and do not show any significant drifts. Even though the induction of the 3rd discrete motion in Figure 2-6 (b) extends across both volumes 24 and 25, the FOV was corrected by the feedback block in the 26th volume.

The in vivo data demonstrates that head pose changes measured prospectively by the $vSNav$'s and retrospectively by FLIRT using the measurement volumes agree to within sub-millimeter precision except in volumes during which motion occurred, for which discrepancies never exceeded 1.7 mm translation or 1.7 degrees rotation (Table 2-1). For the in vivo data acquired with motion correction enabled (MoCo), mean differences between $vSNav$ and FLIRT translation and rotation estimates were ≤0.23 mm and ≤0.14 degrees, respectively, in all directions. In all except the NoCo acquisition of volunteer 2, we find the largest mean and maximum differences between translation estimates along the slice select direction. This may be due to substantial smoothing along this direction, arising from more than half the partitions

being filled with zeroes. The largest differences between $vSNav$ and FLIRT head motion measurements were observed for subject 2 who moved continuously and slowly between volumes 61 and 65, causing the motion events to extend across more than one volume.

Differences between motion parameters estimated by $vSNav$ and FLIRT may be due to discrepancies between the image registration algorithms employed by PACE and FLIRT, as well as differences between the images being registered. While both PACE and FLIRT performed rigid-body co-registration with 6 degrees-of-freedom, PACE used a least squares cost function and FLIRT a normalized correlation cost function. Other factors that may contribute to discrepancies include (i) the lower SNR of the $vSNav$'s of which more than half the partitions are zero filled, compared to the complete volume used by FLIRT; (ii) differences in the timing of motion detection as the feedback block estimates motion based only on the 1st 24 partitions of a volume whereas FLIRT uses all the partitions of a volume; and (iii) the fact that FLIRT estimates would be affected by FOV updates applied before acquisition of the last 16 partitions of the volume.

The temporal resolution of the current technique is limited by the timing and duration of the participant's motion. Motion that occurs during accumulation of the second half of the volume's partitions (partition numbers > 24) will only be detected by the $vSNav$ of the subsequent volume acquisition, and hence only be corrected towards the end of that volume. Very rapid motion, where the subject moves and returns to his/her original position before or after accumulation of partitions for the $vSNav$, will not be detected.

2.5. Conclusion

The current study demonstrates that real-time motion detection and correction can be performed once per volume during repeated 3D-EPI volume acquisitions using volumetric self-navigators constructed from a subset of each volume's partitions. By co-registering each $vSNav$ to the one constructed during the first volume acquisition, head pose changes in the imaging FOV relative to the first volume are estimated and sent back to the sequence. The sequence adjusts the FOV accordingly and acquires the remaining partitions of that volume, as well as the first partitions of the next volume, with the corrected FOV. The proposed technique eliminates the need for extra hardware or additional pulses to track subject motion and it can be reconfigured to track motion at different times during the same volume acquisition, depending on when the subset of partitions for the $vSNav$ are accumulated. The temporal resolution is, however, limited by the number of partitions required to construct a $vSNav$ with sufficient resolution for motion estimation, as well as the time required for co-registration and

feedback. Further work is required to minimize this number to enable multiple motion corrections per volume. Implementing real-time shimming and parallel imaging in the partition direction would further improve image quality following motion correction and accelerate volume acquisitions, respectively.

2.6. Acknowledgements

Resources necessary in the project were provided by the University of Cape Town, the Cape Universities Brain Imaging Centre, and the Athinoula A. Martinos Center for Biomedical Imaging. This study was supported by the South African National Research Foundation grant 48337, National Institute of Health (NIH) grants R01HD085813, R01HD099846 and R01HD093578.

Chapter Three

3. Volumetric self-navigated ($vSNav$) 3D EPI sequence for motion-robust fMRI acquisition

3.1. Introduction

Functional magnetic resonance imaging (fMRI) is a non-invasive brain imaging technique that measures signal changes resulting from the blood oxygenation level changes that accompany neural activation. Since oxygenated hemoglobin is diamagnetic and deoxygenated hemoglobin is paramagnetic (Pauling & Coryell, 1936), localized changes in cerebral blood oxygenation levels alter the magnetic field resulting in localized signal intensity changes on T_2^* weighted images of the brain (Belliveau et al., 1991; Ogawa et al., 1992, 1990). This signal is referred to as the blood-oxygenation-level-dependent (BOLD) signal. Activation-related changes in the BOLD signal may, however, be 1% or less of the average BOLD signal (Buxton, 2009; Huettel et al., 2014), and may therefore be comparable to or smaller than signal changes resulting from other sources of noise, such as cyclic cardiac and respiratory changes, instrumental drifts, external interferences and subject motion during scanning (Birn et al., 2006; Krüger & Glover, 2001; Shmueli et al., 2007). It is therefore important to select a sequence, imaging parameters and an experimental design that maximizes the BOLD signal and minimizes the effects of noise. After fMRI data acquisition, the fMRI data are pre-processed to remove artifacts from physiological processes, device inconsistencies and subject motion (Chen & Glover, 2015; Liu, 2016), and to perform slice scan time correction and intensity normalization. The widely used fMRI analysis software packages such as AFNI (Cox, 1996), SPM (Karl J. Friston et al., 1995), BrainVoyager (Goebel et al., 2006) and FSL (Jenkinson et al., 2002) incorporate their own versions of these pre-processing steps although their performance depend on the severity of the artifacts. Since the most common source of confounding artifacts in fMRI is subject motion during scanning, selecting a sequence that minimizes effects of subject motion is critical to improving statistical power of functional analyses.

Echo planar imaging (EPI) is one of the fastest readouts for filling 2D k-space, requiring only tens of milliseconds (Stehling et al., 1991; Turner et al., 1991) – thereby minimizing effects of spin-history and intra-volume motion. However, fMRI acquires MR images repeatedly over a period of hundreds of seconds to measure the temporal evolution of the

signals in voxels making it susceptible to motion artifacts. Because of its speed, relative robustness to motion artifacts and sensitivity to BOLD contrast, 2D EPI (2D-EPI) remains the most widely used sequence for fMRI acquisitions (Chen & Glover, 2015; Norris, 2006). Due to the large flip angles (~90º) required to optimize the signal, 2D-EPI does, however, suffer from high specific absorption rates (SAR) (Collins & Wang, 2011), making it unsuitable for high spatial resolution fMRI (Bernstein et al., 2004). Acceleration techniques such as partial Fourier (PF) (Jesmanowicz et al., 1998) and partial parallel imaging (PPI) (Griswold et al., 2002) also have limited benefits in 2D-EPI, and 2D-EPI is susceptible to spin-history artifacts (Karl J. Friston et al., 1996).

Although 3D-EPI overcomes some of the shortcomings of 2D-EPI, its greater susceptibility to motion artifacts has limited its use in fMRI. 3D-EPI, for instance, does not require large flip angles (<20º) resulting in very low SAR, is free from spin-history artifacts due to slab excitation, and is suitable for both PF and PPI acceleration along the secondary phase-encoding (slice-encoding) direction (Bernstein et al., 2004; Y. Hu & Glover, 2007; Poser et al., 2010). Previously, we developed and implemented a self-navigated 3D-EPI sequence that performs prospective motion tracking and correction (PMC). Our volumetric self-navigated ($vSNav$) 3D-EPI sequence was able to successfully detect and correct head motion once during every volume acquisition (Bayih et al., 2022).

In the current work we assess the performance of our $vSNav$ 3D-EPI sequence on a finger tapping fMRI experiment, and compare its performance to that of the standard 2D-EPI sequence with PACE (**P**rospective **A**cquisition **C**orre**E**ction; (Thesen et al., 2000) prospective motion correction enabled. Performance was compared on acquisitions with no intentional head motion, non-intentional head motion (while moving legs), and intentional head motion. We also compared results from six pre-processing pipelines that only differed with respect to the full width half maximum (FWHM) of the Gaussian spatial filters that were applied (i.e., 0 mm, 3.3 mm, 6.6 mm, 8 mm, 9.9 mm, and 12 mm). The performance of the sequences was compared based on the temporal SNR (tSNR) values of voxels within the whole brain, the number of activated voxels, the mean BOLD percent signal change in the motor cortex region, and visual inspection of the activation maps.

3.2. Methods

3.2.1. Participants

Four healthy male volunteers (age 30 – 37 years) with no history of neurological disease or learning disability were scanned on a 3T Skyra (Siemens, Erlangen, Germany) located at the Cape Universities Body Imaging Center (CUBIC) in Cape Town, South Africa, according to protocols that had been approved by the Faculty of Health Sciences Human Research Ethics Committee of the University of Cape Town. Written informed consent was obtained from each volunteer.

3.2.2. fMRI task

E-Prime v2.0 was used to present instructions during a block design finger-tapping fMRI experiment. Participants received visual cues to tap either their right- or left-hand fingers for 20 s (Tap_R, Tap_L). Tapping blocks were interleaved with 20 s rest blocks during which a crosshair was displayed ('+'). During the tapping blocks, participants had been instructed to continuously and consecutively tap their index, middle, ring and pinky fingers against the thumb of that hand. Each experiment comprised an initial rest period during which the first 4 volumes were acquired, followed by 8 finger-tapping blocks (4 left, 4 right) interleaved with 8 rest blocks. The order of left- and right-hand finger-tapping blocks were randomized. In two of the participants, randomizations were generated by E-Prime; due to a technical error the order of left- and right-hand blocks were not logged in these experiments. In the remaining two participants, the order of left- and right-hand tapping blocks were set by the experimenter. Six volumes were acquired during each of the tapping and rest blocks. Therefore, a total of 100 volumes were acquired during each 2D-EPI and 3D-EPI acquisition. The first 4 volumes were discarded from our analyses to eliminate T1 saturation effects.

Instructions to perform intentional non-head and head motions during the acquisitions were similarly visually displayed. Instructions to move were displayed for 20 s and were always given during the rest blocks. Participants had been instructed to always move once after receiving a motion cue and to remain in the new position until they received another cue to move. Non-intentional head motions were induced when participants moved their legs. Participants had been instructed to either open or close their legs once (i.e. to open their legs if closed, and close them if open) when they saw the cue '||+/\'. Intentional head motion involved nodding or sideways rotations of the head. The cues 'Nod+' and 'Side+' instructed participants to either nod their head (chin down) or rotate it to the right or left. For rotations, three dots had

been drawn on the inside of the coil – one in the center and one about 8 cm to either side. Participants rotated their head to look at either the right or left dot when they received the 'Side+' cue. Participants had been instructed to move their head once after receiving a cue and remain in the new position until receiving the 'Center+' cue instructing them to return their head to its original position (Figure 3-1). All subjects had learned the instructions and practiced the tasks before scanning. In all scanning sessions, head cushions and inflatable pads were used to improve subjects' comfort and to minimize undesired bulk head motion.

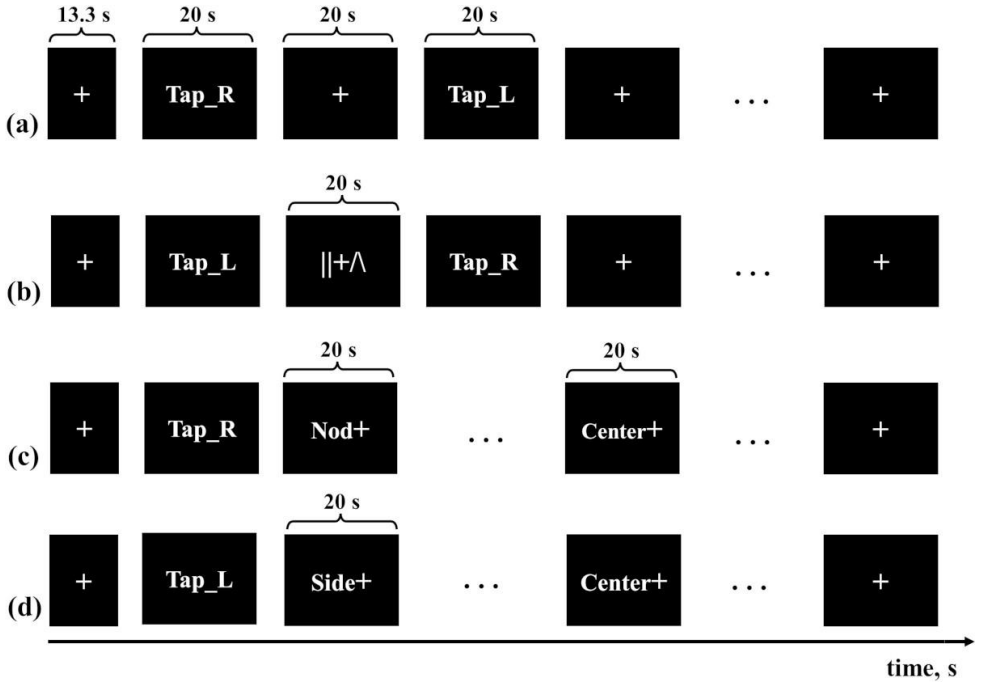

Figure 3-1 Block design of the finger-tapping experiment. The illustration shows the visual cues presented to participants during acquisitions with (a) no motion, (b) leg motion, and (c) pitch and (d) yaw head motions.

3.2.3. fMRI acquisition parameters

The acquisitions were performed using a 20-channel head/neck coil with imaging parameters: TE 30 ms, FOV 210×210 mm^2, acquisition matrix 64×64, voxel size $3.3 \times 3.3 \times 3.1$ mm^3, fat saturation ON and 100 volumes. For 2D-EPI, 52 interleaved slices were acquired per volume, with volume TR (TRvol) 3400 ms, flip-angle 90^0 and bandwidth 1736 Hz/px. For 3D-EPI we used our $vSNav$ 3D-EPI (Bayih et al., 2022) sequence with 52 partitions per volume acquired using a center-out acquisition scheme, TRvol 3328 ms, flip-angle 16^0 and bandwidth 2298 Hz/px. All acquisitions were in sagittal orientation with slice select from right to left and phase encoding from inferior to superior.

In each participant, motion corrected (MoCo) 2D-EPI and 3D-EPI data were acquired for a subset of three different motion protocols (no intentional motion (NoMo); leg motion; head motion involving sideways rotations); the order of 2D-EPI and 3D-EPI acquisitions were randomized across participants. In MoCo 2D-EPI acquisitions, prospective motion correction was performed using the Siemens PACE function, and in MoCo 3D-EPI using our volumetric self-navigators.

One participant (participant 4) was re-scanned on a separate occasion to compare the effects of pitch (nodding) and yaw (rotation) motions during our finger-tapping experiment in 3D-EPI acquisitions without (NoCo) and with (MoCo) prospective motion correction enabled.

3.2.4. Pre-processing

The first 4 volumes were removed from both the 2D-EPI and 3D-EPI fMRI data to eliminate T1 saturation effects. Identical pre-processing steps were applied to the 2D-EPI and 3D-EPI data except for slice scan time correction, which was adjusted to account for the different acquisition trajectories of slices and partitions in the 2D and 3D sequences, respectively. De-spiking, motion correction and 3D-EPI slice scan time correction, which required a text file specifying each partition's acquisition time in the center-out acquisition scheme, were performed using AFNI (Analysis of Functional NeuroImages) (Cox, 1996; Cox & Hyde, 1997), while non-brain tissue removal, intensity normalization, high-pass temporal filtering with cut-off 0.025 Hz, spatial filtering, and 2D-EPI slice scan time correction were performed with FSL (FMRIB Software Library v6.0) (Jenkinson et al., 2012; Smith et al., 2004; Woolrich et al., 2009). During motion correction, linear Fourier interpolation was used to maintain the signal quality and to avoid spatial smoothing. Since spatial smoothing forms part of most 2D-EPI fMRI processing pipelines, and may perform differently for 3D-EPI data, it was necessary to compare the effects of spatial smoothing on 2D- and 3D-EPI data. To this end, we repeated the pre-processing of each 2D- and 3D-EPI data set applying 5 different 2D or 3D, respectively, Gaussian spatial filters, namely FWHM 3.3 mm (in-plane resolution), 6.6 mm (2 x in-plane resolution), 8 mm, 9.9 mm (3 x in-plane resolution), and 12 mm. The filter sizes were chosen based on widely recommended sizes for first- and multi-level fMRI analyses (Alahmadi, 2021; Mikl et al., 2008). Each participant's fMRI data were co-registered to his 1.0 mm^3 structural T1 weighted images and normalized to the MNI152_T1_2mm_brain standard space using a linear transform calculated on the anatomical images.

3.2.5. Statistical analysis of fMRI data

In this work, first-level statistical analyses were performed using FEAT (FMRI Expert Analysis Tool, Version 6.0) (Woolrich et al., 2001, 2004). The block design finger-tapping experiment was modeled by a rectangular function convolved with a double-gamma hemodynamic response function (HRF) and its temporal derivative (K. J. Friston et al., 1998). The standard and extended residual motion parameters estimated by MCFLIRT were included in the model to minimize the confounding effects of residual motion artifacts on explanatory variables (EVs). The right- and left-hand finger-tapping conditions were modeled separately for the two participants in whom the order was known, but as a single 'finger tapping' predictor for the other two participants. In all models resting blocks were used as baseline. A temporal high-pass filter of 0.025 Hz, Z threshold ≥ 2.3 and cluster significance threshold of $p < 0.05$ were selected for all analyses.

To assess the quality of the BOLD data, we computed the voxel-wise temporal signal-to-noise ratios (tSNR) for each preprocessed data set. For each voxel, tSNR was defined as the mean of the signal time course divided by the standard deviation of the residuals after model fitting. The voxel-wise percent BOLD signal changes during finger tapping were determined from the parameter estimates using Featquery. We computed the mean and standard deviation of the percent BOLD signal changes in the motor cortex by averaging the voxel-wise %BOLD signal changes across all voxels with Z ≥ 2.3 and located in the left or right motor cortex. 'Activated' voxels within the left or right motor cortices were identified using the intersections of a mask comprising the primary motor cortices, the Z-statistic maps, and binarized rectangular volumes positioned over either the left or right motor cortex regions. The mask of the primary motor cortices was obtained by eroding the relevant regions on the Juelich Histological Atlas by 10%. For the different acquisition protocols, we compared the mean and standard deviation of the %BOLD signal changes within the motor cortices, as well as the number of activated voxels. Finally, activation maps were generated in MNI152_T1_1mm_brain standard coordinates.

3.3. Results

3.3.1. Motion performed

As shown for a single participant in Figure 3-2, the motion estimates relative to the 1st volume obtained with FLIRT retrospective motion correction (RMC) were similar to the prospective motion estimates output during the MoCo 2D-EPI acquisition by PACE (Figure 3-2 a) and during the MoCo 3D-EPI acquisition by the $vSNav$'s (Figure 3-2 b). The non-

intentional head motion (of the order 1-3 mm translation and 0.5 degrees rotation) shown in Figure 3-2 resulted when the participant opened and closed his legs as instructed around the acquisition of the 11th and 58th volumes of the finger-tapping experiment. Figure 3-3 similarly shows in acquisitions where the participant intentionally rotated his head by 3 to 6 degrees around the left-right axis (i.e. nodding motion) that the motion estimates obtained with FLIRT retrospectively were similar to those obtained prospectively from either PACE during 2D-EPI or from the $vSNav$'s during 3D-EPI.

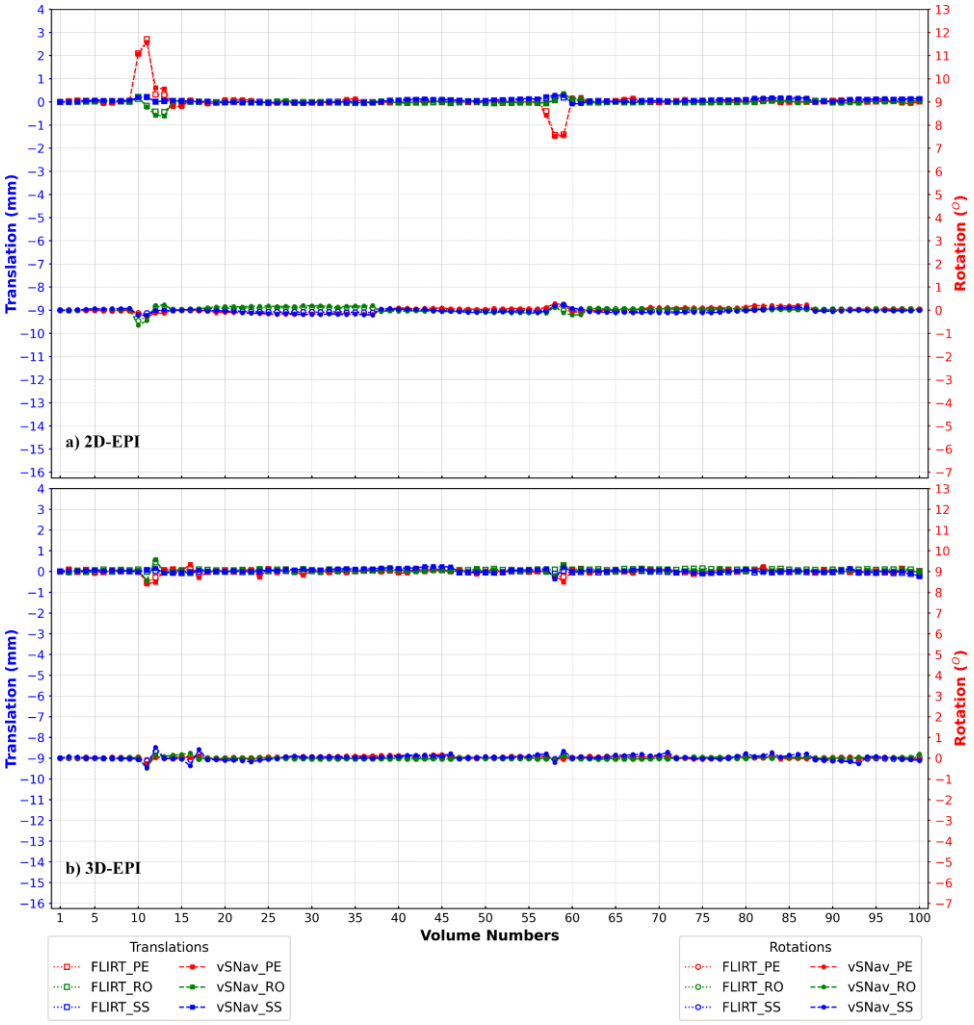

Figure 3-2 Comparison of translation (left scale) & rotation (right scale) estimates relative to the 1st volume obtained for motion corrected (MoCo) (a) 2D-EPI and (b) 3D-EPI acquisitions with similar motion protocols in the same participant. In both plots, retrospective motion estimates were computed using FLIRT. Prospective motion estimates were computed using online PACE. In 2D-EPI, PACE uses the entire volume to estimate motion parameters; in 3D-EPI, PACE uses the volumetric self-navigators (3D-EPI). Non-intentional head motions were induced when participant 4 opened and closed his legs at discrete times during the finger-tapping experiment. PE denotes the phase-encoding direction, RO the readout direction, and SS the slice-select direction. Images were acquired in the sagittal orientation with slice-select from right to left and phase encoding from inferior to superior.

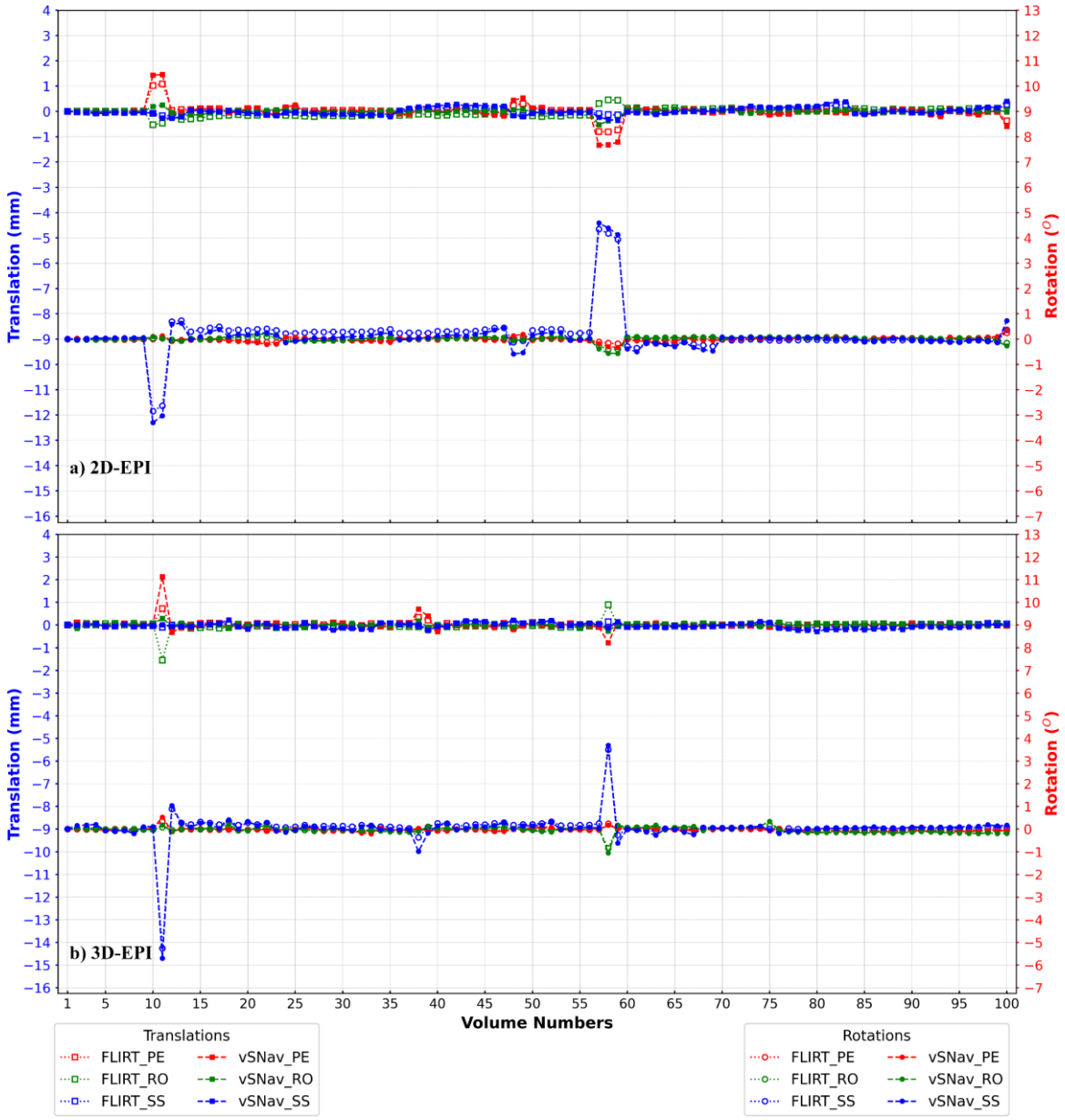

Figure 3-3 Comparison of translation (left scale) & rotation (right scale) estimates relative to the 1st volume obtained for motion corrected (MoCo) (a) 2D-EPI and (b) 3D-EPI acquisitions with similar motion protocols in the same participant. In both plots, retrospective motion estimates were computed using FLIRT and prospective motion estimates using online PACE. In 2D-EPI, PACE uses the entire volume to estimate motion parameters; in 3D-EPI, PACE uses the volumetric self-navigators (3D-EPI). In these acquisitions, intentional head motions were induced when participant 4 moved his chin up or down at discrete times during the finger-tapping experiment. PE denotes the phase-encoding direction, RO the readout direction, and SS the slice-select direction. Images were acquired in the sagittal orientation with slice-select from right to left and phase encoding from inferior to superior.

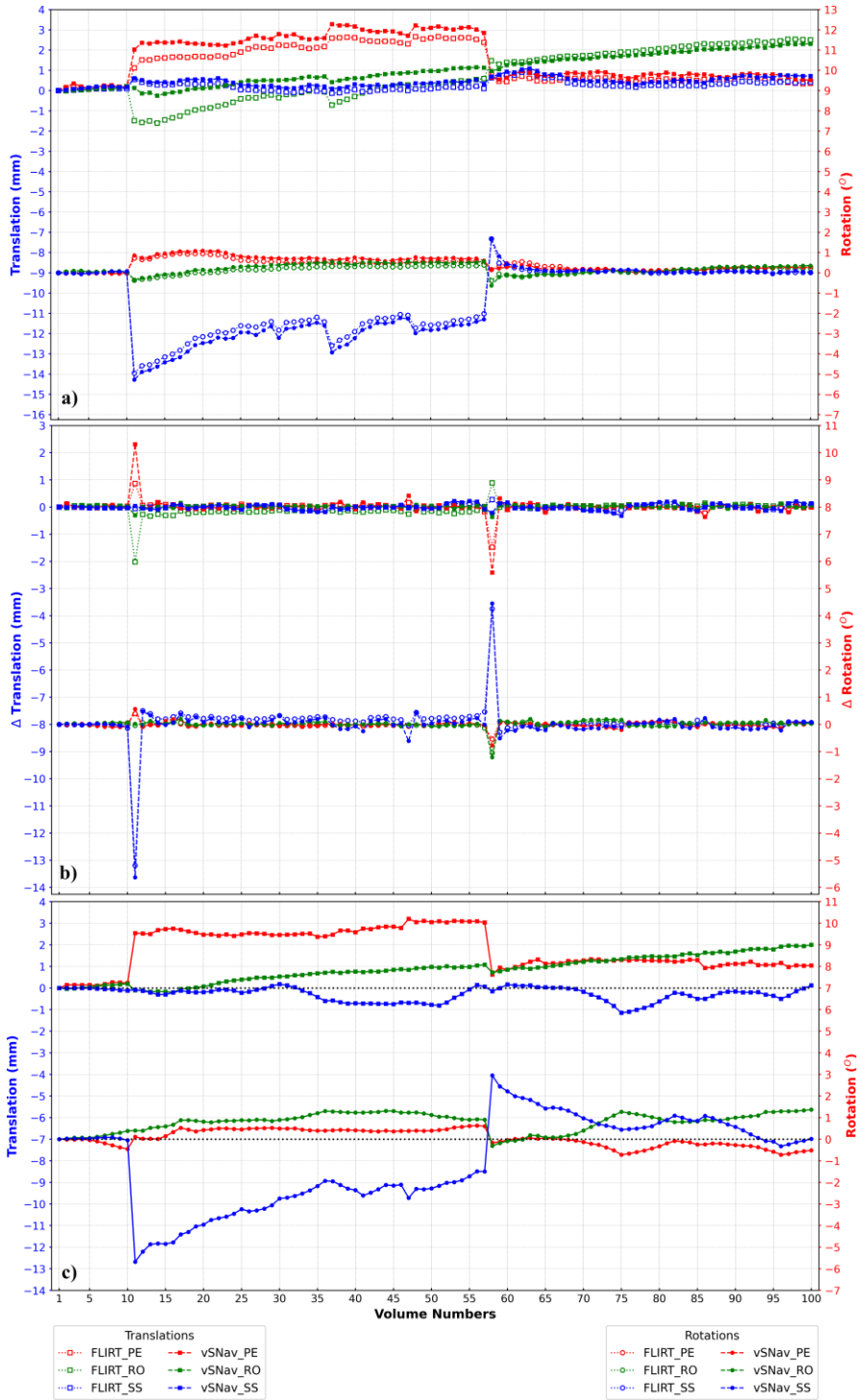

Figure 3-4 Translation (left scale) & rotation (right scale) estimates relative to the 1st volume obtained using FLIRT and the volumetric self-navigators (vSNav's) for 3D-EPI acquisitions with (a) no prospective motion correction applied (NoCo), and (b & c) with prospective motion correction enabled (MoCo). Due to prospective motion correction, motion estimates in (b) show changes in position between successive volumes. To facilitate comparison with motion estimates in (a), the motion parameters in (b) were integrated over time to generate position changes relative to the 1st volume for the MoCo acquisition (shown in (c)). Both these acquisitions were in participant 4 and performing the same motion protocol, which involved moving his chin up or down (pitch) at discrete times during the acquisition. PE denotes the phase-encoding direction, RO the readout direction, and SS the slice-select direction. Images were acquired in the sagittal orientation with slice-select from right to left and phase encoding from inferior to superior.

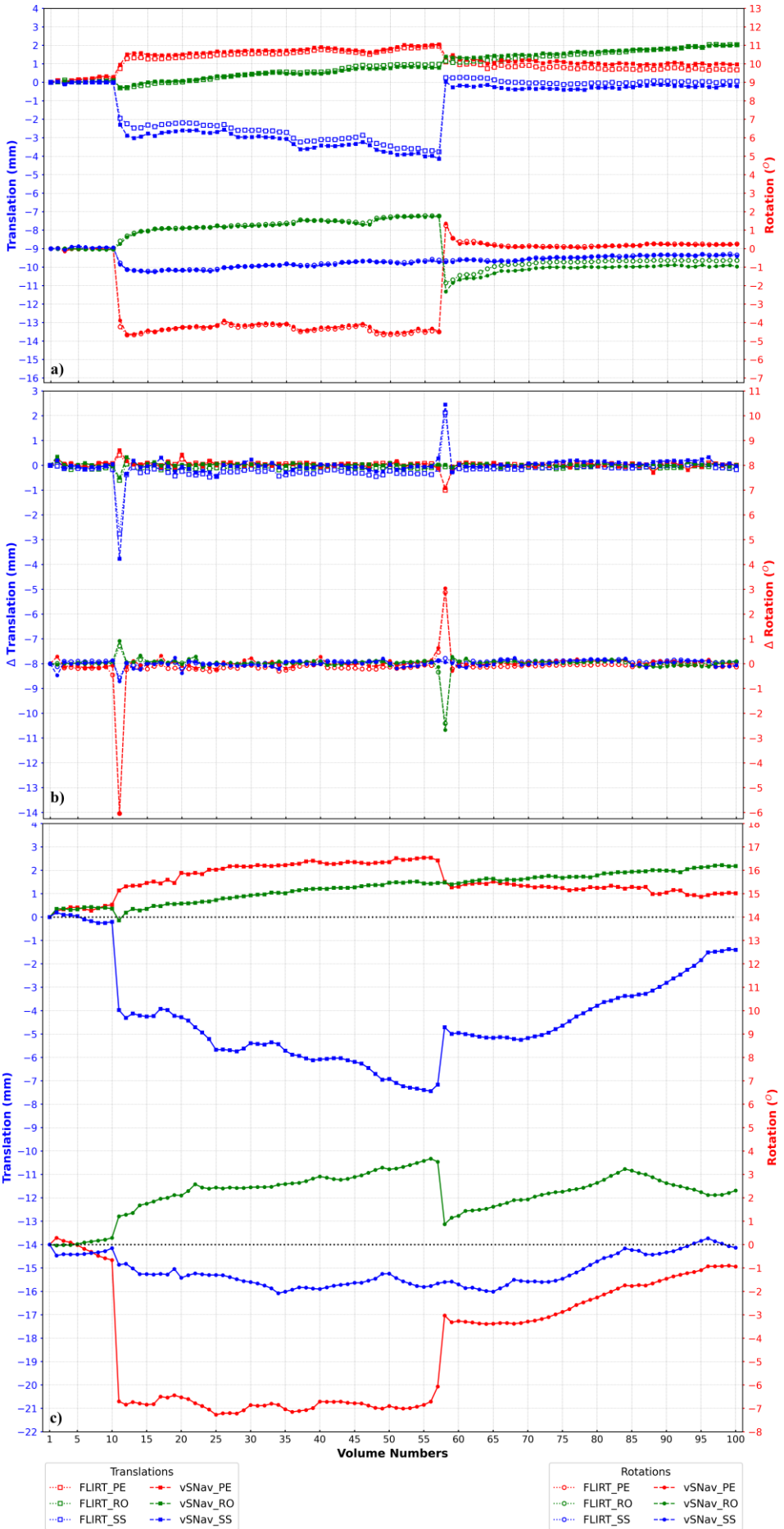
a)
b)
c)
Translation (mm)
Rotation (°)
Δ Translation (mm)
Δ Rotation (°)
Volume Numbers
Translations
FLIRT_PE
FLIRT_RO
FLIRT_SS
vSNav_PE
vSNav_RO
vSNav_SS
Rotations
FLIRT_PE
FLIRT_RO
FLIRT_SS
vSNav_PE
vSNav_RO
vSNav_SS

Figure 3-5 Translation (left scale) & rotation (right scale) estimates relative to the 1st volume obtained using FLIRT and the volumetric self-navigators (vSNav's) for 3D-EPI acquisitions with (a) no prospective motion correction applied (NoCo), and (b & c) with prospective motion correction enabled (MoCo). Due to prospective motion correction, motion estimates in (b) show changes in position between successive volumes. To facilitate comparison with motion estimates in (a), the motion parameters in (b) were integrated over time to generate position changes relative to the 1st volume for the MoCo acquisition (shown in (c)). Both these acquisitions were in participant 4 and for the same motion protocol, which involved rotating his head away from the centre and back to the centre (yaw) at discrete times during the acquisition. PE denotes the phase-encoding direction, RO the readout direction, and SS the slice-select direction. Images were acquired in the sagittal orientation with slice-select from right to left and phase encoding from inferior to superior.

Figure 3-4 and Figure 3-5 show for a single participant that the motion estimates obtained retrospectively with FLIRT and prospectively with the $vSNav$'s were similar both in the absence (NoCo) and presence (MoCo) of prospective motion correction. In both figures, due to prospective motion correction, the plots in (b) only show changes in position (i.e. motion) between successive volumes. To facilitate comparison with motion estimates in (a), the motion parameters in (b) were integrated over time to generate position changes relative to the 1st volume for the MoCo acquisitions (shown in (c)). In Figure 3-4, pitch head motions were induced when the participant moved his chin up or down by 5 to 6 degrees around the acquisition of volumes 11 and 58, and in Figure 3-5 yaw head motions were induced when the participant rotated his head by similar amounts away from and back to the center at roughly the same times during the acquisition.

3.3.2. Data quality (tSNR)

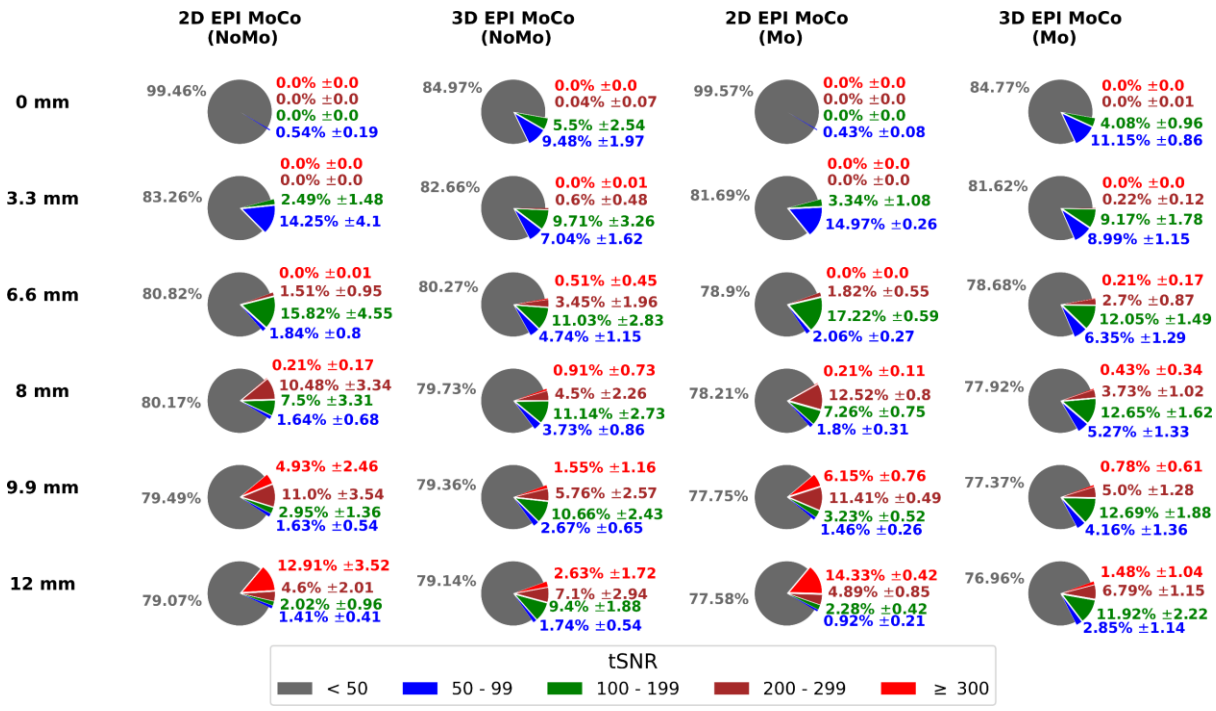

Figure 3-6 Summary of the percentage of brain voxels with tSNR values within the given ranges (less than 50, 50 to 99, 100 to 199, 200 to 299, and 300 or greater) for motion corrected (MoCo) 2D-EPI and 3D-EPI acquisitions both in the absence (NoMo) and presence (Mo) of motion. The tSNR values were computed from the pre-processed data of each acquisition, and the % voxels within each range averaged across participants and acquisitions. Results are shown following pre-processing with 0 mm, 3.3 mm, 6.6 mm, 8 mm, 9.9 mm, and 12 mm FWHM Gaussian spatial filters.

Figure 3-6 shows a summary of the percentage of brain voxels with tSNR values within the given ranges, i.e. < 50, 50 to 99, 100 to 199, 200 to 299, or ≥300, for 2D- and 3D-EPI acquisitions, respectively, and both in the absence (NoMo) and presence (Mo) of intentional motion. Prospective motion correction (MoCo) was active for both the 2D- and 3D-EPI acquisitions. Each 2D- and 3D-EPI MoCo acquisition was pre-processed using 6 different spatial filters, namely 0.0 mm, 3.3 mm, 6.6 mm, 8 mm, 9.9 mm, and 12 mm. For each filter, the percentage of voxels within each tSNR range were averaged across participants and acquisitions. It is evident in the unsmoothed data that the inherent tSNR of 3D-EPI is higher than for 2D-EPI. Surprisingly, for both the 2D- and 3D-EPI acquisitions, the distribution of tSNR values was similar for acquisitions without and with intentional motion. However, compared to 3D data for which there were limited increases in tSNR following smoothing with filters with FWHM >6.6 mm, 2D data showed a substantial impact of increased smoothing. Following smoothing of 2D data with filters of FWHM 9.9 and 12 mm, >15% of voxels

demonstrated tSNR values ≥200, and <5% of voxels had tSNR values in the range 50 to 199, compared to <2% and 17 to 19%, respectively, after smoothing with a 6.6 mm Gaussian filter.

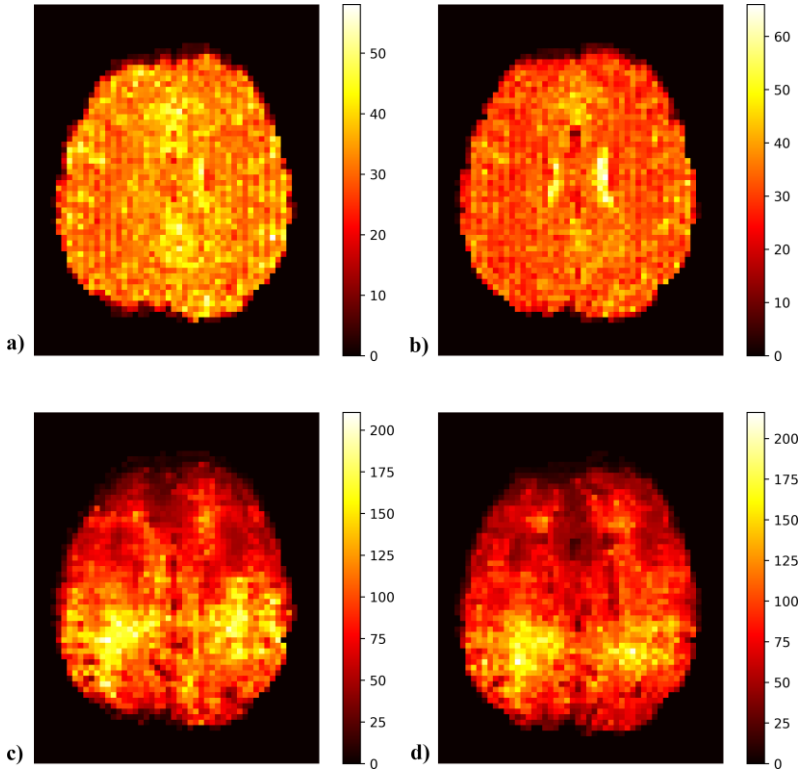

Figure 3-7 Heat maps of tSNR values in the 43rd axial slice of participant 4. The heat maps in the top row show unsmoothed tSNR values for 2D-EPI data acquired: a) without head motion, and b) with head motion. The heat maps in the bottom row show unsmoothed tSNR values for 3D-EPI data acquired: c) without head motion, and d) with head motion. Images were acquired in the sagittal orientation with slice-select from right to left and phase encoding from inferior to superior.

Figure 3-7 displays heat maps of tSNR values (before spatial smoothing) for a single axial slice (the 43rd slice) for (top row) 2D-EPI and (bottom row) 3D-EPI acquisitions in participant 4. Figure 3-7a) and c) showcase heatmaps of 2D- and 3D-EPI data acquired without head motion, while Figure 3-7b) and d) display heatmaps of 2D and 3D EPI data acquired with head motion. Notably, the higher tSNR values of 3D-EPI data appear to be localized in activated brain regions.

3.3.3. FMRI analyses

Mean percent BOLD signal change & number of activated voxels

Table 3-1 and Table 3-2 compare in each participant and for different motion protocols (NoMo, leg motion, head motion involving sideways rotations) the number of voxels in the motor cortex activated during finger tapping, and their % BOLD signal changes, between the

2D-EPI and 3D-EPI acquisitions. Table 3-1 presents results from data that had not been spatially smoothed, and Table 3-2 from data that had been spatially smoothed with a 6.6 mm Gaussian filter.

Table 3-1 Comparison between 2D- and 3D-EPI acquisitions for each participant and each motion protocol of the number of voxels in the motor cortex showing activation during finger tapping, and their mean percent BOLD signal changes. These results were obtained using the unsmoothed fMRI data. The percentage BOLD signal changes between the 2D- and 3D-EPI acquisitions were compared using a two-tailed two-sample t-test.

Participant	Motion protocol	Sequence (all with MoCo enabled)	Number of active voxels	Mean % BOLD signal change ± standard deviation	*t*	*p*
1	NoMo	2D-EPI	133	7.3 ± 7.3	6.3	<0.001
		3D-EPI	215	2.4 ± 6.3		
	Leg Mo	2D-EPI	145	6.3 ± 6.1	4.6	<0.001
		3D-EPI	62	1.8 ± 6.5		
2	NoMo	2D-EPI	130	5.9 ± 3.9	4.6	<0.001
		3D-EPI	354	3.9 ± 5.4		
3	NoMo	2D-EPI	103	4.3 ± 3.4	6.9	<0.001
		3D-EPI	613	1.9 ± 6.2		
4	NoMo	2D-EPI	171	7.5 ± 5.9	8.8	<0.001
		3D-EPI	241	3.3 ± 2.7		
	Leg Mo	2D-EPI	236	7.1 ± 4.4	5.5	<0.001
		3D-EPI	279	4.3 ± 7.2		
	NoMo	2D-EPI	69	6.6 ± 4.2	6.8	<0.001
		3D-EPI	181	3.0 ± 2.6		
	Head Mo	2D-EPI	72	5.9 ± 4.0	5.3	<0.001
		3D-EPI	258	3.2 ± 3.1		

Overall, except for leg motion in participant 1, unsmoothed 2D-EPI data yielded fewer activated voxels but larger % BOLD signal changes than 3D-EPI data (Table 3-1). In contrast, the pattern was much more variable after spatial smoothing (Table 3-2). For example, for acquisitions with no intentional motion, 3D-EPI yielded larger % BOLD signal changes than 2D-EPI in participants 1 and 2, similar % BOLD signal changes in participant 3, and smaller % BOLD signal changes in participant 4. In acquisitions with leg motion, 3D-EPI yielded similar % BOLD signal changes as 2D-EPI in participant 1, but smaller % BOLD signal changes in participant 4. For the acquisitions with head motion in participant 4, 2D- and 3D-EPI yielded similar % BOLD signal changes.

Table 3-2 Comparison between 2D- and 3D-EPI acquisitions for each participant and each motion protocol of the number of voxels in the motor cortex showing activation during finger tapping, and their mean percent BOLD signal changes. These results were obtained from fMRI data that had been spatially smoothed with a 6.6 mm Gaussian filter. The percentage BOLD signal changes between the 2D- and 3D-EPI acquisitions were compared using a two-tailed two-sample t-test.

Participant	Motion protocol	Sequence (all with MoCo enabled)	Number of active voxels	Mean % BOLD signal change ± standard deviation	*t*	*p*
1	NoMo	2D-EPI	494	1.8 ± 1.4	4.0	<0.001
		3D-EPI	378	2.4 ± 2.7		
	Leg Mo	2D-EPI	565	1.7 ± 1.3	1.6	0.18
		3D-EPI	210	1.9 ± 2.0		
2	NoMo	2D-EPI	431	1.7 ± 1.0	4.6	<0.001
		3D-EPI	557	2.0 ± 1.1		
3	NoMo	2D-EPI	470	1.0 ± 0.5	1.6	1.0
		3D-EPI	1025	1.0 ± 0.7		
4	NoMo	2D-EPI	547	2.1 ± 1.4	5.0	<0.001
		3D-EPI	407	1.7 ± 1.0		
	Leg Mo	2D-EPI	754	2.4 ± 1.6	4.8	<0.001
		3D-EPI	517	2.0 ± 1.9		
	NoMo	2D-EPI	222	1.9 ± 1.0	5.8	<0.001
		3D-EPI	301	1.4 ± 0.9		
	Head Mo	2D-EPI	270	1.6 ± 0.8	0.9	0.14
		3D-EPI	438	1.7 ± 1.0		

Figure 3-8 shows in a single participant how the mean % BOLD signal change in activated voxels decreases and the number of activated voxels in the motor cortex increases with increasing spatial smoothing. Notably, the effects are similar for 2D- and 3D-EPI data and for different motion protocols, except that the smoothing-related increase in the number of activated voxels for 2D-EPI acquisitions during which leg motion occurred is substantially greater than for either of the other motion protocols. This same increase is not evident in the 3D-EPI results. Moreover, the decrease in the % BOLD signal change following smoothing with a 3.3 mm spatial filter is larger for 2D-EPI than 3D-EPI data.

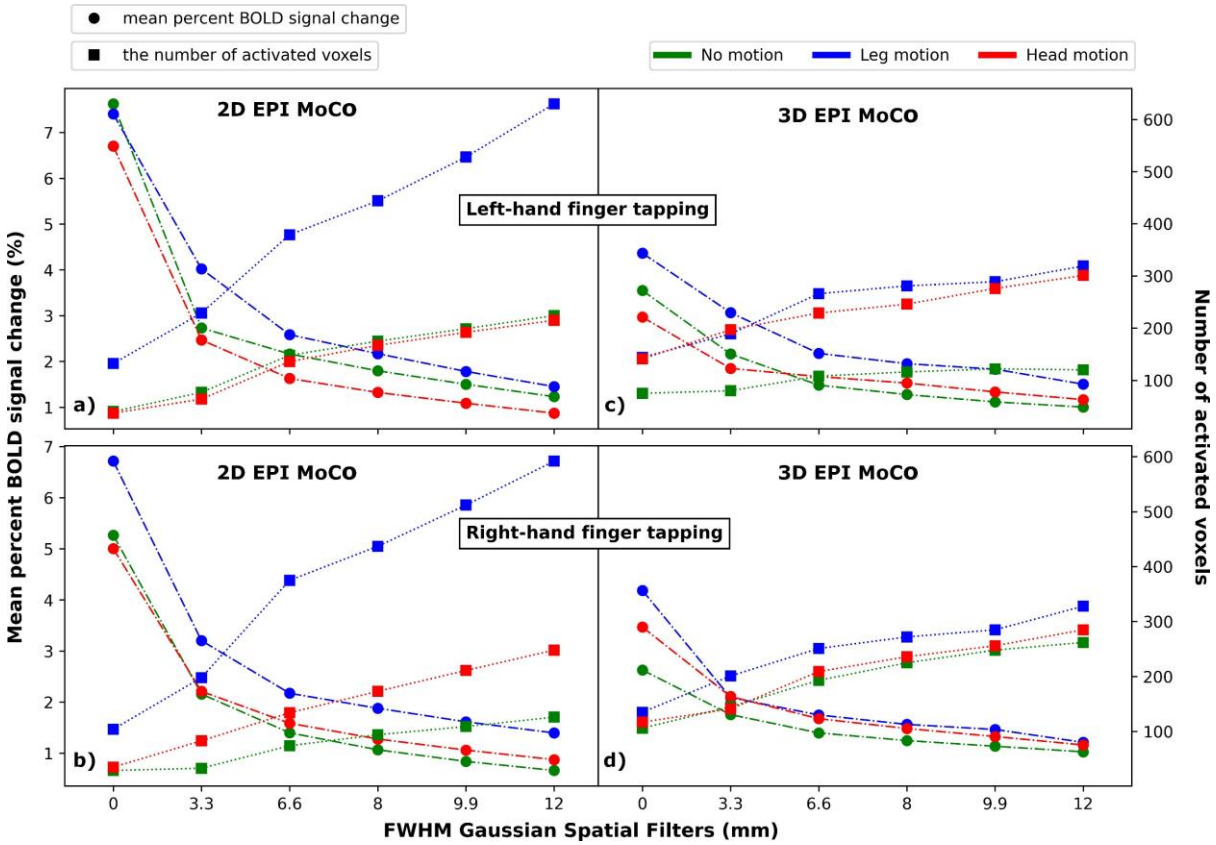

Figure 3-8 Comparison in participant 4 of the effects of spatial smoothing on the (left scale) mean percent BOLD signal change in motor cortex during finger tapping, and (right scale) the number of voxels activated, in data acquired using either motion corrected (MoCo) (left) 2D- or (right) 3D-EPI. Results are presented separately for (top) left- and (bottom) right-hand finger tapping and are compared for different motion protocols (none, leg motion, head motion). The results were based on statistical analyses of data that had been spatially smoothed using Gaussian filters with FWHM 0 mm, 3.3 mm, 6.6 mm, 8 mm, 9.9 mm, or 12 mm, respectively, Z threshold ≥ 2.3 and cluster significance threshold $p < 0.05$.

Figure 3-9 compares how spatial smoothing affects the mean % BOLD signal change and the number of activated voxels in the motor cortex during finger tapping in 3D-EPI acquisitions without (NoCo) and with (MoCo) prospective motion correction for pitch and yaw motions. While the effects of increasing smoothing on the % BOLD signal change were similar in NoCo and MoCo acquisitions, and for pitch and yaw motion, the effects on the number of activated voxels in NoCo acquisitions were more variable than in MoCo acquisitions, especially on the left-hand finger tapping results.

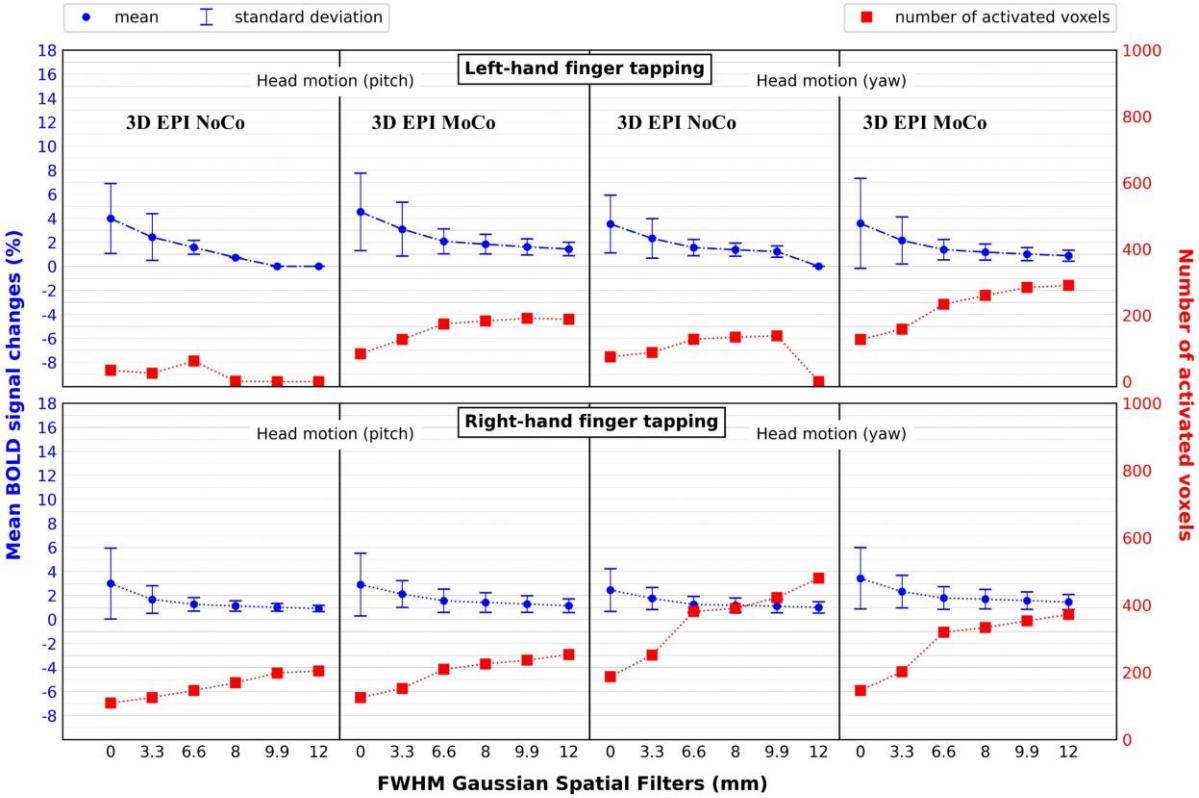

Figure 3-9 Comparison in participant 4 of the effects of spatial smoothing on the (left scale) mean percent BOLD signal change (and standard deviation) in motor cortex during finger tapping, and (right scale) the number of activated voxels, in data acquired using 3D-EPI either without (NoCo) or with (MoCo) prospective motion correction applied. Results are presented separately for (top) left- and (bottom) right-hand finger tapping and are compared for pitch and yaw motions. The results were based on statistical analyses of data that had been spatially smoothed using Gaussian filters with FWHM 0 mm, 3.3 mm, 6.6 mm, 8 mm, 9.9 mm, or 12 mm, respectively, Z threshold ≥ 2.3 and cluster significance threshold $p < 0.05$.

Activation maps

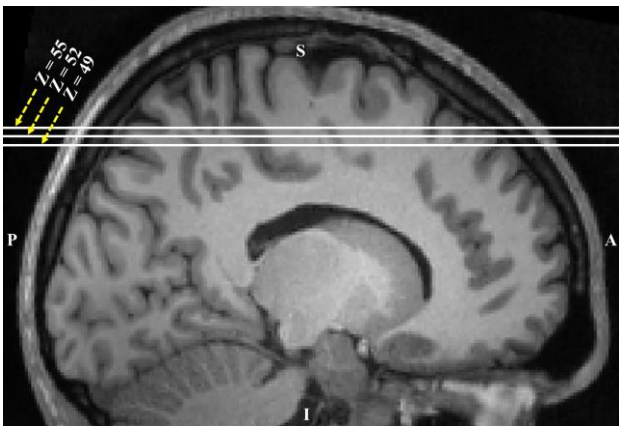

Figure 3-10 The location of the 49th, 52nd, and 55th slices in MNI152 standard space are shown on the high-resolution (1 mm³) T1 images of subject 4.

Figure 3-10 shows the location of the 49th, 52nd and 55th slices in MNI152_T1_1mm standard space on the high resolution (1 mm^3) T1 images of participant 4.

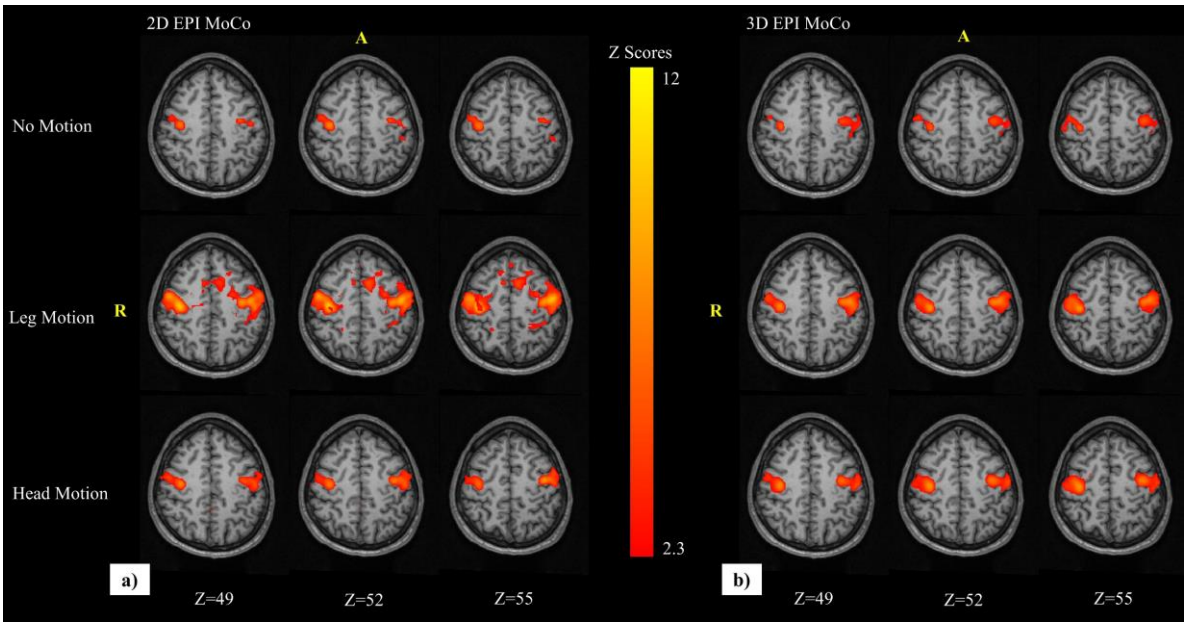

Figure 3-11 Brain regions showing increased activation ($Z \geq 2.3$ and $p < 0.05$) during finger tapping in participant 4. Activation maps were generated from 6.6 mm spatially smoothed (a) MoCo 2D-EPI and (b) MoCo 3D-EPI acquisitions with no motion (top row), leg motion (middle row) or head motion (bottom row).

In Figure 3-11we compare activation maps during finger tapping (left and right combined) in this participant in these slices for MoCo 2D and 3D acquisitions and for different motion protocols. In Figure 3-12, we compare activation maps for NoCo and MoCo 3D-EPI acquisitions during which participant 4 performed pitch or yaw motions. Notably, the 2D data in both Figure 3-11 and Figure 3-12 demonstrate more distributed activations, while activations from 3D data, except for acquisitions with pitch motion, are largely localized within the left and right motor regions.

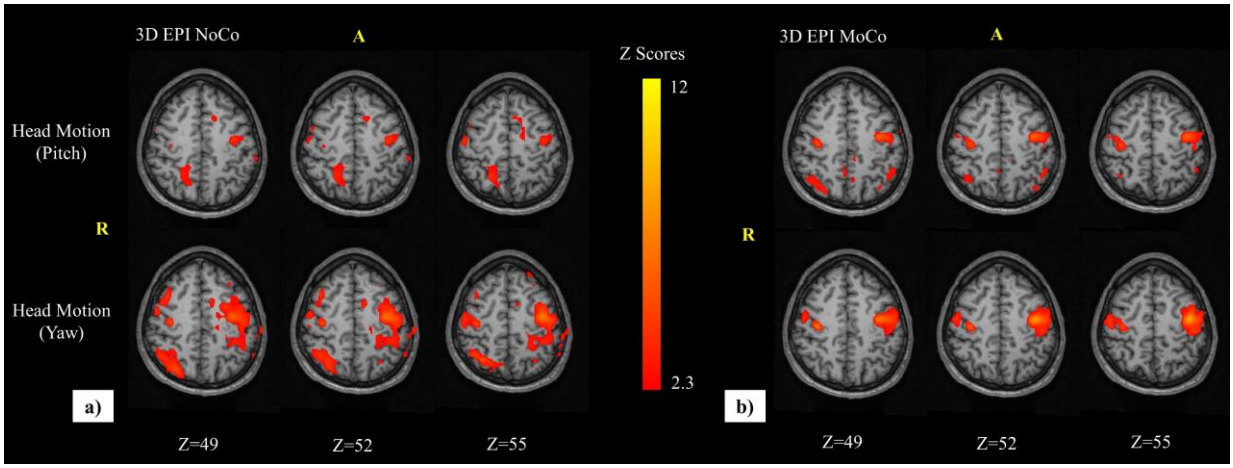

Figure 3-12 Brain regions showing increased activation ($Z \geq 2.3$ and $p<0.05$) during finger tapping in participant 4. Activation maps were generated from 6.6 mm spatially smoothed (a) NoCo and (b) MoCo 3D-EPI acquisitions with pitch (top) or yaw (bottom) head motions.

3.4. Discussion

This work demonstrates that both in the absence and presence of head motion, our prospectively motion corrected $vSNav$ 3D-EPI sequence (Bayih et al., 2022) is able to acquire task-related BOLD signal changes with comparable or better quality than 2D-EPI with PACE prospective motion correction.

Overall, prospective motion estimates (from both PACE and our $vSNav$'s) were in good agreement with those obtained using retrospective FLIRT motion correction, and both 2D- and 3D-EPI acquisitions demonstrated effective motion correction. Notably, in both participants who were asked to move their legs during the acquisitions, larger head motions were recorded in the 2D- than 3D-EPI acquisitions (Figure 3-2). The difference in the magnitude of these unintentional head motions may be related to the timing of the motion computation and FOV update by PACE compared to that of the $vSNav$ sequence. PACE only updates the FOV of the 2D-EPI acquisition before the start of the next volume acquisition. This means that whenever there is a change in head pose, PACE detects it after TRvol (Thesen et al., 2000), which was 3400 ms in our case. This results in a relatively long time during which substantial motion may occur before the FOV is updated. In contrast, the $vSNav$ 3D-EPI sequence has been configured to update the FOV as soon as the motion estimates become available, which is after roughly 2304 ms (36 partitions) in our implementation (Bayih et al., 2022). As such, the last 16 partitions of the current volume are acquired with the updated FOV. The trapezoidal and triangular shapes evident in the motion estimates of the 2D-EPI acquisitions in Figure 3-2 and

Figure 3-3 demonstrate this delayed motion correction with PACE compared to the $vSNav$ 3D-EPI.

In the NoCo 3D-EPI acquisitions shown in Figure 3-4 and Figure 3-5, we observed small (<1.5 mm) differences, especially in translation estimates, between FLIRT and the $vSNav$'s. These may be due to continued motion after acquisition of the partitions used to construct the $vSNav$ image, or after the FOV update. In such cases, the $vSNav$'s would only detect part of the motion occurring during the volume acquisition, compared to FLIRT which bases its motion estimate on all 52 partitions. Since motion parameters were not sent to the 3D-EPI to perform motion correction in these NoCo acquisitions, these phase and frequency discrepancies persist until the head returns close to its original position within the FOV. Notably, the $vSNav$ and FLIRT estimates were within sub-millimeter agreement after the head returned back to its original position, even when the discrepancy in the readout direction was greater than the translational component of the pitch head motion (see Figure 3-4 a).

It has been reported previously that 3D high spatial resolution acquisitions yield higher tSNR MR signals than 2D acquisitions (Bernstein et al., 2004; Y. Hu & Glover, 2007). Here we compared the tSNR of 2D- and 3D-EPI at intermediate spatial resolutions (3.3x3.3x3.1 mm^3) (Scouten et al., 2006). The voxel wise tSNR values of spatially unsmoothed data reflect the inherent MR signal quality of each voxel. We further examined the effects of different amounts of spatial smoothing on tSNR by applying 3.3 mm, 6.6 mm, 8 mm, 9.9 mm, and 12 mm FWHM Gaussian filters to identically pre-processed data, whereafter the same first-level statistical analyses were performed.

As seen in Figure 3-6 and Figure 3-7, the inherent MR signal quality of MoCo 3D-EPI was superior to that of MoCo 2D-EPI, both in the absence and presence of motion. The superior inherent MR signal quality of MoCo 3D-EPI is consistent with the higher SNR expected for a 3D volume comprising 52 partitions and TR/T1 = 0.06, using T1=1330 ms for grey matter (Bernstein et al., 2004). As expected, spatial filtering enhanced the MR signal quality (tSNR) of both the 2D and 3D data. Although the total number of brain voxels with tSNR > 50 appeared to plateau for spatial filters greater than 6.6 mm (twice the size of the voxel) for both 2D and 3D data, more tSNR increases were observed in the 2D than 3D data. For instance, the increase in the number of brain voxels with tSNR ≥ 300 after 12 mm spatial filtering was 13 to 14% for 2D and 1.5 to 3% for 3D. Irrespective of the inherent MR signal quality of 3D brain voxels, the number of 2D brain voxels enhanced by a pre-processing pipeline that included spatial

filtering, were more than triple the number of 3D brain voxels. Given the above differences, the pre-processing pipeline used for 2D-EPI fMRI data may not be optimal for 3D-EPI data.

Using unsmoothed data, 3D-EPI generally showed more extensive activations in motor cortex during finger tapping than 2D-EPI, but significantly smaller % BOLD signal changes. This may, in part, be due to the fact that both imaging parameters and processing pipelines are optimized for 2D-EPI (Bernstein et al., 2004; Scouten et al., 2006), compared to non-optimal pre-processing pipelines for 3D-EPI data. The finding of more voxels showing signal increases during finger tapping is consistent with the higher number of 3D brain voxels with significant tSNR values mentioned earlier. As expected, 6.6 mm spatial filtering increased the number of activated voxels in the motor cortex region while reducing their mean percent BOLD signal change, irrespective of acquisition and motion protocol. The larger number of voxels in 2D than 3D data with tSNR values between 100 and 199 after 6.6 mm spatial filtering did not, however, consistently result in larger % BOLD signal changes nor more extensive activations.

Increasing spatial smoothing in the pre-processing pipeline was associated with decreasing % BOLD signal changes and increasing numbers of activated voxels in the motor cortex, irrespective of acquisition sequence and motion protocol. The larger decrease in % BOLD signal change seen in 2D than 3D data when applying 3.3 mm spatial filtering may be the result of averaging innately separate activations (Geissler et al., 2005), which seem to affect 3D EPI data less. MoCo 3D EPI may be more robust to spatial smoothing due to the additional averaging along the slice-encode direction during 3D Fourier transform.

This work demonstrated also that our $vSNav$ 3D-EPI enables acquisition of consistent fMRI data with better tSNR. From the spatially unsmoothed data, for instance, NoCo 3D-EPI with pitch head motion resulted in 109 and 34 active voxels with 2.99% and 3.98% mean % BOLD signal changes during right- and left-hand finger tapping, respectively (Figure 3-8). However, the MoCo 3D-EPI acquisitions resulted in 125 and 84 activated voxels with 2.90% and 4.53% mean percent BOLD signal changes during right- and left-hand tapping, respectively. Similarly, NoCo 3D-EPI acquisitions with yaw head motion resulted in 187 and 75 active voxels with 2.45% and 3.52% mean percent BOLD signal changes, respectively, while MoCo 3D-EPI acquisitions with identical head motion resulted in 146 and 127 active voxels with 3.43% and 3.57% mean percent BOLD signal changes, respectively. Although increasing spatial smoothing of MoCo 3D-EPI acquisitions with pitch and yaw head motions resulted in increasing numbers of active voxels and decreasing mean percent BOLD signal changes, irregular and unexpected trends were observed in spatially smoothed NoCo 3D-EPI

acquisitions with the same head motions. These results demonstrate that the pre-processing pipeline alone was not able to remove motion induced artifacts in the absence of prospective motion correction.

Based on widely recommended fMRI pre-processing pipelines (Mikl et al., 2008; Worsley & Friston, 1995) and our results showing marginal tSNR gains for smoothing with filters >6.6 mm, we used 6.6 mm (or twice the in-plane voxel size) spatially smoothed data to generate activation maps. The activation maps from first-level analyses shown in Figure 3-11 demonstrate that the $vSNav$ 3D-EPI is capable of detecting and correcting intentional and unintentional head motions in real time such that the resulting activation maps are comparable to those from 2D-EPI acquisitions with standard PACE motion correction. Surprisingly, the most spurious activations were detected in the MoCo 2D-EPI acquisition with leg motion; there were little or no spurious activations in the MoCo 3D-EPI acquisition with leg motion. Since the induced motions (opening/closing the legs) were performed at discrete times (in task rest blocks) during the acquisition, these were not correlated with the task and are likely not the source of these spurious activations. Standard and extended residual motion parameters were also included as regressors during 2D- and 3D-EPI data analyses to reduce the impact of any task uncorrelated motion. It is more likely that the finger tapping task itself caused participant head movement; such task correlated motion could account for the observed spurious activations. Our results demonstrate that the $vSNav$ 3D-EPI sequence minimizes the degradation of the BOLD signal quality in the presence of motion. Activation maps from first-level analyses of NoCo 3D-EPI acquisitions with pitch and yaw head motions demonstrated that the pre-processing pipeline could not completely recover BOLD signals corrupted by motion artifacts. In contrast, the activation maps of MoCo 3D-EPI acquisitions with pitch and yaw head motions demonstrated fewer spurious activations.

3.5. Conclusion

This work demonstrated that our $vSNav$ 3D-EPI sequence is robust to motion artifacts and generates fMRI results that are comparable to those of 2D-EPI with PACE. Irrespective of the motions performed, the number of brain voxels with inherently high tSNR values were greater in 3D- than 2D-EPI acquisitions. The pre-processing pipeline applied on 3D-EPI data appeared to not be as effective as the one used for 2D-EPI data. To maximize the robustness and effectiveness of $vSNav$ 3D-EPI, an optimized pre-processing pipeline should be developed. Since $vSNav$ 3D-EPI does not require additional time, pulses, or hardware to detect subject

motion in real time, it can be integrated with other prospective motion correction techniques so that intra-volume motion correction can be performed in real time.

Chapter Four

4. Double Volumetric Self-Navigators for Accelerated Prospective Motion Correction for 3D EPI Acquisition

4.1. Introduction

Subject motion in MRI is one of the most common sources of confounding artifacts, and more so in repetitive MR acquisitions like functional MRI (fMRI). FMRI employs repeated acquisition of a volumetric image to measure the temporal evolution of signal intensities in voxels. Any subject motion during scanning will, however, cause voxels to represent different anatomical locations at different times of the scan and, depending on the severity of the motion, may lead to reduced statistical power to detect temporal changes (Hajnal et al., 1994; Power et al., 2012; Satterthwaite et al., 2012; van Dijk et al., 2012) or even data corruption. The inherent need for repetitive scanning in fMRI increases the total acquisition time and incidence of subject motion – even young motivated volunteers have been shown to induce involuntary motions of up to $2\,mm$ translation and 1^0 rotation (Zaitsev et al., 2017). The incidence of subject motion generally increases in clinical fMRI where its degree or frequency depends on various factors, including the type of experiment, and the sex, age, state and health of the subject (Mayer et al., 2007; Poldrack et al., 2002; Seto et al., 2001; Yuan et al., 2009). The unlimited possible combinations of these factors makes it impossible to predict how a person may move during a scan, and to prevent or compensate for such motion. This is also why retrospective motion correction remains one of the most important components of image pre-processing in fMRI (Chen & Glover, 2015).

The inevitability of motion artifacts in fMRI has led to various motion minimization strategies such as using cushions to improve comfort and minimize the spaces between the head and head-coil, the use of bite bars while performing motor tasks (Menon et al., 1997), a restraining helmet (Hadj-Bouziane et al., 2014) or sedation (Bernal, 2012). However, these techniques have their own limitations and problems. For instance, cushions are ineffective, and discomfort is not the only factor that causes motion. Bite bars require subjects to bite the bar with their teeth. In addition to this being a task in itself, bite bars are uncomfortable, incur additional costs, and require additional work as they must be cleaned and sanitized before and/or after each use. Helmets incur additional financial costs compounded by head-size differences and they are often uncomfortable. Sedation requires anaesthesia, which increases

both the cost and risks of MRI, and is not viable for fMRI experiments that require subjects to be awake to perform a task. Therefore, substantial research has focused on developing improved retrospective and prospective motion correction techniques to minimize the effects of subject motion in fMRI.

Retrospective motion correction techniques measure and correct motion using completely acquired data. While different fMRI analysis software packages employ different algorithms (Cox, 1996; Karl J. Friston et al., 1995; Goebel et al., 2006; Jenkinson et al., 2002), they all involve realigning repeated imaging volumes to each other. Although retrospective motion correction has been shown to improve the magnitude and cluster size of detected activations (Oakes et al., 2005), insufficiently corrected or uncorrected motion might induce subtle alterations to the functional analysis results. For instance, in resting-state fMRI, uncorrected or insufficiently corrected motion artifacts decreased the intrinsic functional coupling among associated brain regions while increasing intrinsic local functional coupling (van Dijk et al., 2012). In task-based fMRI, insufficient correction of subject motion that is uncorrelated to the functional task increases noise resulting in reduced activations, while motion that is (weakly) correlated to the task may result in false activations (Hajnal et al., 1994).

Notably, co-registering successively acquired image volumes to each other as described above does not correct image degradation resulting from motion *within* individual image volumes. Correcting motion artifacts within image volumes requires an estimate of the motion to solve the inverse forward model given by equation (4.1):

$$E\rho = m, \tag{4.1}$$

where E is the encoding matrix that contains information regarding motion and coil sensitivities, ρ is the artifact-free image and m is the measured image. However, its performance depends, among others, on the number and accuracy of the encoding matrix elements, the criteria to stop the iteration and the cost function (Batchelor et al., 2005; Paige & Saunders, 1982).

Various k-space filling trajectories have been developed to enhance retrospective motion correction by providing a more accurate motion estimate. These techniques, collectively referred to as self-navigation techniques, rely on estimating motion by repeatedly sampling certain parts of k-space. One widely known self-navigation technique known as PROPELLER (Periodically Rotated Overlapping Parallel Lines with Enhanced Reconstruction) fills two-dimensional (2D) k-space by rotating a rectangular strip of parallel k-space lines about the origin (Pipe, 1999). PROPELLER-EPI – a PROPELLER implementation using multi-shot EPI

– samples a circular area around the origin of k-space repeatedly and estimates motion based on the positional inconsistencies of the strips (Krämer et al., 2012). However, PROPELLER-EPI has lower temporal resolution than single-shot EPI because of redundant k-space sampling. The Trajectory Using Radially Batched Internal Navigator Echoes (TURBINE) self-navigator is a hybrid radial-Cartesian sampling scheme. TURBINE fills a cylindrical 3D k-space volume blade-by-blade, where each blade spans the diameter and height of the cylinder and is filled in a cartesian trajectory (Graedel et al., 2017). Rigid body motion is estimated from two or more blades where more blades increase accuracy of motion estimation at the expense of temporal resolution. TURBINE acquisition has lower BOLD signal sensitivity than a matched 3D EPI acquisition (Graedel et al., 2022).

Self-navigators that require transforming data from radial to cartesian coordinates use interpolation (i.e., approximated data) to fill the missing parts of the cartesian k-space. Retrospective motion correction processes data from k-space trajectories that are fixed in the device coordinate system. Therefore, rotational components of subject motion induce a sampling artifact, also known as "pie-slice", which violates the Nyquist criterion (Korin et al., 1995). Overall, the widely used retrospective motion correction approaches have been unable to completely remove subtle functional networks induced by subject motion (Yan et al., 2013).

The availability of large, validated MR data sets in combination with recent advances in graphic processing unit (GPU) technologies and mathematical models have led to a rapid increase in the application of machine learning algorithms to MR image processing. Initial applications of machine learning for automatic identification of abnormalities on structural brain images have been promising. To date, these techniques are, however, unable to localise or classify the artifacts and are restricted to evaluating abnormalities in MR images with the same contrast and voxel geometry as the training data (Esses et al., 2018; Sujit et al., 2019). Machine learning algorithms implemented over interconnected computing units, known as artificial neural networks, have been applied to remove motion artifacts in MR images. Neural network architectures such as convolutional neural networks (CNNs) have been applied to perform spatially resolved motion detection, for example in T1-weighted MR images of the head and upper abdomen (Küstner et al., 2018) and to remove motion artifacts, for example from contrast enhanced liver MR images (Tamada et al., 2020), out-of-FOV motion artifacts on MPRAGE (magnetisation prepared rapid gradient echo) brain images (Wang et al., 2020), and to reduce effects of residual motion artifacts after application of conventional motion corrections in diffusion MRI (Gong et al., 2021). Other neural network architectures such as

generative adversarial networks (GANs) have been applied to remove rigid and non-rigid motion artifacts (Armanious, Gatidis, et al., 2020; Armanious, Jiang, et al., 2020). Although the use of machine learning algorithms in retrospective motion correction has been promising, its clinical applications have yet to be assessed.

In contrast to retrospective techniques, prospective motion correction (PMC) aims to keep the imaging field of view (FOV) fixed to a target by tracking the target's motion and realigning the FOV whenever motion is detected. Various approaches can be used to track the target's motion. Hardware-based approaches involve attaching fixed markers (Todd et al., 2015; Zaitsev et al., 2006) or coils (Derbyshire et al., 1998; Ooi et al., 2009) to the target. These devices, however, require setup and calibration and may be costly. Moreover, their accuracy depends on how the markers are attached to the subject, which may also compromise subject comfort (Maclaren et al., 2013). Another approach is to use navigators, which are acquisitions inserted into an imaging sequence to rapidly acquire one-, two- or three-dimensional low-resolution snapshot images of an anatomical region throughout the acquisition for motion estimation (Alhamud et al., 2012; Hess et al., 2011; Tisdall et al., 2012; Van Der Kouwe et al., 2006; Zhuo Wu Fu et al., 1995). However, navigators need additional gradient and RF pulses to construct the low-resolution images which may be difficult to accommodate in crowded pulse sequences like EPI without increasing the total acquisition time.

Previously, we demonstrated that a subset of partitions during a 3D EPI acquisition could be used as a volumetric self-navigator ($vSNav$) to successfully measure and correct subject motion during the acquisition without needing to introduce any additional gradient pulses, RF pulses or external hardware (Bayih et al., 2022). Our previous implementation which used 24 of 52 partitions to construct the $vSNav$, however, only corrected motion once during the acquisition and only 11 partitions after acquisition of the navigator data. In the present work we aimed to increase the temporal resolution and accuracy of the motion detection and correction by using fewer partitions to construct the volumetric self-navigators, and reducing the computational time, which delays the implementation of the FOV update. Here we use two different subsets of the kz partitions to construct two volumetric self-navigators ($dvsNav1$ and $dvsNav2$) during each volume acquisition. The navigators (i.e., $dvsNav1i$ and $dvsNav2i$) that are constructed during the i^{th} (where $i \neq 1$) volume acquisition are then compared to their corresponding reference volumes (i.e., $dvsNav1Ref$ and $dvsNav2Ref$) constructed during the 1^{st} volume acquisition to compute motion parameters, and corrections are applied to the imaging FOV before the next subset of kz partitions starts to be accumulated.

4.2. Methods

4.2.1. Double volumetric-self-navigated 3D-EPI sequence development

The 3D-EPI sequence uses a center-out acquisition scheme that fills 3D k-space starting from the center partition and moving outwards, successively acquiring partitions either side of the central partition. Each partition is filled following a cartesian trajectory (see Figure 4-1 (a)). Since the center-out scheme first acquires low-frequency partitions that contain more energy, subject motion can be estimated from a small subset of these partitions leaving enough partitions to construct another navigator before completing the acquisition of the volume. To implement this technique, the image reconstruction pipeline (IRP) was modified to include a "feedback block" that successively accumulates two separate subsets of the data being acquired by the online block to two separate and distinct objects. Immediately following the accumulation of the required number of partitions to a particular object, a volumetric image (i.e., a self-navigator) is constructed and motion is estimated. Using the two successively acquired volumetric self-navigators, motion can therefore be estimated twice during the acquisition of a volume. The feedback block sends these motion estimates back to the sequence as they become available. The online block was modified to receive motion parameters from the feedback block twice during each volume acquisition and to re-adjust its FOV accordingly.

4.2.2. Double volumetric-self-navigator design

The feedback block successively constructs two volumetric images, also referred to as double volumetric self-navigators ($dvsNavs$). The first self-navigator of the i^{th} volume acquisition ($dvsNav1_i$) is constructed by accumulating the first l partitions of a volume with n partitions and filling the remaining $n - l$ partitions with zero. This is equivalent to applying a low-pass filter in the partition direction (see Figure 4-1 (b)). After accumulating l partitions, the feedback block stops accumulating the next r partitions to allow time to construct $dvsNav1_i$, estimate motion and send the motion parameters to the sequence. The number of partitions skipped before the feedback block again resumes accumulation of partitions, depends on the time required for these operations. To construct the second volumetric self-navigator of the i^{th} volume ($dvsNav2_i$), the feedback block accumulates the next m partitions and fills the remaining $n - m$ partitions with zeros (see Figure 4-1 (c)). No further partitions are accumulated to the feedback block until the start of the next $((i + 1)^{th})$ volume acquisition.

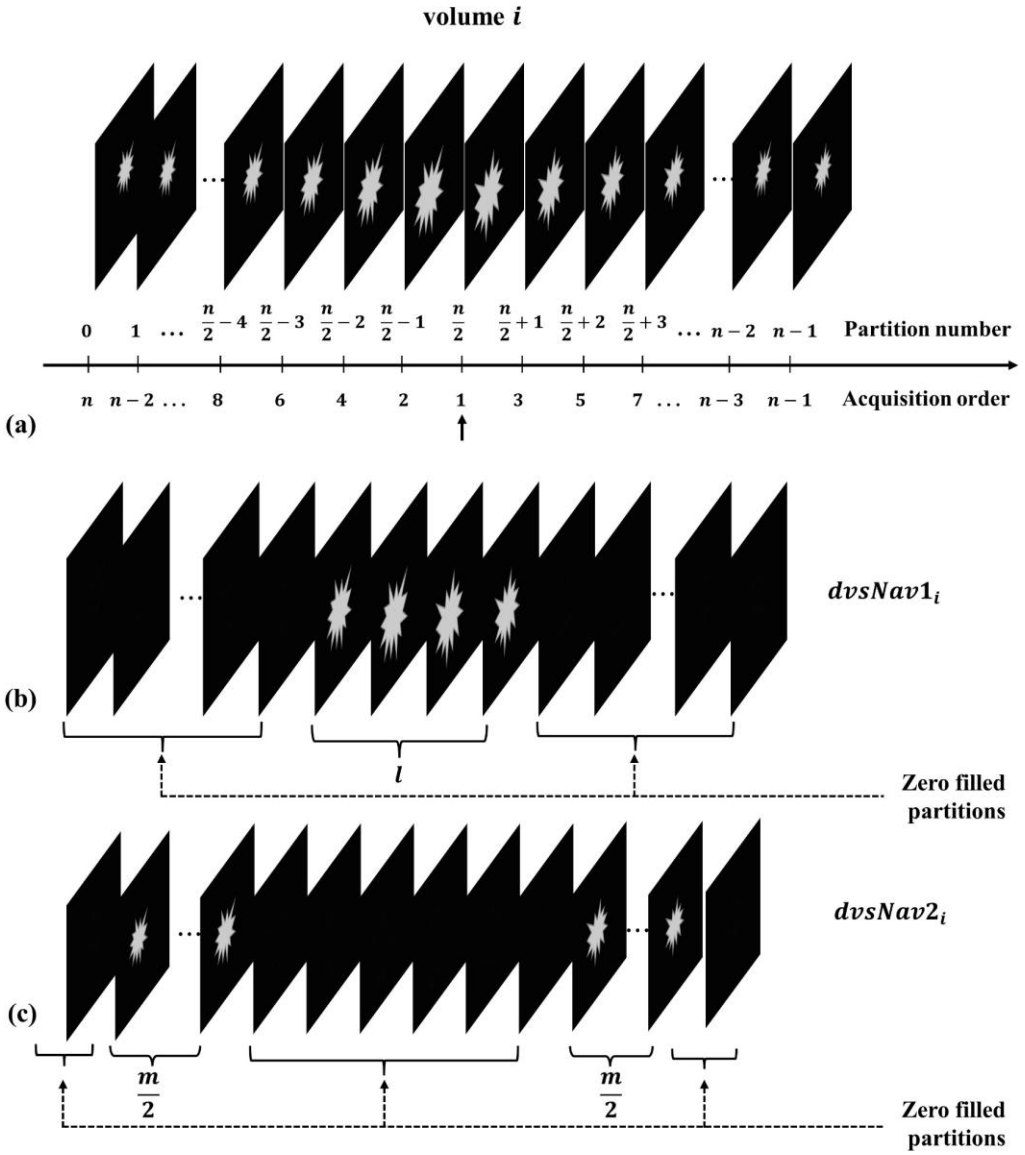

*Figure 4-1 Center-out acquisition scheme and double volumetric-self-navigator ($dvsNav$) construction during the i^{th} volumetric acquisition. (**a**) The relative positions of the n partitions with respect to the isocenter (indicated by the arrow) and their order of acquisition. (**b**) The first volumetric-self-navigator of the i^{th} volume ($dvsNav1_i$) is constructed from l partitions, with remaining partitions zero filled (low-pass filtering). (**c**) The second volumetric-self-navigator of the i^{th} volume ($dvsNav2_i$) is constructed from m partitions, with the remaining partitions zero filled (band-pass filtering).*

4.2.3. Real-time motion detection

During each volume acquisition, a time $\Delta t_1 = l * TR$ is required to accumulate the first l partitions, where TR is the partition repetition time. Immediately after accumulation of l partitions, the feedback block constructs the first volumetric self-navigator for that volume ($dvsNav1_i$). If $i = 1$, the $dvsNav1_i$ is set as the first reference volume ($dvsNav1_{Ref}$), but if $i > 1$, the feedback block estimates the position of $dvsNav1_i$ relative to $dvsNav1_{Ref}$ using the Siemens prospective acquisition correction (PACE) algorithm (Thesen et al., 2000). PACE outputs six motion parameter values – three for translation and three for rotation. Assuming

the feedback block requires a time Δt_2 to fill the remaining $n - l$ partitions with zero, construct $dvsNav1_i$, estimate motion, and send the motion parameters to the sequence, the imaging FOV will be updated at a time $\Delta t_1 + \Delta t_2$ after the start of the i^{th} volume acquisition and the remaining partitions are acquired with this updated FOV. This time, Δt_2, therefore determines the number of skipped partitions, *r*, before accumulation of partitions to the feedback block can resume. Of the remaining (*n-l-r*) partitions, the next m partitions are accumulated to the feedback block in a time $\Delta t_3 = m * TR$ for construction of the second volumetric self-navigator ($dvsNav2_i$). If $i = 1$, $dvsNav2_i$ is set as the second reference volume ($dvsNav2_{Ref}$), but if $i > 1$, the feedback block again uses PACE to estimate the position of $dvsNav2_i$ relative to $dvsNav2_{Ref}$. Assuming the time required by the feedback block to fill the remaining $n - m$ partitions of the second volumetric self-navigator with zero, construct $dvsNav2_i$, estimate motion, and send the motion parameters to the sequence is given by Δt_4, the imaging FOV will be updated for a second time at a time $\Delta t_1 + \Delta t_2 + \Delta t_3 + \Delta t_4$ after the start of the i^{th} volume acquisition. Although the feedback block stops accumulating partitions during Δt_2 and Δt_4, the online block accumulates all partitions of the volume (see Figure 4-2).

4.2.4. Real-time motion correction considerations

The temporal resolution of motion correction during volume acquisition is limited by the number of partitions that need to be accumulated by the feedback block to construct $dvsNavs$ with enough features for accurate co-registration. On one hand, reducing the number of partitions accumulated to construct the navigators increases temporal resolution but reduces sensitivity to and accuracy of motion detection. In $dvsNav1_i$, sensitivity to detect through-plane motion is reduced due to excessive spatial smoothing in the partition direction, while the accuracy of motion detection in $dvsNav2_i$ is reduced due to insufficient features in the self-navigator images for accurate co-registration. On the other hand, increasing the number of partitions accumulated to construct the navigators delays the timing of motion correction but increases the accuracy of motion estimation. Therefore, the number of partitions used to construct the $dvsNavs$ requires a trade-off between latency and accuracy of motion estimation. During acquisition of the i^{th} volume where $i \neq 1$, $dvsNav2_i$ is constructed from partitions that were motion corrected based on motion estimates derived from $dvsNav1_i$, and $dvsNav1_i$ for $i > 2$ is constructed from partitions that were motion corrected based on motion estimates derived from $dvsNav2_{(i-1)}$.

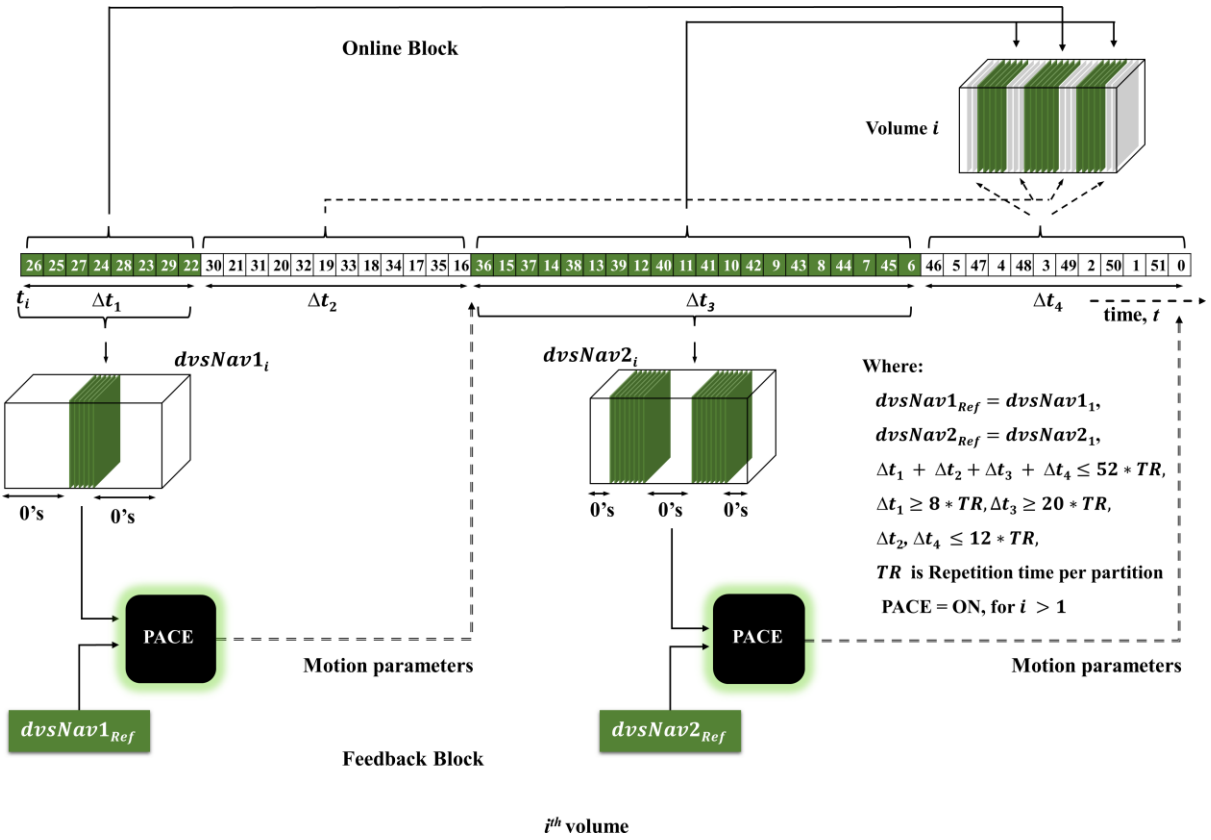

Figure 4-2 Illustration of the double volumetric self-navigator motion correction scheme for a single (i^{th}) volume comprising 52 partitions. The Feedback block takes time Δt_1 to accumulate the first subset of partitions and time Δt_2 to zero fill the remaining partitions, construct the 1st volumetric self-navigator ($dvsNav1_i$), estimate its position relative to the first reference self-navigator ($dvsNav1_{Ref}$) and send motion estimates to the sequence. The Feedback block takes time Δt_3 to accumulate the second subset of partitions and time Δt_4 to construct the 2nd volumetric self-navigator ($dvsNav2_i$), estimate its position relative to the 2nd reference volumetric self-navigator ($dvsNav2_{Ref}$) and send motion estimates to the sequence. All 52 partitions are accumulated to the online block in a time $52 * TR$, where TR is the partition repetition time. In the current implementation, TR = 64 ms.

In our current work, the feedback block was designed to detect and correct motion twice per volume with each $dvsNav$ constructed from partitions that were acquired in the updated FOV. Hence synchronization of motion detection and motion correction was critical. The first step involved measuring the feedback block computation time, which is comprised of the time required to construct the navigator image, co-register it to a corresponding reference volume, send motion parameters to the sequence, and update the FOV. Notably, the computation time varies depending on the number of channels in the head coil. It was shown previously (Bayih et al., 2022) for a partition-TR of 64 ms and 20-channel head/neck coil, that all computations required by the feedback block could be completed in the time it takes to acquire 11 partitions (i.e. 11*TR). In contrast, it took the equivalent of 12 partitions (i.e. 12*TR) to complete the computations for a 32-channel head coil. As such, the total computation time required for two

self-navigators with the 32-channel head coil will be 24*TR, leaving 28 partitions available to construct the two navigator images. Since the center partitions contain more energy, the feedback block was configured to accumulate the first 8 partitions to $dvsNav1$. After skipping the 12 partitions needed for the computations related to $dvsNav1$, the remaining available 20 partitions are accumulated to $dvsNav2$ (Figure 4-2).

In our previous work we found that the synchronization point – defined as the total number of partitions accumulated by the online block from the start of a volume acquisition until receiving motion parameters from the feedback block – varies depending on the number of channels in the head coil. Since the synchronization points of the IRP should be consistent irrespective of varying numbers of channels in the head coil, it was important to determine the optimal synchronization points for both $dvsNav1$ and $dvsNav2$. To examine the effect of varying numbers of channels on the synchronization points, the IRP was configured with feedback blocks accumulating partition data from different numbers of spatially distributed channels of a 32-channel head coil. In each case, the volumetric self-navigators were constructed, motion was estimated, and the synchronization points were measured. Table 4-1 shows synchronization points of the IRP for feedback blocks accumulating partition data from 12, 16, 20, 24, 28 and 32 channels of a 32-channel head coil.

Table 4-1 Synchronization points of the image reconstruction pipeline (IRP) for feedback blocks accumulating partition data from 12, 16, 20, 24, 28 and 32 channels of the 32-channel head coil.

		Number of channels					
		12	**16**	**20**	**24**	**28**	**32**
IRP Synchronization points	***dvsNav1***	18	19	19	19	20	20
	dvsNav2	50	51	51	51	51	51

The relative accuracies of motion estimates from self-navigators constructed using partitions from varying numbers of channels was tested offline. Six volumes of 3D EPI data were first acquired for a High Precision Devices (HPD) system phantom using the 32-channel head coil with the feedback block disabled; the phantom was moved during the acquisition of the 2nd volume. Sequence parameters were: TR 64 ms, TE 30 ms, voxel size 3.1 x 3.1 x 3.1 mm^3, acquisition matrix 64 x 64 x 52, FOV 200 x 200 mm^3, bandwidth 2298 Hz/px, flip angle 16° fat saturation ON. The IRP was then run offline using the acquired raw data with the feedback block active and accumulating partitions from all 32 channels of the head coil (referred to as the 32-channel feedback block). The two volumetric self-navigators

were constructed and motion parameters estimated. These IRP steps were repeated with the feedback block accumulating partitions from only 28, 24, 20, 16 and 12 channels, respectively, of the head coil. The motion parameters estimated by feedback blocks with partition data from different numbers of channels are shown in Figure 4-3. Since the raw data were acquired using a 32-channel head coil, motion parameters estimated using the 32-channel feedback block are assumed to be most accurate. Motion estimates are seen to be similar for self-navigators constructed using data from 20 or more channels.

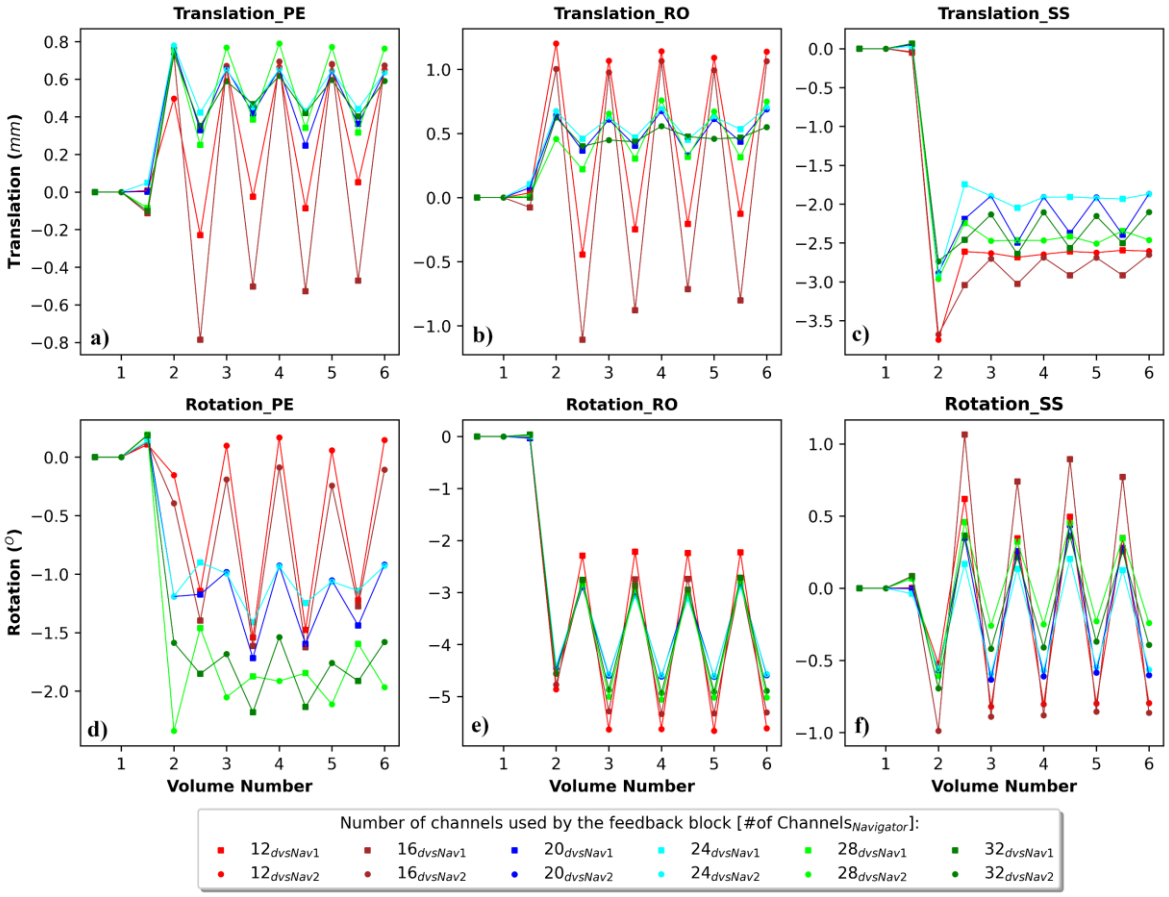

Figure 4-3 Motion estimates computed by the feedback block using partitions from 12, 16, 20, 24, 28 and 32 channels of the 32-channel head coil. Estimated translational and rotational motion components in the phase-encoding (a and d), read-out (b and e), and slice-select (c and f) directions are shown.

Based on a trade-off between synchronization point (Table 4-1) and accuracy (Figure 4-3), the 20-channel feedback block was selected for this work. That means, if a head coil with ≤ 20 channels is used, the feedback block will accumulate partition data from all the channels, while only partition data from 20 channels will be used for a head coil with >20 channels. With this scheme, motion parameters will be received from the feedback block by the 19th and 51st partitions, respectively. During acquisition of the i^{th} volume, the feedback block accumulates the 1st incoming 8 partitions to construct $dvsNav1_i$; this takes $\Delta t_1 \cong 512$ ms (i.e., 8*TR) for

TR 64 ms. For data from 20 channels, it takes $\Delta t_2 \cong 704$ ms (i.e., $11 * TR$) to construct $dvsNav1_i$, estimate and send motion parameters to the sequence; no partitions are accumulated to the feedback block during this time. To ensure that the next set of partitions accumulated to the feedback block are all in the readjusted FOV, our feedback block waits another 64 ms (1 * TR) before accumulating the 20 partitions for $dvsNav2_i$ in a time $\Delta t_3 \cong 1280$ ms (i.e., $20 *$ TR). Construction of $dvsNav2_i$, motion estimation and feedback to the sequence takes $\Delta t_4 \cong 704$ ms (i.e., 11*TR), during which time no new partitions are accumulated to the feedback block. As before, our feedback block waits another 64 ms (1 * TR) before starting to accumulate partitions again, thereby ensuring that the next set of accumulated partitions are in the readjusted FOV. Limiting the number of channels to 20 therefore ensures synchronization of motion detection with motion correction so that the next $dvsNav$ is always constructed from motion corrected partitions.

The online block of the IRP (Figure 4-2) accumulates all the partitions of a given volume before constructing the volumetric image. Notably, the FOV is updated twice during the acquisition. Therefore, the quality of the volumetric data depends on the performance of the feedback block, which in turn depends on the number and position of partitions used to construct the $dvsNav$s, the imaging parameters, and the severity of subject motion. There are two instances when the feedback block will not send motion parameters to the sequence: (i) if the estimated translation or rotation values are greater than $20\ mm$ or 8°, respectively, or (ii) if the $dvsNav$s do not have enough features for PACE to estimate motion.

The IRP displays the slices of each volume and each $dvsNav$ in mosaic format. The motion parameters are additionally overlaid on the mosaic images for each $dvsNav1$ and $dvsNav2$.

4.2.5. Sequence validation

The double volumetric self-navigated 3D-EPI sequence was validated both in a phantom and in vivo in two healthy male volunteers (ages 31 and 37 years). All scans were performed on a 3 T Skyra (Siemens Healthcare, Erlangen, Germany) located at the Cape Universities Body Imaging Centre (CUBIC) in Cape Town, South Africa, according to protocols that had been approved by the Faculty of Health Sciences Human Research Ethics Committee of the University of Cape Town. The volunteers provided written informed consent.

For the phantom scans, the High Precision Devices (HPD) system phantom model 130, which contains 5 plates, 57 fiducial spheres and 2 wedges, was scanned (Figure 4-4) in the 20-channel Head/Neck coil. The sequence parameters were as follows: TR = 64 ms, TRvol = 3.33

s, TE = 30 ms, voxel size 3.3 x 3.3 x 3.1 mm^3, acquisition matrix = 64 x 64 x 52, FOV = 200 x 200 mm^2, bandwidth 2298 Hz/px, flip angle 16º, 36 volumes with fat saturation ON. The same sequence parameters were used for in vivo acquisitions except that 50 volumes were acquired. The parameters were selected to be similar to those typically used during an fMRI BOLD acquisition using 3D-EPI. The phantom images were acquired in the coronal orientation where slice select is anterior-posterior and phase encoding is left-right. The in vivo images were acquired in the sagittal orientation where slice select is right-left and phase encoding is anterior-posterior.

Figure 4-4 High Precision Devices (HPD) system phantom model 130

The phantom scans were performed first without motion and next with motion; in both scans, real-time motion correction was active. During the scans with motion, four discrete motions were induced manually by moving the pad supporting the phantom first to the right during volume 7, then to the left around the start of volumes 13 and 19, and finally slow motion to the right during volume 25.

During the in vivo scans, participants were asked to move their head at particular time points, remaining still at each new position until they were instructed to move their head. Specifically, the participants were asked to rotate their head to the right around volume 10, rotate back to the center around volume 20, rotate to the left around volume 30, and finally rotate back to the center around volume 40, remaining still until the end of the acquisition. The amount of the motion was controlled by marking three dots on the inside surface of the scanner bore – one dot directly in line with the subject's line-of-sight (center mark), one dot approximately 8 cm to the left of the center mark, and another approximately 8 cm to the right of the center mark. When instructed to move, the participants turned their head to face the relevant mark (center, left or right). The in vivo scans were performed first without motion while real-time motion correction was active, second with discrete motions while real-time motion correction was inactive, and finally with discrete motions while real-time motion

correction was active. In vivo data were further processed using FMRIB's Linear Image Registration Tool (FLIRT) (Jenkinson et al., 2002) to assess residual motions in each volume.

4.3. Results

4.3.1. Phantom data

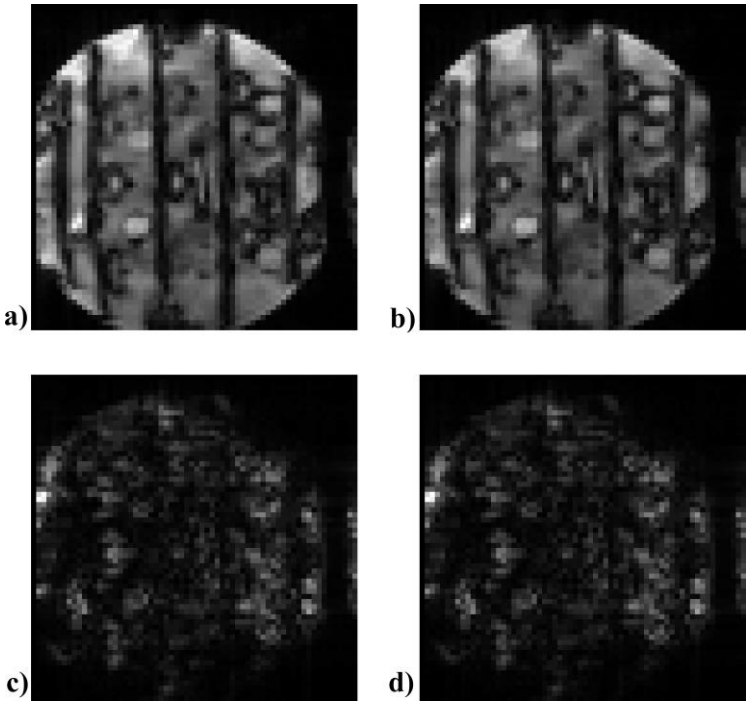

Figure 4-5 The images in the top row show the central slice of the first volumetric self-navigator (dvsNav1) for two consecutive volumes when scanning a phantom (i.e. volumes 1 and 2), and the bottom row shows the central slice of the second self-navigator (dvsNav2) for the same two volumes. The phantom was scanned in the sagittal orientation; the slice-select gradient was from left to right and phase encoding from anterior to posterior.

The top and bottom images in Figure 4-5 show the central slices of the 1st and 2nd volumetric self-navigators (*dvsNav1 and dvsNav2*), respectively, constructed by our double volumetric self-navigated 3D-EPI sequence for two consecutive volumes during a phantom scan. The images on the left are for the 1st volume acquisition (i.e. the reference volume), and those on the right from the second volume acquisition. Motions are estimated by co-registering subsequent *dvsNavs* ($dvsNav_i$, $i>1$) to their corresponding (i.e. 1st or 2nd) reference *dvsNav*.

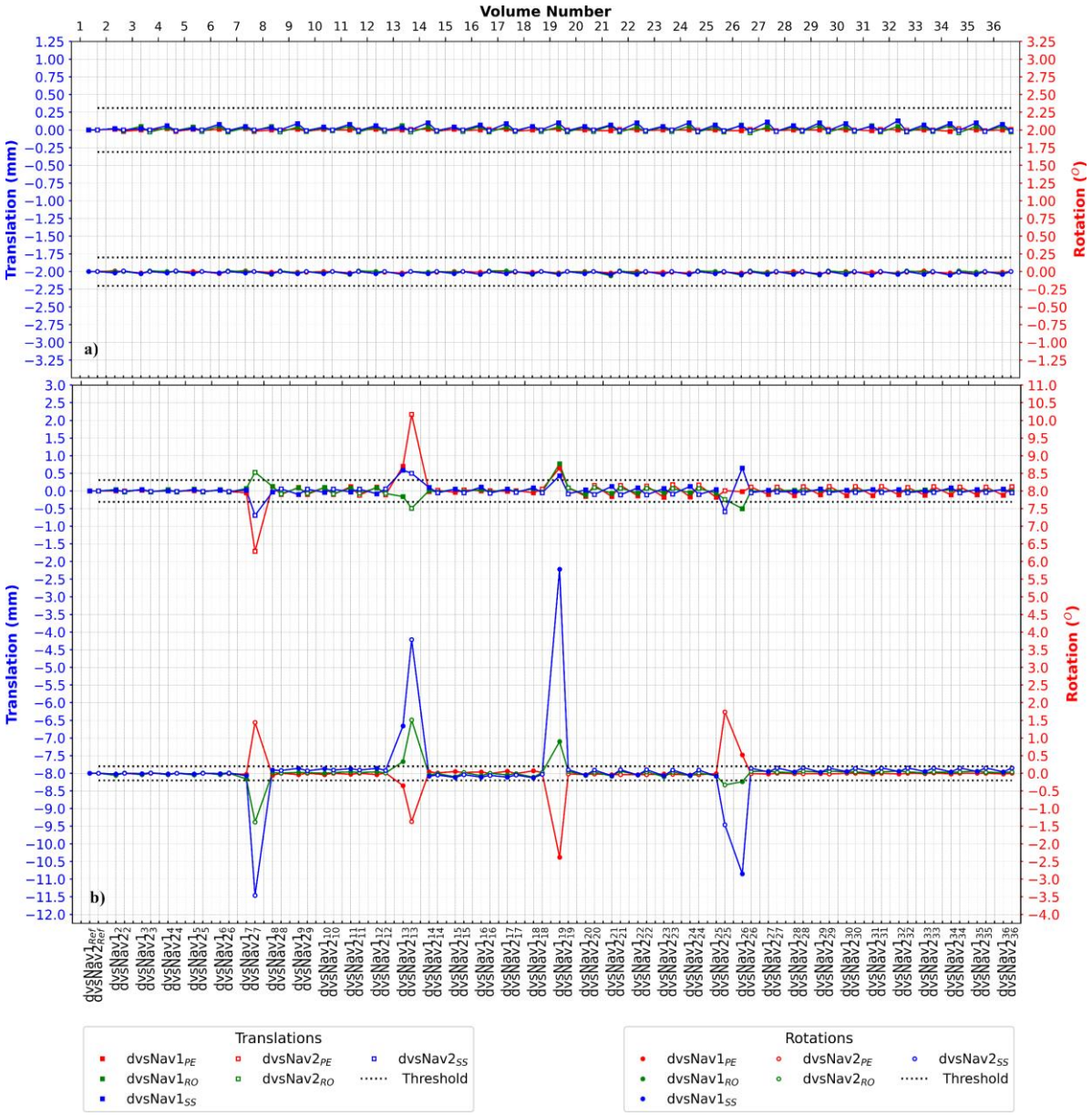

Figure 4-6 Plots showing for each volume the position of the phantom in the imaging FOV relative to its position during the first volume as measured by $dvsNav1$ and $dvsNav2$ with a) no motion, and b) motion induced during measurements 7, 13, 19 and 25. Images were acquired in the coronal orientation with phase encoding left-right and readout inferior-superior directions.

Figure 4-6 (a) shows that motion estimates for the phantom in the absence of motion are stable although there were below threshold through-plane oscillations. Figure 4-6 (b) shows the two batches of motion estimates when the phantom was moved briefly during the 2nd navigator of the 7th volume (i.e., $dvsNav2_7$), when the phantom was moved for a period that spans over the 1st and 2nd navigators of the 13th volume (i.e., $dvsNav1_{13}$ and $dvsNav2_{13}$), when the phantom was moved briefly during the 1st navigator of the 19th volume (i.e., $dvsNav1_{19}$), and when the phantom was moved for a period that spans over the 2nd navigator of the 25th and 1st navigator of the 26th volumes (i.e., $dvsNav2_{25}$ and $dvsNav1_{26}$). In all of

these cases, the 3D EPI successfully adjusted its FOV so that subsequent volumes were acquired with below threshold motion estimates. Figure 4-7 (a) shows the central slice of the 1st volume, and Figure 4-7 (b) – (e) the absolute difference images between the central slices of the volumes acquired before and after the motion occurred.

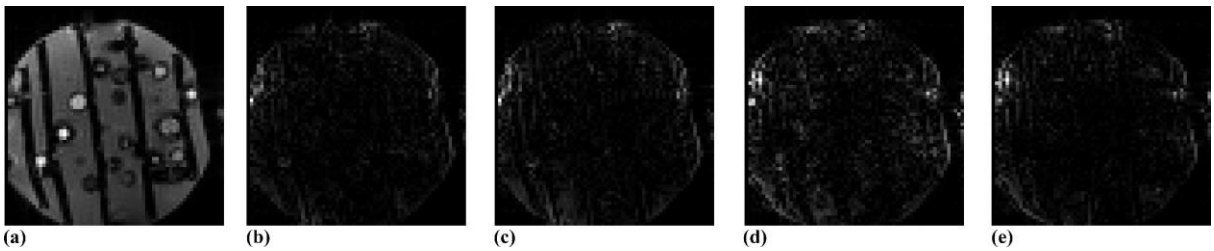

Figure 4-7 Images showing (a) the central slice of the first volume, and difference images between (b) the central slice of volumes 6 and 8, (c) volumes 12 and 14, (d) volumes 18 and 20, and (e) volumes 24 and 27.

4.3.2. In vivo data

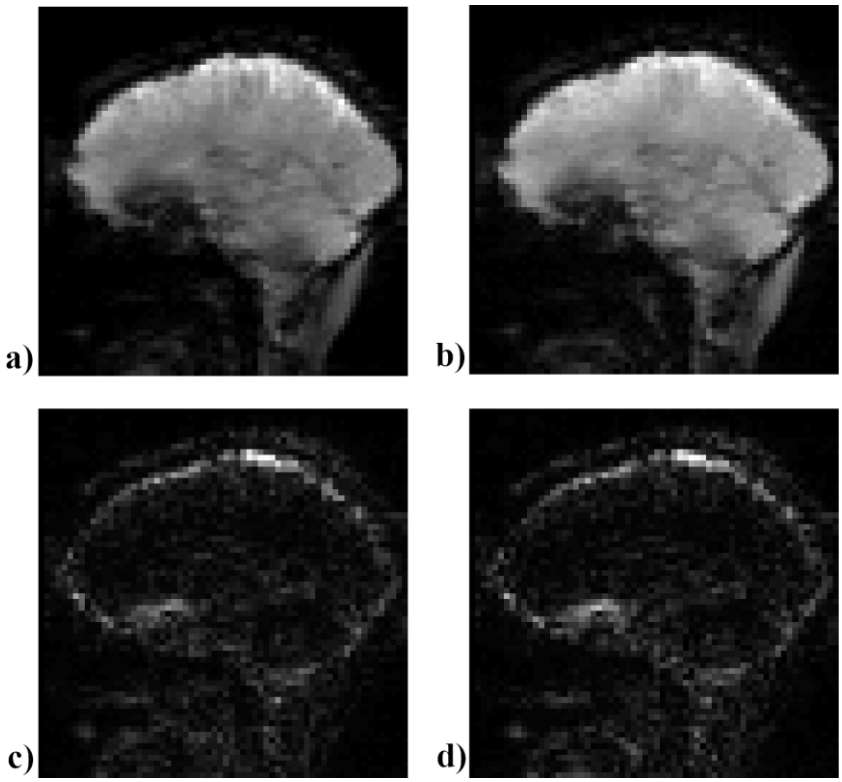

Figure 4-8 The images in the top row show the central slice of the first volumetric self-navigator (dvsNav1) for two consecutive volumes (volumes 1 and 2) during in vivo imaging, and the bottom row shows the central slice of the second self-navigator for the same two volumes. Volumes were acquired in sagittal orientation; slice select was from left to right and phase encoding from anterior to posterior.

Figure 4-8 shows the central slices from two consecutive volumes (left volume 1, right volume 2) for each of the two double volumetric self-navigators (top *dvsNav1*, bottom *dvsNav2*) constructed during an in vivo acquisition.

Figure 4-9 shows for one volunteer how head position in the imaging FOV changes relative to its position in the 1st volume for acquisitions (a) without intentional motion (NoMo), (b) with intentional motion but feedback to the sequence disabled (NoCo), and (c) with intentional motion and feedback to the sequence enabled (MoCo). The plots show the motion parameters estimated prospectively by the feedback block using $dvsNav1$ and $dvsNav2$, and retrospectively by FLIRT.

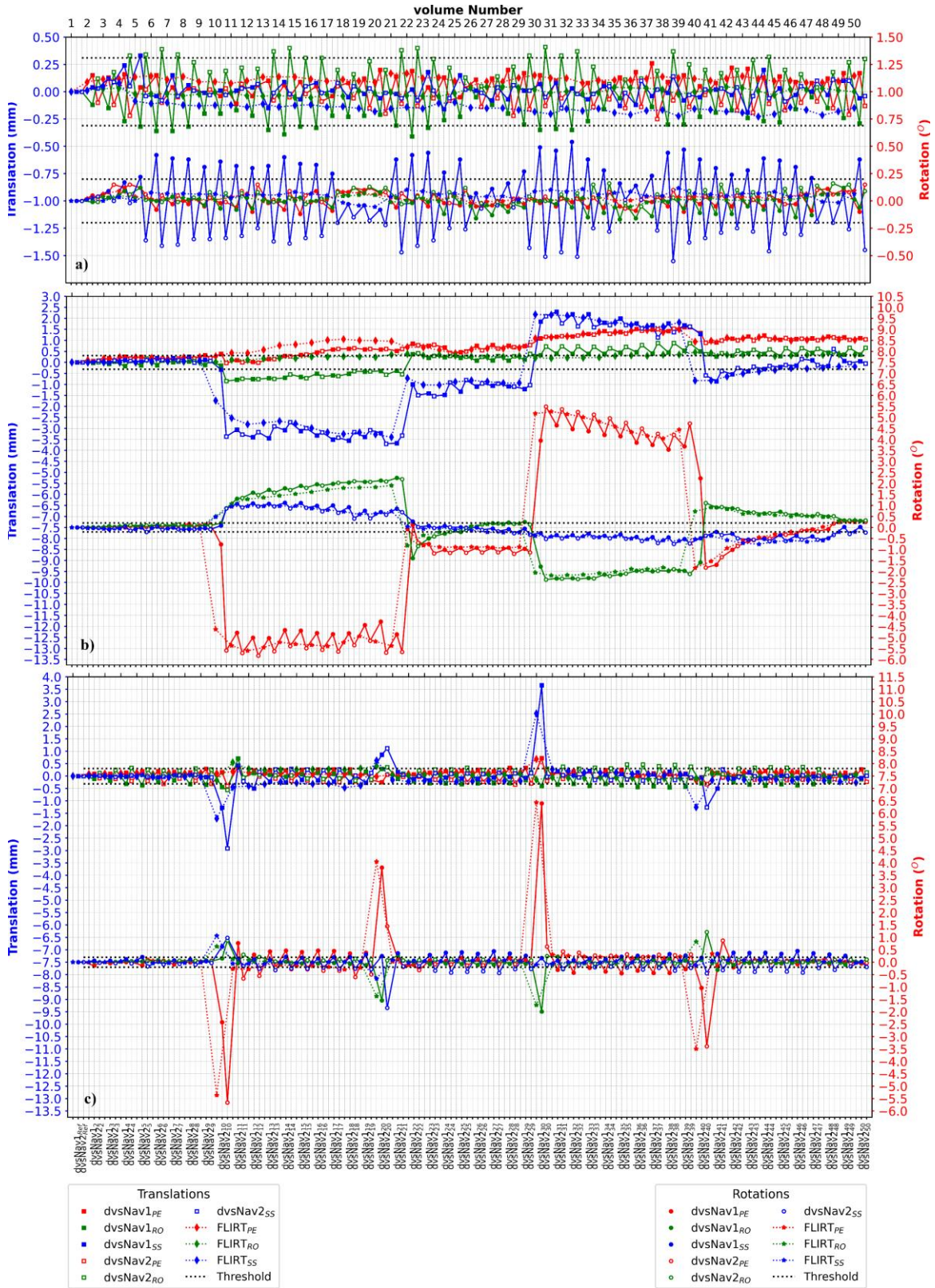

Figure 4-9 Plots showing for one volunteer the prospective dvsNav1 and dvsNav2, and retrospective FLIRT estimates of head position in the imaging FOV during each volume acquisition relative to its position during the 1st acquisition (a) without intentional motion, (b) with intentional motion around volumes 10, 21, 29 and 40 but without feedback to the sequence, and (c) intentional motion around volumes 10, 19, 29 and 40 with active feedback to the sequence. The horizontal dotted lines show thresholds for through-plane translation (i.e., 10% slice thickness) and rotation (i.e., 0.2⁰). Since the

images were acquired in the sagittal orientation, the slice-select is from left to right direction and phase encoding is from anterior to posterior.

Figure 4-9 a) shows 'pulsating' motion detected by the feedback block during acquisitions without intentional motion, which were hardly detected by FLIRT. Figure 4-9 b) shows motion estimated by the feedback block using $dvsNav1$ and $dvsNav2$, but without sending the motion parameters to the sequence for prospective correction, and by FLIRT. Figure 4-9 c) shows that the head position approaches its original position within the imaging FOV after the motion parameters were sent to the sequence. Moreover, motion estimates from multiple self-navigators may be needed to correct the FOV if the motion continues longer than the time required to acquire the partitions of a single volumetric self-navigator.

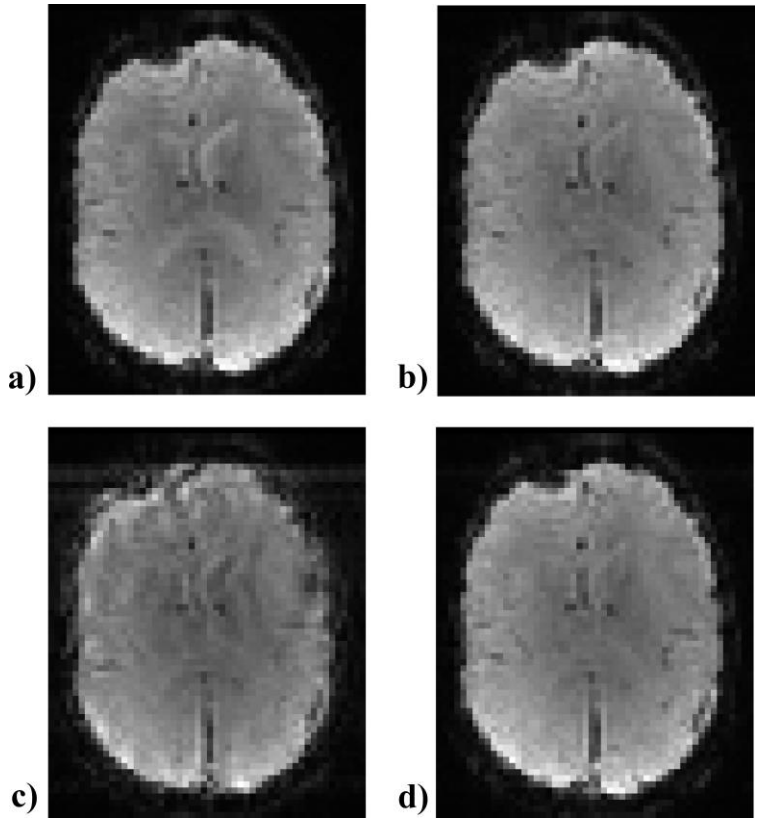

Figure 4-10 Images of an axial slice from the dvsNav 3D-EPI acquisition with intentional head motion and prospective motion correction applied (MoCo). The images show the same slice for: a) the 1st (reference) volume, b) the 8th volume (before motion occurred), c) the 10th volume (during motion), and d) the 11th volume (after motion occurred). The acquisition orientation was sagittal with the slice-select from left to right and phase encoding from anterior to posterior.

Figure 4-10 shows images of the 27th axial slice from a *dvsNav* 3D-EPI acquisition with intentional motion and feedback active for a) the 1st volume, b) the 8th volume, which is immediately before motion occurred, c) the 10th volume, which is acquired during the motion,

and d) from the 11th volume, which is immediately after motion occurred. Notably, image quality is degraded in the volume during which motion occurred (Figure 4-10 c), despite PMC.

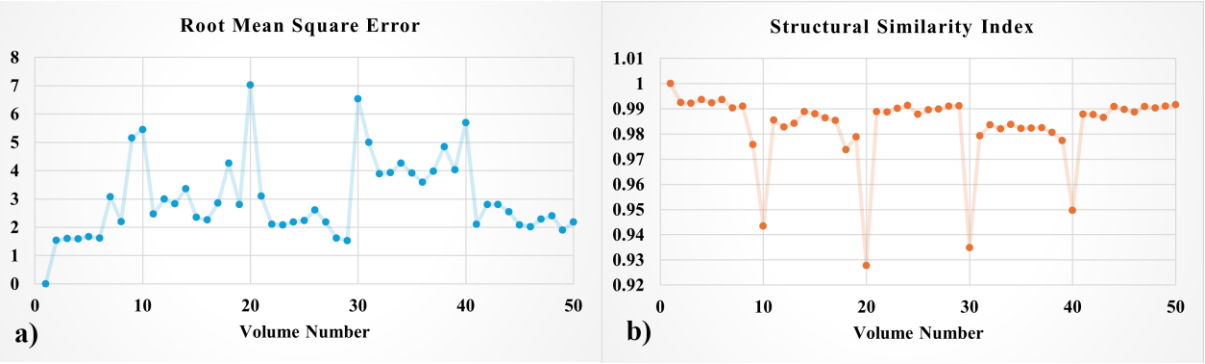

Figure 4-11 a) Root mean square errors (RMSE) and b) structural similarity indices (SSI) obtained when comparing the 27th axial slice of each volume to the same slice of the reference volume. Images were from the dvsNav 3D-EPI MoCo acquisition in participant #2.

Figure 4-11 shows how 'similar' a single slice from each volume in a time series acquired with PMC active is to the same slice of the reference volume. As expected, root mean square errors and structural similarity indices (SSIs) are higher and lower, respectively, during (or immediately after) the volume where motion occurred. In this acquisition, the participant moved around volumes 10, 19, 29 and 40. In volumes around the motion events, SSIs range from 92-95%; following motion events, SSIs typically return to values of 98% or higher.

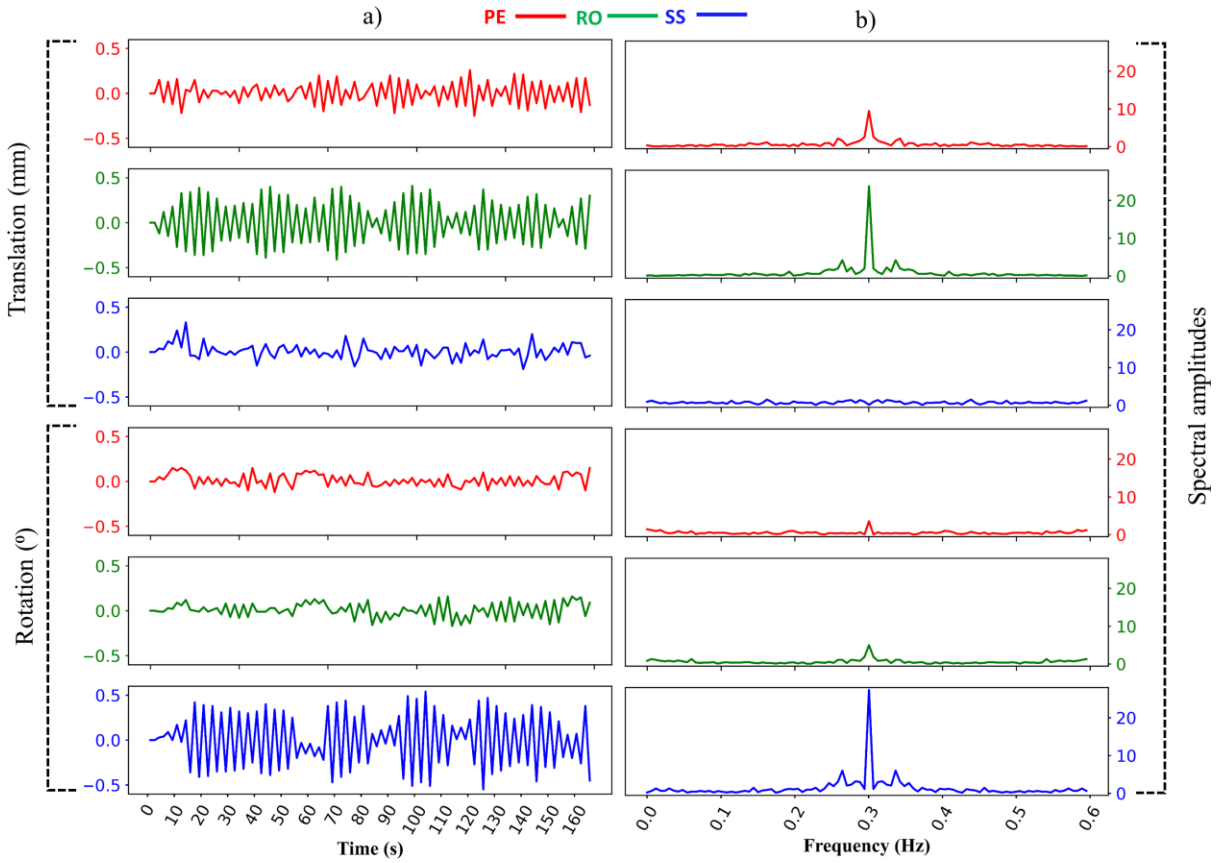

Figure 4-12 The six components of dvsNavs' motion estimations during 3D EPI acquisition without motion in a) time and b) frequency domain.

Plots of motion parameters estimated by *dvsNavs* during an in vivo 3D EPI acquisition with no motion are shown in column a) whereas their corresponding frequency spectrum are shown in corresponding rows of column b) of Figure 4-12. Pulsating motion parameters, which were not observed in any of phantom acquisitions, were detected in all of the in vivo 3D EPI acquisitions without motion. In all in vivo 3D EPI acquisitions without motion, the translational motion parameters in phase-encoding and readout components were consistently pulsating. However, in subject 1 it was the rotational (see Figure 4-12 a) and in subject 2 it was translational (not shown) motion parameters in the slice-select direction that were pulsating.

4.4. Discussion

This work demonstrates that the modified feedback block implemented in the IRP of the 3D EPI sequence can use two successive subsets of partitions to compute and correct motion with submillimeter accuracy twice during each volume acquisition.

The feedback block constructs two volumetric self-navigators from two separate subsets of the partitions being accumulated as part of the volume acquisition. Therefore, the new technique requires no additional RF pulses, no additional gradient pulses, and no measurement

interruptions, however, it is limited to 3D acquisitions. This is because image reconstruction in 3D acquisition does not start until all the partitions have been acquired, allowing the feedback block to accumulate two subsets of partitions, construct two navigators, estimate motion twice and send the estimated motion parameters to the sequence to correct the FOV before the Online block of the IRP constructs the main volume image. In the current configuration, which employs a center-out acquisition scheme, the first self-navigator of volume i, $dvsNav1_i$, is constructed from the 8 central partitions with remaining partitions zero filled; this is equivalent to lowpass filtering (or smoothing) in the partition direction. The second self-navigator of volume i, $dvsNav2_i$, is constructed from 20 consecutively-acquired later partitions with missing partitions zero filled. Zero filling ensures that the resolution of $dvsNav1_i$ and $dvsNav2_i$ are the same as that of the image volume. We used a flip angle equal to the Ernst angle (16º) to optimize the BOLD contrast at 3T. The current implementation did not employ any compression, which may allow the temporal resolution of motion tracking to be increased.

The feedback block requires time to accumulate partitions to the navigator volumes, as well as time to construct the image volumes, register these to the reference volumes, and send the motion parameters to the sequence. It has been shown previously (Bayih et al., 2022) that the computation time depends, in part, on the number of receiver channels in the head coil and the partition repetition time (TR). Based on the trade-off between computation time (Table 4-1) and motion estimation accuracy (Figure 4-3), the feedback block was configured to accumulate partitions from a maximum of 20 channels of the head coil. Therefore, in this work, both the phantom and in vivo scans were performed with a 20-channel head/neck coil and a 64 ms TR. In both experiments, the FOV was updated twice during each volume acquisition; updates occurred 11 partitions (0.704 s) after all required partitions had been accumulated to the feedback block. As a result, the first batch of motion parameters (estimated using $dvsNav1_i$) update the FOV after acquisition of 19 partitions, permitting a maximum of 33 partitions of the current volume to be acquired with the corrected FOV. The second batch of motion parameters (estimated using $dvsNav2_i$) update the FOV after the acquisition of 51 partitions; the last partition of the current volume and the first 19 partitions of the next volume are therefore acquired with the newly updated FOV. Hence, our feedback block was capable of providing position updates to the sequence twice during the acquisition of a 52-partition volume.

As shown in Figure 4-5, the phantom (Figure 4-4) comprising 5 plates, 57 fiducial spheres and 2 wedges provided sufficient features for both $dvsNav1$ and $dvsNav2$. The motion parameter plots (Figure 4-6) and absence of apparent features in the absolute difference images

of the central slices of the phantom (Figure 4-7) before and after motion confirm that the position of the phantom approaches its original position within the imaging FOV in the volumes following the one(s) during which motion occurred. The through-plane motion estimates of $dvsNav1$ and $dvsNav2$ appeared to fluctuate slightly (in μm) in the phantom data acquired without motion (Figure 4-6 a)). This is likely due to the difference in the number of partitions accumulated and zero-fillings performed to construct $dvsNav1$ and $dvsNav2$. To avoid unstable fluctuations, through-plane motion estimates less than 10% of the slice thickness or rotations in any direction less 0.2º were not sent back to the sequence for correction. Slight differences in the $dvsNav1$ and $dvsNav2$ estimates are therefore not unexpected. Rapid motions (i.e., motions that did not spill into the next navigator) were accurately corrected by the sequence, as illustrated by $dvsNav2_7$ and $dvsNav1_8$, and again by $dvsNav19_1$ and $dvsNav19_2$ in Figure 4-6 b). This was also true when the motion spanned across two self-navigator acquisitions, as can be seen from $dvsNav1_{13}$ and $dvsNav2_{13}$ or $dvsNav2_{25}$ and $dvsNav1_{26}$ (see Figure 4-6 b).

As can be seen in Figure 4-8, the images of the 1st *dvsNav* appear low-pass filtered due to zero filling of all except the central 8 partitions. In contrast, those of *dvsNav*2 appear high-pass filtered due to zero filling of the central 20 partitions containing the bulk of the signal. Notably, despite the absence of the center partitions, the *dvsNav*2 images demonstrate sufficient features for accurate co-registration and real-time motion tracking.

The in vivo data shown in Figure 4-9 demonstrate that motion estimated by the $dvsNavs$ and FLIRT are largely similar, except in the volumes during which the motion occurred. Figures 4-10 and 4-11 show that the image quality and structural similarity indices compared to the reference volume of images acquired after motion events are largely recovered. However, prospective motion correction could not fully recover image quality in volumes during which bulk motion occurred (Figure 4-10 c) and Figure 4-11).

Notably, even in the absence of intentional motion (Figure 4-9 a), the feedback block detected pulsating motion with a frequency around 0.25Hz (see Figure 4-12). Since no such pulsating motion was detected by the self-navigators during phantom acquisitions, nor by FLIRT in phantom or in vivo acquisitions, this may be due to breathing, which may affect $dvsNav1$ and $dvsNav2$ images differently. Since the pulsating motions are modulated by the bulk motions, their effect will likely depend on the magnitude and direction of the bulk motion (see Figure 4-9 b). The current configuration of the double volumetric self-navigated 3D EPI sequence uses two distinct subsets of partitions to detect motion during volume acquisition

which makes it inefficient to correct continuously induced pulsating motions; to date, there is no prospective motion correction technique capable of efficiently correcting continuously induced motions. Whenever bulk motion occurs during in vivo acquisitions, the proposed sequence readjusts its FOV to minimize the pose change in the imaging FOV, which predominantly compensates for the bulk motion. However, depending on the bulk motion, the correction may over correct the pose change because of the residual pulsating motions as seen in Figure 4-9 c). Additional work is needed to confirm the origin of the observed pulsating motion.

In the current configuration of the sequence, 24 of 52 partitions are not used for motion detection. Very fast motion during these feedback block computation times may remain undetected and affect volume images differently. For instance, motion during the 12 partitions of the 1st computation period will result in more image degradation than motion during the second computation block.

4.5. Conclusion

The current study demonstrates that real-time motion detection and correction can be performed twice per volume during repeated 3D EPI volume acquisitions using double volumetric self-navigators constructed from two subsets of each volume's partitions. By co-registering each $dvsNav$ to its corresponding volume constructed during the first volume acquisition, head pose changes in the imaging FOV relative to the first navigator volume can be estimated. Motion estimates are sent to the sequence to readjust the imaging FOV accordingly and acquires the remaining partitions of that volume and/or the first partitions of the next volume, with the corrected FOV. The proposed technique eliminates the need for extra hardware or additional sequence pulses to track subject motion. Moreover, our observation during in vivo acquisitions of pseudo-periodic fluctuations in the motion estimates, suggest that the technique may be able to detect pulsating physiological motions. The temporal resolution is limited to detecting and correcting motion twice per volume due to the number of partitions required to construct $dvsNav$s with sufficient features for motion estimation, as well as the time required for co-registration and feedback. Further work is required either to determine the detection and accuracy of physiological motions or to reduce the sensitivity of the technique to physiological pulsations. To reduce the IRP's sensitivity to physiological noise, the feedback block can be reconfigured to skip partitions further removed from the center partition and use more central partitions in self-navigator construction. Implementing real-time

shimming and parallel imaging in the partition direction would further improve image quality and accelerate volume acquisition, respectively.

Chapter Five

5. Discussion

5.1. Self-navigated PMC ($snPMC$)

In this work, we demonstrated the efficacy of a new prospective motion correction (PMC) technique for 3D-EPI fMRI that utilizes a subset (or subsets) of the partitions being acquired to construct one (or more) low-resolution volume images, called a volumetric self-navigator(s) ($vSNav$), to detect and correct motion while the remaining partitions of the volume are still being acquired. Since the proposed PMC technique uses only the data that are being acquired by the sequence anyway to track subject motion in real time, it is referred to as a self-navigated prospective motion correction ($snPMC$) technique. $snPMC$ does not require additional hardware or radio frequency (RF) and gradient pulses to track subject motion, therefore eliminating the extra steps and time usually required to track subject motion in real time, such as acquiring and/or setting up a tracking module in the parent sequence, calibrating acquisition axes, etc. (Ooi et al., 2009; Todd et al., 2015; Van Der Kouwe et al., 2006). Theoretically, $snPMC$ can be implemented in any 3D sequence because of their image reconstruction timing. In this work, 3D-EPI was used because EPI is widely used for functional MR data acquisitions and it is highly susceptible to motion artifacts (Bernstein et al., 2004; Chen & Glover, 2015; Norris, 2006; Stehling et al., 1991).

The temporal resolution of $snPMC$ can be increased by constructing more navigators from fewer partitions. However, this requires that more partitions are zero filled to match the image resolution of the acquisition. Since zero filling results in spatial smoothing along the partition direction, the locations of these zero-filled partitions may result in loss of critical features, which will reduce the accuracy of co-registration and motion detection. At worst, the navigators may have insufficient features for motion detection. Therefore, implementing $snPMC$ requires a trade-off between motion detection accuracy and the temporal resolution of motion correction. This problem could potentially be addressed by re-acquiring the 3 center partitions with each partition subset (i.e., partition numbers 25 to 27 in the current implementation), which would result in the main volume features being preserved in each $vSNav$ but a minimal increase in acquisition time.

5.2. Implementation of $snPMC$ in 3D-EPI

In our first implementation of $snPMC$ (Bayih et al., 2022), we detected and corrected subject motion once per volume in real time by accumulating the 1st 24 partitions (partition#14 to partition#37) of a 52-partition volume. After filling the remaining 28 partitions (partition#0 to partition#13 and partition#38 to partition#51) with zeroes, a volumetric self-navigator ($vSNav$) was constructed; the navigator volume constructed during the 1st volume was defined as the reference volumetric self-navigator ($vSNav_{Ref}$). Motion was estimated by co-registering each $vSNav$ to the $vSNav_{Ref}$ and sending motion parameters back to the 3D-EPI sequence; motion estimates were received after acquisition of a further 12 partitions. The remaining partitions of the current volume (i.e., the last 16 partitions in our implementation), as well as the first 36 partitions of the next volume (until the next motion estimates are received), were then acquired with the adjusted field of view (FOV) (see Figure 2-3). The performance of our $vSNav$ 3D-EPI sequence in detecting and correcting motion in real time was validated both in a phantom and in vivo. Moreover, we compared the performance of our $vSNav$ 3D-EPI sequence to a 2D-EPI sequence with standard PACE (**P**rospective **A**cquisition **C**orre**E**ction; (Thesen et al., 2000)) PMC for localizing brain activations during a simple finger tapping fMRI experiment, both in the absence and presence of intentional head motions. Overall, our results demonstrated that our $vSNav$ 3D-EPI sequence is able to acquire task-related BOLD signal changes with comparable or better quality than 2D-EPI with PACE PMC, without the need for any additional hardware or RF and gradient pulses.

The timing and accuracy of motion detection, which determines the timing and accuracy of motion correction, depends on the number and position of the partitions used to construct the $vSNav$. For instance, constructing the $vSNav$ from all the partitions of a volume will result in the most accurate possible motion estimate but pushes the temporal resolution of motion detection and correction beyond the current volume acquisition period. On the other hand, constructing a $vSNav$ from fewer partitions results in less accurate motion estimation but increases the temporal resolution of motion detection so that FOV adjustments can be applied within the current volume acquisition period. Any subset of partitions can be used to implement $snPMC$, as long as the subset of partitions used to construct the $vSNav$ contains enough features for accurate co-registration to the reference, and enough time is left for the acquisition FOV to be adjusted before commencing the acquisition of partitions for the next $vSNav$. Given the flexibility of motion detection and correction timings, prospective motion gating may be possible (Cassidy et al., 2004; Kinchesh et al., 2018; Rasmus M. Birn, J. Bodurka, 2001).

5.3. The $dvsNav$ 3D-EPI implementation of $snPMC$

The temporal resolution of motion detection and correction in our $vSNav$ 3D-EPI sequence was doubled by sequentially accumulating two subsets of partitions (1st subset: partition#22 to partition#29; 2nd subset: partition#6 to partition#15 and partition#36 to partition#45) during the center-out acquisition of partitions to construct a volume. Using these subsets of partitions, and zero filling missing partitions, we constructed two volumetric self-navigators, called double volumetric self-navigators ($dvsNav1$ and $dvsNav2$); the two self-navigators constructed during the acquisition of the 1st volume were defined as the reference double volumetric self-navigators ($dvsNav1_{Ref}$ and $dvsNav2_{Ref}$). As with the implementation of the single self-navigator, motion estimates were computed by co-registering each $dvsNav$ to its reference volume. As soon as they became available, motion estimates were sent back to the 3D-EPI sequence so that the FOV could be updated before acquisition of the next partitions (see Figure 4-2). In our implementation, the 1st FOV adjustment occurred after acquisition of 20 partitions, and the second at the end of the current volume acquisition (after partition 52). Our phantom and in vivo results demonstrated that our $dvsNav$ 3D-EPI sequence could successfully compute and correct bulk motion to sub-millimeter accuracy twice during each volume acquisition (see Figure 4-6 and Figure 4-7). However, during in vivo testing, there was evidence of continuous pulsating motion, likely due to physiological noise, which the sequence was not able to correct (Figure 4-9c).

The $dvsNavs$ achieved twice the temporal resolution of traditional image registration (see Figure 4-9c), which may be important for accurate motion correction. The $dvsNav1$ is constructed from a subset of partitions that contains the center partition, and it is low-pass filtered in the partition direction, whereas $dvsNav2$ is constructed from a subset of partitions that contains no center partition and it is band-pass filtered in the partition direction. Notably, the *dvsNavs* detected continuously pulsating motion in the in vivo acquisitions, which may have physiological origins. Further work is needed to confirm the origins of these pulsating motions and to confirm that these are not artifacts related to bias in the motion estimates computed by the two self-navigators, which have very different image features. When using the $dvsNav$ 3D-EPI sequence for fMRI scanning, it may be necessary to include a continuously pulsating motion model in the analysis to account for this signal (Jones et al., 2008; Kassinopoulos & Mitsis, 2021). Such a model can be defined based on the continuously pulsating residual motions detected by the $dvsNavs$.

5.4. The imaging parameters

In the current work, which aimed to implement $snPMC$ for 3D-EPI fMRI applications, both our $vSNav$ and $dvsNav$ 3D-EPI sequences were validated using imaging parameters appropriate for 3D-EPI fMRI. Any implementation of $snPMC$ using a different 3D sequence would necessarily have different imaging parameters and require validation.

5.5. Validation limitations and recommendations

The motion correction performance of the $vSNav$ 3D-EPI sequence was validated in a phantom by manually inducing brief motions during the acquisition of volumes 4, 13 and 24 to 25 (see Figure 2-6). The performance of the $dvsNav$ 3D-EPI was similarly validated by manually inducing brief motions during the accumulation of partitions for $dvsNav2$ in volume 7 and partitions for $dvsNav1$ in volume 19, and extended motions during the accumulation of $dvsNav1$ and $dvsNav2$ partitions of volume 13, and $dvsNav2$ and *dvsNav1* partitions of volumes 26 and 27, respectively (see Figure 4-6). However, in the present work, the exact amount and timing of motions were not known. The use of a motion rig would have been advantageous as it provides a ground truth against which to compare motion estimates.

For in vivo scanning, motion correction performance of both the $vSNav$ and $dvsNav$ 3D-EPI sequences were validated using direct head motions induced when subjects moved their head from centre to side and from side to centre (see Chapter Two). The head motions were loosely controlled by marking three dots on the surface of the scanner bore – one dot directly in line with the subject's line-of-sight (centre mark), one dot approximately 8 cm to the left of the centre mark, and another approximately 8 cm to the right of the centre mark. While the three dots helped to control the direction and magnitude of the motions, so they did not exceed the PACE thresholds (i.e. translation <20 mm and rotation <8^{o}), the exact magnitude and timing of the induced motions were not known. Therefore, FLIRT was used to determine the translational and rotational components of the induced motions for comparison with motion estimates determined prospectively using the self-navigator(s). Although the head motions of all subjects typically extended beyond the period required to accumulate the partitions for the self-navigators, the sequences were able to successfully track and correct head motions.

The effectiveness of our $vSNav$ 3D-EPI sequence in acquiring motion-robust fMRI data was assessed in four subjects who were requested to induce indirect and/or direct head motions during scanning (as described in Chapter Three). We did not expect the indirect head motions induced when subjects opened and closed their legs during fMRI scanning to be comparable to involuntary head motions induced by swallowing, deep breathing, yawning, sneezing, etc.. The ability of our self-navigated sequences to correct for such motions was not assessed. Moreover,

the magnitude of direct head motions was only controlled to ensure that they did not exceed the PACE limits for translation and rotation. The latency, which is the time between an instruction cue and the start of the subject's motion, and the duration of the subject's action for each instruction were also not measured. Considering these factors would improve future experiments that aim to validate the effectiveness of the $vSNav$ 3D-EPI sequence in acquiring motion-robust fMRI data.

In our self-navigated sequences, except for the first volume, every subsequent fMRI volume is comprised of partitions acquired with either two (in the case of the $vSNav$) or three (for $dvsNavs$) different FOVs. While the current work used an adaptation of widely used 2D fMRI pre-processing pipelines, further work is required to optimize the pre-processing pipeline for 3D data. Moreover, any fMRI acquisition with a differently configured $vSNav$ 3D-EPI sequence will require a differently adapted pre-processing pipeline. Further validation of the performance of our $vSNav$ 3D-EPI sequence for motion-robust fMRI data acquisition is required in more subjects, for different types of indirect head motion (deep breathing, swallowing, coughing, etc.), and for different head motion directions (pitch, yaw and roll), magnitudes (small vs large), and durations (slow vs fast).

5.5.1. Future work on $vSNav$ 3D-EPI implementation of $snPMC$

Under the current configuration, 12 partitions (i.e. partition numbers 38–43 and 8–13) are acquired by the $vSNav$ 3D-EPI sequence while the $vSNav$ is being reconstructed and the motion estimates are computed. However, these partitions contain a more significant portion of the total signal than the final 16 partitions (i.e. partition numbers 0–13 and 38–51) that are acquired after the FOV has been updated (see Figure 2-3). These 'uncorrected' 12 partitions degrade the quality of the volumetric data more than would have been the case if instead the last 12 partitions in the center-out acquisition scheme, which contain less signal, had not been corrected. Therefore, future work could minimize such image quality degradation by reconfiguring the center-out acquisition order to, after acquiring the first 24 partitions, instead acquire the last 6 partitions on either side of the center partition (i.e., partition numbers 0–5 and 46–51) and then acquire the middle 16 partitions (i.e. partition numbers 6–13 and 38–45) after the FOV has been updated (see Figure 5-1). However, any such re-ordering will require that the pre-processing pipeline be adjusted accordingly to ensure accurate slice timing correction.

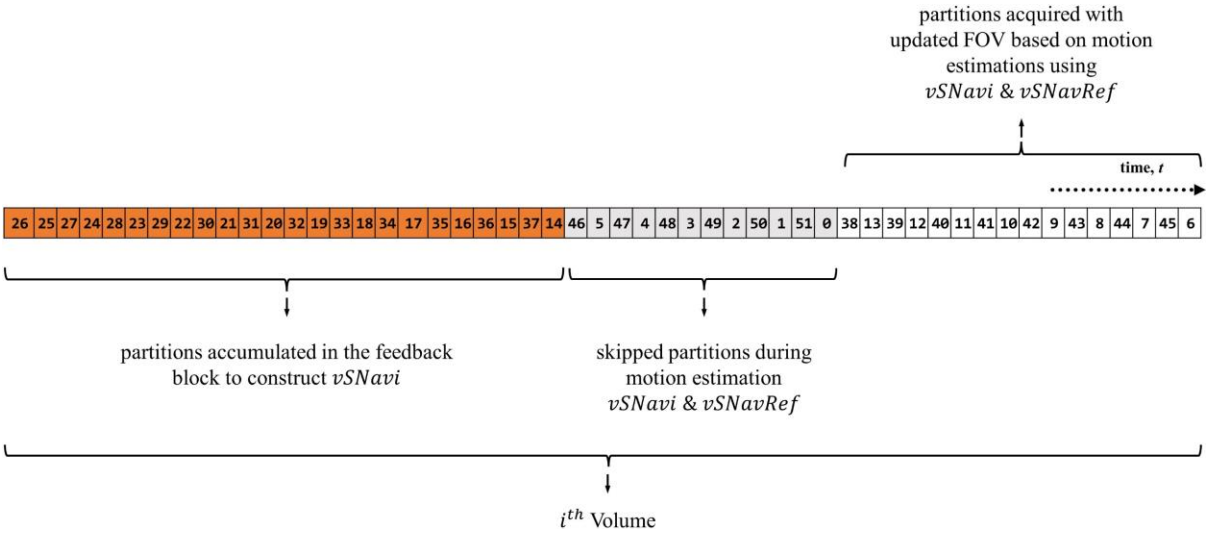

Figure 5-1 The reconfigured vSNav 3D-EPI partition acquisition order which ensures that the 12 partitions with the least amount of signal (i.e. the 6 partitions on either side that are the furthest from the center partition) are acquired with the 'uncorrected' FOV.

5.5.2. Future work on $dvsNav$ 3D-EPI implementation of $snPMC$

The ever-present continuously pulsating (physiological) motions and inherent differences between the $dvsNav1$ and $dvsNav2$ (see Figure 4-2) limited the accuracy of motion correction during in vivo scanning with our $dvsNav$ 3D-EPI sequence. However, due to the different distortions induced by continuous motion in $dvsNav1$ and $dvsNav2$, these $dvNavs$ also provide an opportunity to detect and measure such continuously pulsating (physiological) motions. Therefore, future implementations of $snPMC$ using our $dvsNav$ 3D-EPI sequence should consider whether the primary aim is to detect the continuously pulsating motions or to perform real-time motion correction.

As with the $vSNav$ 3D-EPI, the accuracy of motion tracking and correction could potentially be improved, and the effect of "uncorrected" partitions on our volumetric data minimized, by ensuring that partitions containing the most signal are used to construct the self-navigators, while those with the least signal are acquired during self-navigator reconstruction and motion computation times. For example, modifying the center-out partition acquisition order as shown in Figure 5-2 would ensure that only the 12 partitions furthest removed on either side from the center partition, which are also those with the least signal, are "skipped" – i.e., these partitions are not used to compute motion estimates and are not acquired with the updated FOV. According to this scheme, partition numbers 6–11 and 40–45 would be acquired before the FOV is updated the first time using motion estimates computed from $dvsNav1$, and partition numbers 0–5 and 46–51 before the FOV is updated a second time using motion

estimates computed from $dvsNav2$. Also, the *dvsNav2* constructed from partition numbers 12–21 and 30–39 according to this scheme would have substantially more signal than that constructed using partition numbers 6–15 and 36–45 in the current implementation of our $dvsNav$ 3D-EPI sequence. Using the same principle, various combinations of accumulated and skipped partitions can be tested to optimize both the accuracy and temporal resolution of motion tracking. Re-acquiring one or three of the centre partition(s) for *dvsNav2* would also substantially increase the signal of the second self-navigator and improve the accuracy of motion tracking. This could also potentially reduce the number of partitions required for accurate motion estimation by the second self-navigator and provide space for a 3rd self-navigator (with the centre partitions re-acquired) in the sequence, thereby increasing the temporal resolution of motion estimation. However, as mentioned previously, reconfiguring the partition acquisition scheme would require that the pre-processing pipeline be adapted accordingly.

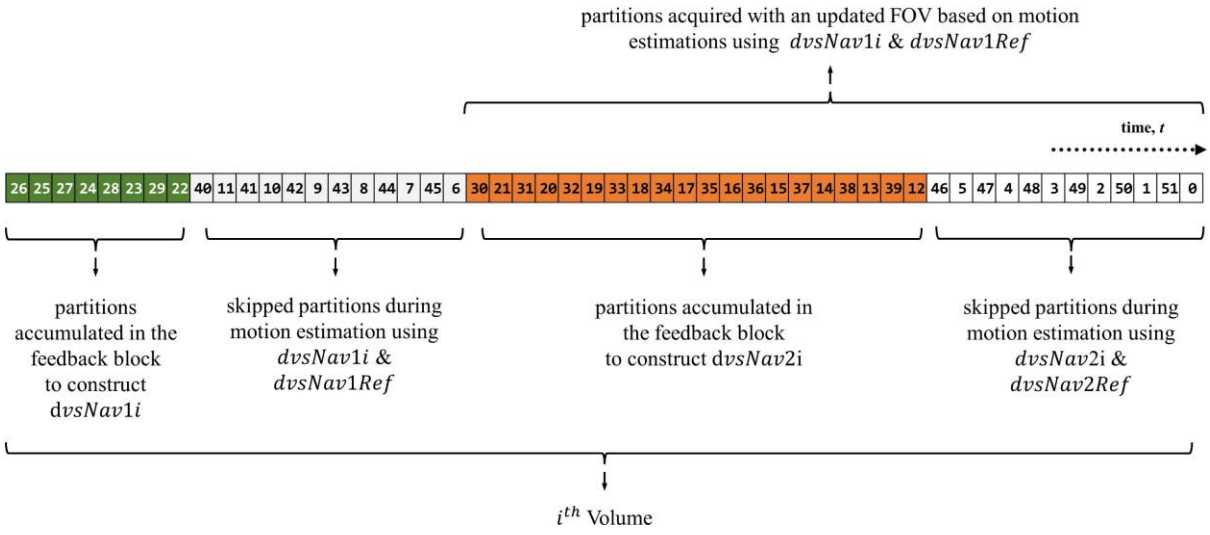

Figure 5-2 The reconfigured $dvsNav$ 3D-EPI partition acquisition order which ensures that 24 partitions with the least amount of signal (i.e. the 12 partitions furthest removed on either side from the centre partition) are not used for motion estimation and are the ones acquired with the "uncorrected" FOV, thereby minimizing signal degradation.

Chapter Six

6. Conclusion

In this work, a novel self-navigated prospective motion correction ($snPMC$) technique for 3D-EPI fMRI was proposed and implemented. This technique does not require additional hardware or radio frequency (RF) and gradient pulses inserted into the scanning sequence to detect subject motion in real time. The $snPMC$ is based on the idea that a subset of the partitions that are used to create a complete 3D volume can be used to create a spatially smoothed volumetric image. Since this smoothed image will have the same general features as the complete volume, it can be used to detect motion and correct the field of view (FOV) while the remaining partitions are still being acquired. Therefore, the proposed s$nPMC$ technique accumulates a subset of the partitions being acquired to a separate storage location, constructs a volumetric self-navigator from this subset of partitions, registers it to a reference volumetric self-navigator (constructed during the acquisition of the first volume), and sends the motion parameters to the sequence so that the imaging FOV can be updated before any remaining partitions are acquired.

In our first implementation of $snPMC$, we tracked and corrected for subject motion once per volume by registering each volumetric self-navigator ($vSNav$) to a reference $vSNav$ ($vSNav_{Ref}$) that was constructed during the first volume acquisition. The estimated motion parameters were sent to the sequence, and the sequence updated its imaging FOV, once per volume. The motion correction performance of our $vSNav$ 3D-EPI sequence was validated both in a phantom and in vivo. In the absence of motion, both phantom and in vivo data demonstrated stable motion estimates. For phantom acquisitions with intentional motion, estimated residual motion after motion correction were within acceptable thresholds (i.e., < 10% of the slice thickness and < 0.2º rotation). For in vivo acquisitions, motion estimates using $vSNav$ and FLIRT agreed to within 0.23 mm (< 10% of the slice thickness) and 0.14º in all directions.

fMRI data acquired using our $vSNav$ 3D-EPI sequence were compared to data acquired using 2D-EPI with Siemens' standard prospective acquisition correction (PACE) scheme. It was found that the 3D data yielded more brain voxels with a higher temporal signal-to-noise ratio (tSNR) and blood oxygenation level dependent (BOLD) signal changes compared to 2D data. However, spatial filtering increased the number of brain voxels with higher tSNR and BOLD signal changes in the 2D data more than in the 3D data. Despite this, both spatially

smoothed 2D and 3D data resulted in similar activation maps, with the 3D data having fewer false activations. To fully utilize the superior quality of the 3D BOLD signal, an optimized pre-processing pipeline for 3D-EPI data needs to be developed.

Finally, the temporal resolution of $snPMC$ was doubled by implementing double volumetric self-navigators ($dvsNav$s) in our 3D-EPI sequence. The sequence adjusts its imaging FOV twice per volume using motion parameters estimated through registering either the first ($dvsNav1$) or second ($dvsNav2$) of the double volumetric self-navigators to their respective references (i.e., $dvsNav1_{Ref}$ or $dvsNav2_{Ref}$). Both reference self-navigators are acquired and constructed during the first volume acquisition. Subsequent partitions, including those used to construct the next volumetric self-navigator, are then acquired with the updated FOV. The motion correction performance of the $dvsNav$ 3D-EPI sequence was validated using both phantom and in vivo data. Motion estimates during in vivo scans were compared to retrospective estimates obtained from FLIRT. The phantom data showed successful motion detection and correction, accurately identifying and correcting induced motions before accumulation of the partitions for the next $dvsNav$. However, the in vivo data showed residual motions above the acceptable thresholds (>10% of slice thickness or >0.2º) and between motion estimates from the $dvsNav$s and FLIRT. We posit that these continuously pulsating motions are likely physiological noise artifacts. However, the continuously pulsating motions detected by the $dvsNav$s could be important inputs for modelling continuous motions that may confound fMRI data. Future work should explore the continuous motion detection performance of different configurations of the $dvsNav$ 3D-EPI sequence.

Overall, an implementation of $snPMC$ in 3D-EPI has been presented that can detect and correct subject motion in real time, once or twice per volume, without the need for additional hardware or RF and gradient pulses. The $vSNav$ 3D-EPI implementation of $snPMC$ was shown to provide accurate and good quality fMRI data.

References

Afacan, O., Hoge, W. S., Janoos, F., Brooks, D. H., & Morocz, I. A. (2012). Rapid full-brain fMRI with an accelerated multi shot 3D EPI sequence using both UNFOLD and GRAPPA. *Magnetic Resonance in Medicine*, *67*(5), 1266–1274. https://doi.org/10.1002/mrm.23106

Aksoy, M., Forman, C., Straka, M., Çukur, T., Hornegger, J., & Bammer, R. (2012). Hybrid prospective and retrospective head motion correction to mitigate cross-calibration errors. *Magnetic Resonance in Medicine*, *67*(5), 1237–1251. https://doi.org/10.1002/mrm.23101

Alahmadi, A. A. S. (2021). Effects of different smoothing on global and regional resting functional connectivity. *Neuroradiology*, *63*(1), 99–109. https://doi.org/10.1007/s00234-020-02523-8

Alhamud, A., Taylor, P. A., van der Kouwe, A. J. W., & Meintjes, E. M. (2016). Real-time measurement and correction of both B0 changes and subject motion in diffusion tensor imaging using a double volumetric navigated (DvNav) sequence. *NeuroImage*, *126*, 60–71. https://doi.org/10.1016/j.neuroimage.2015.11.022

Alhamud, A., Tisdall, M. D., Hess, A. T., Hasan, K. M., Meintjes, E. M., & Van Der Kouwe, A. J. W. (2012). Volumetric navigators for real-time motion correction in diffusion tensor imaging. *Magnetic Resonance in Medicine*, *68*(4), 1097–1108. https://doi.org/10.1002/mrm.23314

Altman, N. R., & Bernal, B. (2015). Pediatric applications of functional magnetic resonance imaging. *Pediatric Radiology*, *45*, 382–396. https://doi.org/10.1007/s00247-015-3365-1

Amaro, E., & Barker, G. J. (2006). Study design in fMRI: Basic principles. *Brain and Cognition*, *60*(3), 220–232. https://doi.org/10.1016/j.bandc.2005.11.009

Andropoulos, D. B., & Greene, M. F. (2017). Anesthesia and Developing Brains — Implications of the FDA Warning. *New England Journal of Medicine*, *376*(10), 905–907. https://doi.org/10.1056/NEJMp1700196

Armanious, K., Gatidis, S., Nikolaou, K., Yang, B., & Thomas, K. (2020). RETROSPECTIVE CORRECTION OF RIGID AND NON-RIGID MR MOTION ARTIFACTS USING GANS University of Stuttgart , Institute of Signal Processing and System Theory , Stuttgart , Germany University of T ¨ ubingen , Department of Radiology , T ¨ King ' s College Lond. *IEEE 17th International Symposium on Biomedical Imaging (ISBI)*, *Isbi*, 1550–1554.

Armanious, K., Jiang, C., Fischer, M., Küstner, T., Hepp, T., Nikolaou, K., Gatidis, S., & Yang, B. (2020). MedGAN: Medical image translation using GANs. *Computerized Medical Imaging and Graphics*, *79*. https://doi.org/10.1016/j.compmedimag.2019.101684

Bandettini, P. A., Jesmanowicz, A., Wong, E. C., & Hyde, J. S. (1993). Processing strategies for time-course data sets in functional mri of the human brain. *Magnetic Resonance in Medicine*, *30*(2), 161–173. https://doi.org/10.1002/mrm.1910300204

Batchelor, P. G., Atkinson, D., Irarrazaval, P., Hill, D. L. G., Hajnal, J., & Larkman, D. (2005). Matrix description of general motion correction applied to multishot images. *Magnetic Resonance in Medicine*, *54*(5), 1273–1280. https://doi.org/10.1002/mrm.20656

Bayih, S. G., Jankiewicz, M., Alhamud, A., van der Kouwe, A. J. W., & Meintjes, E. M. (2022). Self-navigated prospective motion correction for 3D-EPI acquisition. *Magnetic Resonance in Medicine*, *88*(1), 211–223. https://doi.org/10.1002/mrm.29202

Behzadi, Y., Restom, K., Liau, J., & Liu, T. T. (2007). A component based noise correction method (CompCor) for BOLD and perfusion based fMRI. *NeuroImage*, *37*(1), 90–101. https://doi.org/10.1016/j.neuroimage.2007.04.042

Bell, A. J., & Sejnowski, T. J. (1995). An Information-Maximization Approach to Blind Separation and Blind Deconvolution. *Neural Computation*, *7*(1), 1129–1159.

Belliveau, J. W., Kennedy, D. N., McKinstry, R. C., Buchbinder, B. R., Weisskoff, R. M., Cohen, M. S., Vevea, J. M., Brady, T. J., & Rosen, B. R. (1991). Functional Mapping of the Human Visual Cortex by Magnetic Resonance Imaging. *Science*, *254*(5032), 716–719. https://doi.org/10.1126/science.1948051

Bernal. (2012). fMRI Under Sedation: What Is the Best Choice in Children? *Journal of Clinical Medicine Research*, *4*(6), 363–370. https://doi.org/10.4021/jocmr1047w

Bernstein, M. A., King, K. F., & J, Z. X. (2004). *Handbook of MRI Pulse Sequence*. Elsevier Academic Press.

Birn, R. M., Diamond, J. B., Smith, M. A., & Bandettini, P. A. (2006). Separating respiratory-variation-related fluctuations from neuronal-activity-related fluctuations in fMRI. *NeuroImage*, *31*(4), 1536–1548. https://doi.org/10.1016/j.neuroimage.2006.02.048

Birn, R. M., Saad, Z. S., & Bandettini, P. A. (2001). Spatial heterogeneity of the nonlinear dynamics in the FMRI BOLD response. *NeuroImage*, *14*(4), 817–826. https://doi.org/10.1006/nimg.2001.0873

Birn, R. M., Smith, M. A., Jones, T. B., & Bandettini, P. A. (2008). The respiration response function: The temporal dynamics of fMRI signal fluctuations related to changes in

respiration. *NeuroImage*, *40*(2), 644–654. https://doi.org/10.1016/j.neuroimage.2007.11.059

Bloch, F. (1946). Nuclear induction. *Physical Review*, *70*(7–8), 460–474. https://doi.org/10.1103/PhysRev.70.460

Boegle, R., MacLaren, J., & Zaitsev, M. (2010). Combining prospective motion correction and distortion correction for EPI: Towards a comprehensive correction of motion and susceptibility-induced artifacts. *Magnetic Resonance Materials in Physics, Biology and Medicine*, *23*(4), 263–273. https://doi.org/10.1007/s10334-010-0225-8

Boynton, G. M., Engel, S. A., Glover, G. H., & Heeger, D. J. (1996). Linear systems analysis of functional magnetic resonance imaging in human V1. *Journal of Neuroscience*, *16*(13), 4207–4221. https://doi.org/10.1523/jneurosci.16-13-04207.1996

Buxton, R. B. (2009). *Introduction to Functional Magnetic Resonance Imaging* (2nd ed.). Cambridge Unvesity Press.

Cassidy, P. J., Schneider, J. E., Grieve, S. M., Lygate, C., Neubauer, S., & Clarke, K. (2004). Assessment of Motion Gating Strategies for Mouse Magnetic Resonance at High Magnetic Fields. *Journal of Magnetic Resonance Imaging*, *19*(2), 229–237. https://doi.org/10.1002/jmri.10454

Chen, J. E., & Glover, G. H. (2015). Functional Magnetic Resonance Imaging Methods. *Neuropsychology Review*, *25*(3), 289–313. https://doi.org/10.1007/s11065-015-9294-9

Collins, C. M., & Wang, Z. (2011). Calculation of radiofrequency electromagnetic fields and their effects in MRI of human subjects. *Magnetic Resonance in Medicine*, *65*(5), 1470–1482. https://doi.org/10.1002/mrm.22845

Cox, R. W. (1996). AFNI: Software for analysis and visualization of functional magnetic resonance neuroimages. *Computers and Biomedical Research*, *29*(3), 162–173.

Cox, R. W., & Hyde, J. S. (1997). Software Tools for Analysis and Visualization of FMRI Data NMR in Biomedicine, in press. *NMR Biomed*, *10*(4–5), 171–178.

Dale, A. M., & Buckner, R. L. (1997). Selective averaging of individual trials using fMRI. *NeuroImage*, *5*(4), 329–340.

Davatzikos, C., Ruparel, K., Fan, Y., Shen, D. G., Acharyya, M., Loughead, J. W., Gur, R. C., & Langleben, D. D. (2005). Classifying spatial patterns of brain activity with machine learning methods: Application to lie detection. *NeuroImage*, *28*(3), 663–668. https://doi.org/10.1016/j.neuroimage.2005.08.009

De Bie, H. M. A., Boersma, M., Wattjes, M. P., Adriaanse, S., Vermeulen, R. J., Oostrom, K.

J., Huisman, J., Veltman, D. J., & Delemarre-Van De Waal, H. A. (2010). Preparing children with a mock scanner training protocol results in high quality structural and functional MRI scans. *European Journal of Pediatrics*, *169*(9), 1079–1085. https://doi.org/10.1007/s00431-010-1181-z

Derbyshire, J. A., Wright, G. A., Henkelman, R. M., & Hinks, R. S. (1998). Dynamic scan-plane tracking using MR position monitoring. *Journal of Magnetic Resonance Imaging*, *8*(4), 924–932. https://doi.org/10.1002/jmri.1880080423

Edelstein, W. A., Glover, G. H., Hardy, C. J., & Redington, R. W. (1986). The intrinsic signal-to-noise ratio in NMR imaging. *Magnetic Resonance in Medicine*, *3*(4), 604–618. https://doi.org/10.1002/mrm.1910030413

Ernst, R. R., & Anderson, W. A. (1966). Application of fourier transform spectroscopy to magnetic resonance. *Review of Scientific Instruments*, *37*(1), 93–102. https://doi.org/10.1063/1.1719961

Esses, S. J., Lu, X., Zhao, T., Shanbhogue, K., Dane, B., Bruno, M., & Chandarana, H. (2018). Automated image quality evaluation of T 2 -weighted liver MRI utilizing deep learning architecture. *Journal of Magnetic Resonance Imaging*, *47*(3), 723–728. https://doi.org/10.1002/jmri.25779

Field, A. S., Yen, Y. F., Burdette, J. H., & Elster, A. D. (2000). False cerebral activation on BOLD functional MR images: Study of low-amplitude motion weakly correlated to stimulus. *American Journal of Neuroradiology*, *21*(8), 1388–1396.

Fox, P. T., & Raichle, M. E. (1986). Focal physiological uncoupling of cerebral blood flow and oxidative metabolism during somatosensory stimulation in human subjects. *Proceedings of the National Academy of Sciences of the United States of America*, *83*(4), 1140–1144. https://doi.org/10.1073/pnas.83.4.1140

Friston, K. J., Fletcher, P., Josephs, O., Holmes, A., Rugg, M. D., & Turner, R. (1998). Event-related fMRI: Characterizing differential responses. *NeuroImage*, *7*(1), 30–40. https://doi.org/10.1006/nimg.1997.0306

Friston, Karl J., Ashburner, J., Frith, C. D., Poline, J. -B, Heather, J. D., & Frackowiak, R. S. J. (1995). Spatial registration and normalization of images. *Human Brain Mapping*, *3*(3), 165–189. https://doi.org/10.1002/hbm.460030303

Friston, Karl J., Williams, S., Howard, R., Frackowiak, R. S. J., & Turner, R. (1996). Movement-related effects in fMRI time-series. *Magnetic Resonance in Medicine*, *35*(3), 346–355. https://doi.org/10.1002/mrm.1910350312

Geissler, A., Lanzenberger, R., Barth, M., Tahamtan, A. R., Milakara, D., Gartus, A., & Beisteiner, R. (2005). Influence of fMRI smoothing procedures on replicability of fine scale motor localization. *NeuroImage*, *24*(2), 323–331. https://doi.org/10.1016/j.neuroimage.2004.08.042

Glover, G. H., Li, T. Q., & Ress, D. (2000). Image-based method for retrospective correction of physiological motion effects in fMRI: RETROICOR. *Magnetic Resonance in Medicine*, *44*(1), 162–167. https://doi.org/10.1002/1522-2594(200007)44:1<162::AID-MRM23>3.0.CO;2-E

Goebel, R., Esposito, F., & Formisano, E. (2006). Analysis of Functional Image Analysis Contest (FIAC) data with BrainVoyager QX: From single-subject to cortically aligned group General Linear Model analysis and self-organizing group Independent Component Analysis. *Human Brain Mapping*, *27*(5), 392–401. https://doi.org/10.1002/hbm.20249

Goerke, U., Möller, H. E., Norris, D. G., & Schwarzbauer, C. (2005). A comparison of signal instability in 2D and 3D EPI resting-state fMRI. *NMR in Biomedicine*, *18*(8), 534–542. https://doi.org/10.1002/nbm.987

Gong, T., Tong, Q., Li, Z., He, H., Zhang, H., & Zhong, J. (2021). Deep learning-based method for reducing residual motion effects in diffusion parameter estimation. *Magnetic Resonance in Medicine*, *85*(4), 2278–2293. https://doi.org/10.1002/mrm.28544

Graedel, N. N., McNab, J. A., Chiew, M., & Miller, K. L. (2017). Motion correction for functional MRI with three-dimensional hybrid radial-Cartesian EPI. *Magnetic Resonance in Medicine*, *78*(2), 527–540. https://doi.org/10.1002/mrm.26390

Graedel, N. N., Miller, K. L., & Chiew, M. (2022). Ultrahigh Resolution fMRI at 7T Using Radial-Cartesian TURBINE Sampling. *Magnetic Resonance in Medicine*, *88*(5), 2058–2073. https://doi.org/10.1002/mrm.29359

Griswold, M. A., Jakob, P. M., Heidemann, R. M., Nittka, M., Jellus, V., Wang, J., Kiefer, B., & Haase, A. (2002). Generalized Autocalibrating Partially Parallel Acquisitions (GRAPPA). *Magnetic Resonance in Medicine*, *47*(6), 1202–1210. https://doi.org/10.1002/mrm.10171

Hadj-Bouziane, F., Monfardini, E., Guedj, C., Gardechaux, G., Hynaux, C., Farnè, A., & Meunier, M. (2014). The helmet head restraint system: A viable solution for resting state fMRI in awake monkeys. *NeuroImage*, *86*, 536–543. https://doi.org/10.1016/j.neuroimage.2013.09.068

Hajnal, J. V., Myers, R., Oatridge, A., Schwieso, J. E., Young, I. R., & Bydder, G. M. (1994).

Artifacts due to stimulus correlated motion in functional imaging of the brain. *Magnetic Resonance in Medicine*, *31*(3), 283–291. https://doi.org/10.1002/mrm.1910310307

Hausman, H. K., Hardcastle, C., Kraft, J. N., Evangelista, N. D., Boutzoukas, E. M., O'Shea, A., Albizu, A., Langer, K., Van Etten, E. J., Bharadwaj, P. K., Song, H., Smith, S. G., Porges, E., Hishaw, G. A., Wu, S., DeKosky, S., Alexander, G. E., Marsiske, M., Cohen, R., & Woods, A. J. (2022). The association between head motion during functional magnetic resonance imaging and executive functioning in older adults. *Neuroimage: Reports*, *2*(2), 100085. https://doi.org/10.1016/j.ynirp.2022.100085

Hess, A. T., Dylan Tisdall, M., Andronesi, O. C., Meintjes, E. M., & Van Der Kouwe, A. J. W. (2011). Real-time motion and B0 corrected single voxel spectroscopy using volumetric navigators. *Magnetic Resonance in Medicine*, *66*(2), 314–323. https://doi.org/10.1002/mrm.22805

Hidalgo-Tobon, S. S. (2010). Theory of gradient coil design methods for magnetic resonance imaging. *Concepts in Magnetic Resonance Part A: Bridging Education and Research*, *36*(4), 223–242. https://doi.org/10.1002/cmr.a.20163

Hoinkiss, D. C., Erhard, P., Breutigam, N. J., von Samson-Himmelstjerna, F., Günther, M., & Porter, D. A. (2019). Prospective motion correction in functional MRI using simultaneous multislice imaging and multislice-to-volume image registration. *NeuroImage*, *200*(December 2018), 159–173. https://doi.org/10.1016/j.neuroimage.2019.06.042

Holland, D. J., Liu, C., Song, X., Mazerolle, E. L., Stevens, M. T., Sederman, A. J., Gladden, L. F., D'Arcy, R. C. N., Bowen, C. V., & Beyea, S. D. (2013). Compressed sensing reconstruction improves sensitivity of variable density spiral fMRI. *Magnetic Resonance in Medicine*, *70*(6), 1634–1643. https://doi.org/10.1002/mrm.24621

Hu, X., Le, T. H., Parrish, T., & Erhard, P. (1995). Retrospective estimation and correction of physiological fluctuation in functional MRI. *Magnetic Resonance in Medicine*, *34*(2), 201–212. https://doi.org/10.1002/mrm.1910340211

Hu, Y., & Glover, G. H. (2007). Three-dimensional spiral technique for high-resolution functional MRI. *Magnetic Resonance in Medicine*, *58*(5), 947–951. https://doi.org/10.1002/mrm.21328

Huettel, S. A., & McCarthy, G. (2000). Evidence for a refractory period in the hemodynamic response to visual stimuli as measured by MRI. *NeuroImage*, *11*(5), 547–553. https://doi.org/10.1006/nimg.2000.0553

Huettel, S. A., Obembe, O. O., Song, A. W., & Woldorff, M. G. (2004). The BOLD fMRI

refractory effect is specific to stimulus attributes: Evidence from a visual motion paradigm. *NeuroImage*, *23*(1), 402–408. https://doi.org/10.1016/j.neuroimage.2004.04.031

Huettel, S. A., Song, A. W., & Mccarthy, G. (2014). *Functional Magnetic Resonance Imaging, Third Edition by Scott A. Huettel (2014-08-31): Amazon.com: Books* (3rd ed.). Sinauer Associates Inc. https://www.amazon.com/Functional-Magnetic-Resonance-Imaging-2014-08-31/dp/B01FIXGC3C

Jenkinson, M., Bannister, P., Brady, M., & Smith, S. (2002). Improved Optimization for the Robust and Accurate Linear Registration and Motion Correction of Brain Images. *NeuroImage*, *17*(2), 825–841. https://doi.org/10.1006/nimg.2002.1132

Jenkinson, M., Beckmann, C. F., Behrens, T. E. J., Woolrich, M. W., & Smith, S. M. (2012). FSL. *NeuroImage*, *62*(2), 782–790. https://doi.org/10.1016/j.neuroimage.2011.09.015

Jesmanowicz, A., Bandettini, P. A., & Hyde, J. S. (1998). Single-shot half k-space high-resolution gradient-recalled EPI for fMRI at 3 Tesla. *Magnetic Resonance in Medicine*, *40*(5), 754–762. https://doi.org/10.1002/mrm.1910400517

Jezzard, P. (2012). Correction of geometric distortion in fMRI data. *NeuroImage*, *62*(2), 648–651. https://doi.org/10.1016/j.neuroimage.2011.09.010

Jezzard, P., & Balaban, R. S. (1995). Correction for geometric distortion in echo planar images from B0 field variations. *Magnetic Resonance in Medicine*, *34*(1), 65–73. https://doi.org/10.1002/mrm.1910340111

Jezzard, P., & Clare, S. (1999). Sources of distortion in functional MRI data. *Human Brain Mapping*, *8*(2–3), 80–85. https://doi.org/10.1002/(SICI)1097-0193(1999)8:2/3<80::AID-HBM2>3.0.CO;2-C

Jezzard, P., Metthews, P. M., & Smith, S. M. (Eds.). (2001). *Functional MRI: An Introduction to Methods*. Oxford University Press.

Jones, T. B., Bandettini, P. A., & Birn, R. M. (2008). Integration of motion correction and physiological noise regression in fMRI. *NeuroImage*, *42*(2), 582–590. https://doi.org/10.1016/j.neuroimage.2008.05.019

Kassinopoulos, M., & Mitsis, G. D. (2021). Physiological noise modeling in fMRI based on the pulsatile component of photoplethysmograph. *NeuroImage*, *242*, 1–37. https://doi.org/10.1016/j.neuroimage.2021.118467

Kellman, P., & McVeigh, E. R. (2005). Image reconstruction in SNR units: A general method for SNR measurement. *Magnetic Resonance in Medicine*, *54*(6), 1439–1447.

https://doi.org/10.1002/mrm.20713

Kinchesh, P., Gilchrist, S., Beech, J. S., Gomes, A. L., Kersemans, V., Newman, R. G., Vojnovic, B., Allen, P. D., Brady, M., Muschel, R. J., & Smart, S. C. (2018). Prospective gating control for highly efficient cardio-respiratory synchronised short and constant TR MRI in the mouse. *Magnetic Resonance Imaging*, *53*(May), 20–27. https://doi.org/10.1016/j.mri.2018.06.017

Korin, H. W., Felmlee, J. P., Riederer, S. J., & Ehman, R. L. (1995). Spatial-Frequency-Tuned Markers and Adaptive Correction for Rotational Motion. *Magnetic Resonance in Medicine*, *33*(5), 663–669. https://doi.org/10.1002/mrm.1910330511

Krämer, M., Jochimsen, T. H., & Reichenbach, J. R. (2012). Functional magnetic resonance imaging using PROPELLER-EPI. *Magnetic Resonance in Medicine*, *68*(1), 140–151. https://doi.org/10.1002/mrm.23220

Krüger, G., & Glover, G. H. (2001). Physiological noise in oxygenation-sensitive magnetic resonance imaging. *Magnetic Resonance in Medicine*, *46*(4), 631–637. https://doi.org/10.1002/mrm.1240

Krüger, G., Kastrup, A., & Glover, G. H. (2001). Neuroimaging at 1.5 T and 3.0 T: Comparison of oxygenation-sensitive magnetic resonance imaging. *Magnetic Resonance in Medicine*, *45*(4), 595–604. https://doi.org/10.1002/mrm.1081

Küstner, T., Liebgott, A., Mauch, L., Martirosian, P., Bamberg, F., Nikolaou, K., Yang, B., Schick, F., & Gatidis, S. (2018). Automated reference-free detection of motion artifacts in magnetic resonance images. *Magnetic Resonance Materials in Physics, Biology and Medicine*, *31*(2), 243–256. https://doi.org/10.1007/s10334-017-0650-z

Lauterbur, P. C. (1973). Image Formation by Induced Local Interactions: Examples Employing Nuclear Magnetic Resonance. *Nature*, *242*, 190–191.

Le Ster, C., Moreno, A., Mauconduit, F., Gras, V., Stirnberg, R., Poser, B. A., Vignaud, A., Eger, E., Dehaene, S., Meyniel, F., & Boulant, N. (2019). Comparison of SMS-EPI and 3D-EPI at 7T in an fMRI localizer study with matched spatiotemporal resolution and homogenized excitation profiles. *PLoS ONE*, *14*(11), 1–17. https://doi.org/10.1371/journal.pone.0225286

Liu, T. T. (2016). Noise contributions to the fMRI signal: An overview. *NeuroImage*, *143*, 141–151. https://doi.org/10.1016/j.neuroimage.2016.09.008

Liu, T. T. (2017). Reprint of 'Noise contributions to the fMRI signal: An Overview.' *NeuroImage*, *154*, 4–14. https://doi.org/10.1016/j.neuroimage.2017.05.031

Maclaren, J., Herbst, M., Speck, O., & Zaitsev, M. (2013). Prospective motion correction in brain imaging: A review. *Magnetic Resonance in Medicine*, *69*(3), 621–636. https://doi.org/10.1002/mrm.24314

MacLaren, J., Lee, K. J., Luengviriya, C., Speck, O., & Zaitsev, M. (2011). Combined prospective and retrospective motion correction to relax navigator requirements. *Magnetic Resonance in Medicine*, *65*(6), 1724–1732. https://doi.org/10.1002/mrm.22754

Mahmoudi, A., Takerkart, S., Regragui, F., Boussaoud, D., & Brovelli, A. (2012). Multivoxel Pattern Analysis for fMRI Data : A Review. *Comput Math Methods Med.*, *2012*. https://doi.org/10.1155/2012/961257

Mayer, A. R., Franco, A. R., Ling, J., & Cañive, J. M. (2007). Assessment and quantification of head motion in neuropsychiatric functional imaging research as applied to schizophrenia. *Journal of the International Neuropsychological Society*, *13*(5), 839–845. https://doi.org/10.1017/S1355617707071081

McKeown, M. J., Hansen, L. K., & Sejnowsk, T. J. (2003). Independent component analysis of functional MRI: What is signal and what is noise? *Current Opinion in Neurobiology*, *13*(5), 620–629. https://doi.org/10.1016/j.conb.2003.09.012

Mckeown, M. J., Makeig, S., Brown, G. G., Jung, T., Kindermann, S. S., Bell, A. J., & Sejnowski, T. J. (1998). Analysis of fMRI data by blind separation into independent spatial components. *Human Brain Mapping*, *6*(3), 160–188. https://doi.org/10.1002/(sici)1097-0193(1998)6:3<160::aid-hbm5>3.3.co;2-r

Menon, V., Lim, K. O., Anderson, J. H., Johnson, J., & Pfefferbaum, A. (1997). Design and efficacy of a head-coil bite bar for reducing movement-related artifacts during functional MRI scanning. *Behavior Research Methods, Instruments, and Computers*, *29*(4), 589–594. https://doi.org/10.3758/BF03210613

Mikl, M., Mareček, R., Hluštík, P., Pavlicová, M., Drastich, A., Chlebus, P., Brázdil, M., & Krupa, P. (2008). Effects of spatial smoothing on fMRI group inferences. *Magnetic Resonance Imaging*, *26*(4), 490–503. https://doi.org/10.1016/j.mri.2007.08.006

Mintun, M. A., Lundstrom, B. N., Snyder, A. Z., Vlassenko, A. G., Shulman, G. L., & Raichle, M. E. (2001). Blood flow and oxygen delivery to human brain during functional activity: Theoretical modeling and experimental data. *Proceedings of the National Academy of Sciences of the United States of America*, *98*(12), 6859–6864. https://doi.org/10.1073/pnas.111164398

Mitchell, H. H., Hamilton, T. S., Steggerda, F. R., & Bean, H. W. (1945). The chemical

composition of the adult human body and its bearing on the biochemistry of growth. *Journal of Biological Chemistry*, *158*(3), 625–637. https://doi.org/10.1016/S0021-9258(19)51339-4

Moeller, S., Yacoub, E., Olman, C. A., Auerbach, E., Strupp, J., Harel, N., & Uğurbil, K. (2010). Multiband multislice GE-EPI at 7 tesla, with 16-fold acceleration using partial parallel imaging with application to high spatial and temporal whole-brain FMRI. *Magnetic Resonance in Medicine*, *63*(5), 1144–1153. https://doi.org/10.1002/mrm.22361

Monti, M. M. (2011). Statistical analysis of fMRI time-series: A critical review of the GLM approach. *Frontiers in Human Neuroscience*, *5*(MARCH), 1–13. https://doi.org/10.3389/fnhum.2011.00028

Muresan, L., Renken, R., Roerdink, J. B. T. M., & Duifhuis, H. (2005). Automated correction of spin-history related motion artefacts in fMRI: Simulated and phantom data. *IEEE Transactions on Biomedical Engineering*, *52*(8), 1450–1460. https://doi.org/10.1109/TBME.2005.851484

Neggers, S. F. W., Hermans, E. J., & Ramsey, N. F. (2008). Enhanced sensitivity with fast three-dimensional blood-oxygen-level-dependent functional MRI: Comparison of SENSE-PRESTO and 2D-EPI at 3T. *NMR in Biomedicine*, *21*(7), 663–676. https://doi.org/10.1002/nbm.1235

Norris, D. G. (2006). Principles of magnetic resonance assessment of brain function. *Journal of Magnetic Resonance Imaging*, *23*(6), 794–807. https://doi.org/10.1002/jmri.20587

Oakes, T. R., Johnstone, T., Ores Walsh, K. S., Greischar, L. L., Alexander, A. L., Fox, A. S., & Davidson, R. J. (2005). Comparison of fMRI motion correction software tools. *NeuroImage*, *28*(3), 529–543. https://doi.org/10.1016/j.neuroimage.2005.05.058

Ogawa, S., Lee, T. M., Kay, A. R., & Tank, D. W. (1990). Brain magnetic resonance imaging with contrast dependent on blood oxygenation. *Pro. Natl. Acad. Sci. USA*, *87*, 9868–9872.

Ogawa, S., Menon, R. S., Tank, D. W., Kim, S. G., Merkle, H., Ellermann, J. M., & Ugurbil, K. (1993). Functional brain mapping by blood oxygenation level-dependent contrast magnetic resonance imaging. A comparison of signal characteristics with a biophysical model. *Biophysical Journal*, *64*(3), 803–812. https://doi.org/10.1016/S0006-3495(93)81441-3

Ogawa, S., Tank, D. W., Menon, R., Ellermann, J. M., Kim, S. G., Merkle, H., & Ugurbil, K. (1992). Intrinsic signal changes accompanying sensory stimulation: Functional brain mapping with magnetic resonance imaging. *Proceedings of the National Academy of*

Sciences of the United States of America, *89*(13), 5951–5955. https://doi.org/10.1073/pnas.89.13.5951

Ooi, M. B., Krueger, S., Thomas, W. J., Swaminathan, S. V., & Brown, T. R. (2009). Prospective real-time correction for arbitrary head motion using active markers. *Magnetic Resonance in Medicine*, *62*(4), 943–954. https://doi.org/10.1002/mrm.22082

Ooi, M. B., Muraskin, J., Zou, X., Thomas, W. J., Krueger, S., Aksoy, M., Bammer, R., & Brown, T. R. (2013). Combined prospective and retrospective correction to reduce motion-induced image misalignment and geometric distortions in EPI. *Magnetic Resonance in Medicine*, *69*(3), 803–811. https://doi.org/10.1002/mrm.24285

Paige, C. C., & Saunders, M. A. (1982). LSQR: An Algorithm for Sparse Linear Equations and Sparse Least Squares. *ACM Transactions on Mathematical Software*, *8*(1), 43–71. https://doi.org/10.1145/355984.355989

Paschal, C. B., & Morris, H. D. (2004). K-Space in the Clinic. *Journal of Magnetic Resonance Imaging*, *19*(2), 145–159. https://doi.org/10.1002/jmri.10451

Pauling, L., & Coryell, C. D. (1936). The Magnetic Properties and Structure of Hemoglobin, Oxyhemoglobin and Carbonmonoxyhemoglobin. *Proceedings of the National Academy of Sciences*, *22*(4), 210–216. https://doi.org/10.1073/pnas.22.4.210

Pipe, J. G. (1999). Motion correction with PROPELLER MRI: Application to head motion and free-breathing cardiac imaging. *Magnetic Resonance in Medicine*, *42*(5), 963–969. https://doi.org/10.1002/(SICI)1522-2594(199911)42:5<963::AID-MRM17>3.0.CO;2-L

Poldrack, R. A., Paré-Blagoev, E. J., & Grant, P. E. (2002). Pediatric functional magnetic resonance imaging: Progress and challenges. *Topics in Magnetic Resonance Imaging*, *13*(1), 61–70. https://doi.org/10.1097/00002142-200202000-00005

Poser, B. A., Koopmans, P. J., Witzel, T., Wald, L. L., & Barth, M. (2010). Three dimensional echo-planar imaging at 7 Tesla. *NeuroImage*, *51*(1), 261–266. https://doi.org/10.1016/j.neuroimage.2010.01.108

Power, J. D., Barnes, K. A., Snyder, A. Z., Schlaggar, B. L., & Petersen, S. E. (2012). Spurious but systematic correlations in functional connectivity MRI networks arise from subject motion. *NeuroImage*, *59*(3), 2142–2154. https://doi.org/10.1016/j.neuroimage.2011.10.018

Pruessmann, K. P., Weiger, M., Scheidegger, M. B., & Boesiger, P. (1999). SENSE: Sensitivity encoding for fast MRI. *Magnetic Resonance in Medicine*, *42*(5), 952–962. https://doi.org/10.1002/(SICI)1522-2594(199911)42:5<952::AID-MRM16>3.0.CO;2-S

Raj, D., Anderson, A. W., & Gore, J. C. (2001). Respiratory effects in human functional magnetic resonance imaging due to bulk susceptibility changes. *Physics in Medicine and Biology*, *46*(12), 3331–3340. https://doi.org/10.1088/0031-9155/46/12/318

Rasmus M. Birn, J. Bodurka, P. A. B. (2001). The efficacy of cardiac gating with variable TR correction in fMRI. *Proc.Intl. Soc. Mag. Reson*, *9*, 1.

Satterthwaite, T. D., Wolf, D. H., Loughead, J., Ruparel, K., Elliott, M. A., Hakonarson, H., Gur, R. C., & Gur, R. E. (2012). Impact of in-scanner head motion on multiple measures of functional connectivity: Relevance for studies of neurodevelopment in youth. *NeuroImage*, *60*(1), 623–632. https://doi.org/10.1016/j.neuroimage.2011.12.063

Scouten, A., Papademetris, X., & Constable, R. T. (2006). Spatial resolution, signal-to-noise ratio, and smoothing in multi-subject functional MRI studies. *NeuroImage*, *30*(3), 787–793. https://doi.org/10.1016/j.neuroimage.2005.10.022

Seto, E., Sela, G., McIlroy, W. E., Black, S. E., Staines, W. R., Bronskill, M. J., McIntosh, A. R., & Graham, S. J. (2001). Quantifying head motion associated with motor tasks used in fMRI. *NeuroImage*, *14*(2), 284–297. https://doi.org/10.1006/nimg.2001.0829

Shmueli, K., van Gelderen, P., de Zwart, J. A., Horovitz, S. G., Fukunaga, M., Jansma, J. M., & Duyn, J. H. (2007). Low-frequency fluctuations in the cardiac rate as a source of variance in the resting-state fMRI BOLD signal. *NeuroImage*, *38*(2), 306–320. https://doi.org/10.1016/j.neuroimage.2007.07.037

Silva, A. C., & Merkle, H. (2003). Hardware considerations for functional magnetic resonance imaging. *Concepts in Magnetic Resonance Part A: Bridging Education and Research*, *16*(1), 35–49. https://doi.org/10.1002/cmr.a.10052

Smith, S. M., Jenkinson, M., Woolrich, M. W., Beckmann, C. F., Behrens, T. E. J., Johansen-Berg, H., Bannister, P. R., De Luca, M., Drobnjak, I., Flitney, D. E., Niazy, R. K., Saunders, J., Vickers, J., Zhang, Y., De Stefano, N., Brady, J. M., & Matthews, P. M. (2004). Advances in functional and structural MR image analysis and implementation as FSL. *NeuroImage*, *23*(SUPPL. 1), 208–219. https://doi.org/10.1016/j.neuroimage.2004.07.051

Speck, O., Hennig, J., & Zaitsev, M. (2006). Prospective real-time slice-by-slice motion correction for fMRI in freely moving subjects. *Magnetic Resonance Materials in Physics, Biology and Medicine*, *19*(2), 55–61. https://doi.org/10.1007/s10334-006-0027-1

Stehling, M. K., Turner, R., & Mansfield, P. (1991). Echo-planar imaging: Magnetic resonance imaging in a fraction of a second. In *Science* (Vol. 254, pp. 43–50).

https://doi.org/10.1126/science.1925560

Stirnberg, R., Huijbers, W., Brenner, D., Poser, B. A., Breteler, M., & Stöcker, T. (2017). Rapid whole-brain resting-state fMRI at 3 T: Efficiency-optimized three-dimensional EPI versus repetition time-matched simultaneous-multi-slice EPI. *NeuroImage*, *163*(August), 81–92. https://doi.org/10.1016/j.neuroimage.2017.08.031

Sujit, S. J., Coronado, I., Kamali, A., Narayana, P. A., & Gabr, R. E. (2019). Automated image quality evaluation of structural brain MRI using an ensemble of deep learning networks. *Journal of Magnetic Resonance Imaging*, *50*(4), 1260–1267. https://doi.org/10.1002/jmri.26693

Tamada, D., Kromrey, M.-L., Ichikawa, S., Onishi, H., & Motosugi, U. (2020). Motion Artifact Reduction Using a Convolutional Neural Network for Dynamic Contrast Enhanced MR Imaging of the Liver. *Magnetic Resonance in Medical Sciences*, *19*(1), 64–76. https://doi.org/10.2463/mrms.mp.2018-0156

Tanabe, J., Miller, D., Tregellas, J., Freedman, R., & Meyer, F. G. (2002). Comparison of detrending methods for optimal fMRI preprocessing. *NeuroImage*, *15*(4), 902–907. https://doi.org/10.1006/nimg.2002.1053

Thesen, S., Heid, O., Mueller, E., & Schad, L. R. (2000). Prospective Acquisition Correction for head motion with image-based tracking for real-time fMRI. *Magnetic Resonance in Medicine*, *44*(3), 457–465. https://doi.org/10.1002/1522-2594(200009)44:3<457::AID-MRM17>3.0.CO;2-R

Thomason, M. E., Foland, L. C., & Glover, G. H. (2007). Calibration of BOLD fMRI using breath holding reduces group variance during a cognitive task. *Human Brain Mapping*, *28*(1), 59–68. https://doi.org/10.1002/hbm.20241

Tisdall, M. D., Hess, A. T., Reuter, M., Meintjes, E. M., Fischl, B., & Van Der Kouwe, A. J. W. (2012). Volumetric navigators for prospective motion correction and selective reacquisition in neuroanatomical MRI. *Magnetic Resonance in Medicine*, *68*(2), 389–399. https://doi.org/10.1002/mrm.23228

Todd, N., Josephs, O., Callaghan, M. F., Lutti, A., & Weiskopf, N. (2015). Prospective motion correction of 3D echo-planar imaging data for functional MRI using optical tracking. *NeuroImage*, *113*, 1–12. https://doi.org/10.1016/j.neuroimage.2015.03.013

Triantafyllou, C., Hoge, R. D., Krueger, G., Wiggins, C. J., Potthast, A., Wiggins, G. C., & Wald, L. L. (2005). Comparison of physiological noise at 1.5 T, 3 T and 7 T and optimization of fMRI acquisition parameters. *NeuroImage*, *26*(1), 243–250.

https://doi.org/10.1016/j.neuroimage.2005.01.007

Tsai, C. M., & Nishimura, D. G. (2000). Reduced aliasing artifacts using variable-density k-space sampling trajectories. *Magnetic Resonance in Medicine*, *43*(3), 452–458. https://doi.org/10.1002/(SICI)1522-2594(200003)43:3<452::AID-MRM18>3.0.CO;2-B

Turner, R., Bihan, D. Le, Moonen, C. T. W., Despres, D., & Frank, J. (1991). Echo-planar time course MRI of cat brain oxygenation changes. *Magnetic Resonance in Medicine*, *22*(1), 159–166. https://doi.org/10.1002/mrm.1910220117

Van Der Kouwe, A. J. W., Benner, T., & Dale, A. M. (2006). Real-time rigid body motion correction and shimming using cloverleaf navigators. *Magnetic Resonance in Medicine*, *56*(5), 1019–1032. https://doi.org/10.1002/mrm.21038

van der Zwaag, W., Francis, S., Head, K., Peters, A., Gowland, P., Morris, P., & Bowtell, R. (2009). fMRI at 1.5, 3 and 7 T: Characterising BOLD signal changes. *NeuroImage*, *47*(4), 1425–1434. https://doi.org/10.1016/j.neuroimage.2009.05.015

van Dijk, K. R. A., Sabuncu, M. R., & Buckner, R. L. (2012). The influence of head motion on intrinsic functional connectivity MRI. *NeuroImage*, *59*(1), 431–438. https://doi.org/10.1016/j.neuroimage.2011.07.044

Wald, L. L., & Polimeni, J. R. (2017). Impacting the effect of fMRI noise through hardware and acquisition choices – Implications for controlling false positive rates. *NeuroImage*, *154*(December 2016), 15–22. https://doi.org/10.1016/j.neuroimage.2016.12.057

Wang, C., Liang, Y., Wu, Y., Zhao, S., & Du, Y. P. (2020). Correction of out-of-FOV motion artifacts using convolutional neural network. *Magnetic Resonance Imaging*, *71*(May), 93–102. https://doi.org/10.1016/j.mri.2020.05.004

White, N., Roddey, C., Shankaranarayanan, A., Han, E., Rettmann, D., Santos, J., Kuperman, J., & Dale, A. (2010). PROMO: Real-time prospective motion correction in MRI using image-based tracking. *Magnetic Resonance in Medicine*, *63*(1), 91–105. https://doi.org/10.1002/mrm.22176

Winkler, M. L., Ortendahl, D. A., Mills, T. C., Crooks, L. E., Sheldon, P. E., Kaufman, L., & Kramer, D. M. (1988). Characteristics of partial flip angle and gradient reversal MR imaging. *Radiology*, *166*(1 I), 17–26. https://doi.org/10.1148/radiology.166.1.3275967

Woolrich, M. W., Behrens, T. E. J., & Smith, S. M. (2004). Constrained linear basis sets for HRF modelling using Variational Bayes. *NeuroImage*, *21*(4), 1748–1761. https://doi.org/10.1016/j.neuroimage.2003.12.024

Woolrich, M. W., Jbabdi, S., Patenaude, B., Chappell, M., Makni, S., Behrens, T., Beckmann,

C., Jenkinson, M., & Smith, S. M. (2009). Bayesian analysis of neuroimaging data in FSL. *NeuroImage*, *45*(1 Suppl), S173–S186. https://doi.org/10.1016/j.neuroimage.2008.10.055

Woolrich, M. W., Ripley, B. D., Brady, M., & Smith, S. M. (2001). Temporal autocorrelation in univariate linear modeling of FMRI data. *NeuroImage*, *14*(6), 1370–1386. https://doi.org/10.1006/nimg.2001.0931

Worsley, K. J., & Friston, K. J. (1995). Analysis of fMRI Time-Series Revisited—Again. *NeuroImage*, *2*(3), 173–181. https://doi.org/10.1006/nimg.1995.1023

Yan, C. G., Cheung, B., Kelly, C., Colcombe, S., Craddock, R. C., Di Martino, A., Li, Q., Zuo, X. N., Castellanos, F. X., & Milham, M. P. (2013). A comprehensive assessment of regional variation in the impact of head micromovements on functional connectomics. *NeuroImage*, *76*, 183–201. https://doi.org/10.1016/j.neuroimage.2013.03.004

Yancey, S. E., Rotenberg, D. J., Tam, F., Chiew, M., Ranieri, S., Biswas, L., Anderson, K. J. T., Nicole Baker, S., Wright, G. A., & Graham, S. J. (2011). Spin-history artifact during functional MRI: Potential for adaptive correction. *Medical Physics*, *38*(8), 4634–4646. https://doi.org/10.1118/1.3583814

Yuan, W., Altaye, M., Ret, J., Schmithorst, V., Byars, A. W., Plante, E., & Holland, S. K. (2009). Quantification of head motion in children during various fMRI language tasks. *Human Brain Mapping*, *30*(5), 1481–1489. https://doi.org/10.1002/hbm.20616

Zaitsev, M., Akin, B., LeVan, P., & Knowles, B. R. (2017). Prospective motion correction in functional MRI. *NeuroImage*, *154*(November 2016), 33–42. https://doi.org/10.1016/j.neuroimage.2016.11.014

Zaitsev, M., Dold, C., Sakas, G., Hennig, J., & Speck, O. (2006). Magnetic resonance imaging of freely moving objects: prospective real-time motion correction using an external optical motion tracking system. *NeuroImage*, *31*(3), 1038–1050. https://doi.org/10.1016/j.neuroimage.2006.01.039

Zaitsev, M., Maclaren, J., & Herbst, M. (2015). Motion artifacts in MRI: A complex problem with many partial solutions. *Journal of Magnetic Resonance Imaging*, *42*(4), 887–901. https://doi.org/10.1002/jmri.24850

Zhuo Wu Fu, Wang, Y., Grimm, R. C., Rossman, P. J., Felmlee, J. P., Riederer, S. J., & Ehman, R. L. (1995). Orbital navigator echoes for motion measurements in magnetic resonance imaging. *Magnetic Resonance in Medicine*, *34*(5), 746–753. https://doi.org/10.1002/mrm.1910340514